Supercritical Water Gasification of Model Alcohols

Brian R. Pinkard

A dissertation submitted in partial fulfillment of
the requirements for the degree of

Doctor of Philosophy

University of Washington

2020

Reading Committee:

Igor V. Novosselov, Chair

John Kramlich

Per Reinhall

Program Authorized to Offer Degree:

Mechanical Engineering

University of Washington

Abstract

Supercritical Water Gasification of Model Alcohols

Brian R. Pinkard

Chair of the Supervisory Committee

Igor V. Novosselov

Department of Mechanical Engineering

Supercritical water is a unique reaction medium with emerging applications in waste destruction, fuel generation, and material synthesis. The high temperatures and pressures necessary to bring water to the supercritical state create a kinetically and thermodynamically advantageous environment for redox reactions to occur, with minimized mass transfer limitations. Supercritical water acts both as reactant and reaction medium, facilitating the rapid decomposition of many organic molecules into hydrogen-rich gas. As a waste-to-energy technology, supercritical water gasification shows promise for converting organic waste, especially wet waste, into green hydrogen. Despite decades of interest in supercritical water gasification and oxidation, fundamental knowledge of reaction chemistry in supercritical water remains limited. It is relevant to study the chemistry of simple model compounds in supercritical water as a means of elucidating reaction phenomena occurring with common compound classes or functional groups.

A continuous, tubular supercritical water reactor facilitates novel studies of reaction kinetics in supercritical water. *In situ* Raman spectroscopy allows for real-time monitoring of reaction products, short experimentation times, and rapid identification and quantification of reaction products. Through multiple studies investigating reaction kinetics of model compounds in the gasification environment, chemical reaction routes and mechanisms of several model compounds are determined under varied conditions.

As a proof-of-concept study to demonstrate the validity of using Raman spectroscopy for determining product yields, the reaction kinetics of formic acid (HCOOH) in 25 MPa water are quantified for subcritical and supercritical temperatures between 300 and 430 °C. *In situ* Raman spectroscopy facilitates precise, time-resolved data collection.

First-order reaction behavior is not observed during gasification of methanol, ethanol, or isopropyl alcohol in supercritical water between 500 and 560 °C. Chain-branching free radical reaction mechanisms are inferred to drive the decomposition of alcohols in supercritical water, and the heterogeneous catalyst of the reactor wall surface is significant for initiating radical reactions. Global reaction pathways are proposed, and mechanisms for free radical initiation, propagation, and termination are discussed. Ethanol is also studied under partially oxidative conditions at 500 to 530 °C, where intermediate reaction products counterintuitively polymerize to form char. A deeper understanding of reaction mechanisms in supercritical water is gained, lending insight towards the conditions necessary to maximize gaseous yields and minimize char buildup.

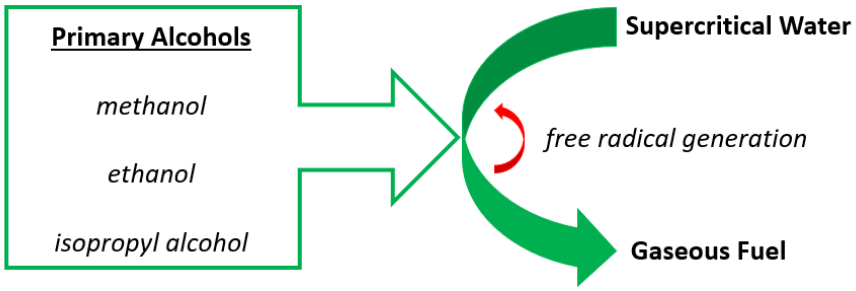

Table of Contents

List of Figures

List of Tables

List of Abbreviations

BPR - back pressure regulator

CE - carbon conversion efficiency

CFD - computational fluid dynamic

DI - deionized

DRE - destruction and removal efficiency

DTRA - Defense Threat Reduction Agency

FTIR - Fourier transform infrared

GC - gas chromatography

GE - gasification efficiency

HACA - H-abstraction, C_2H_2-addition

HE - hydrogen efficiency

HPLC - high-pressure liquid chromatography

HTD - deteriorated heat transfer

HTE - enhanced heat transfer

HTHP - high-temperature, high-pressure

ID - inner diameter

IHM - indirect hard modeling

NMR - nuclear magnetic resonance

OFR - oxidant-to-fuel stoichiometric equivalence ratio

PAH - polycyclic aromatic hydrocarbon

PFR - plug flow reactor

S/V - surface-to-volume ratio

SCW - supercritical water

SCWG - supercritical water gasification

SCWO - supercritical water oxidation

SCWR - supercritical water gasification

SFR - Sandia Supercritical Fluid Reactor

SWPO - supercritical water partial oxidation

TOC - total organic carbon

WGS - water-gas shift

Acknowledgements

My deepest gratitude to my advisor, Prof. Igor Novosselov, for providing me with excellent guidance throughout my entire time at the University of Washington. Igor has continually allowed me the flexibility and independence that I needed to be successful at UW and I would not be finishing this degree without his continued support and encouragement.

Thanks to Dr. John Kramlich and Dr. Per Reinhall for their continued guidance of the supercritical water reactor team. Their expertise and insights repeatedly proved valuable both with tackling practical engineering challenges and with interpreting experimental results.

My appreciation to all the other students who have been a part of the supercritical water research team. David Gorman did an excellent job designing and fabricating the majority of our supercritical water gasification reactor. Kartik Tiwari's expertise with computational fluid dynamics allowed us to design an effective mixing section for accurate chemical kinetics studies. Thanks to Vedant Maheshwari, Stuart Moore, and Anmol Purohit, for continued assistance running the reactor and collecting data.

Thanks to the administrative staff in the Mechanical Engineering department for support, assistance with purchasing research materials, and for keeping the department running efficiently.

Funding for this work and for my time at the UW came both through the Defense Threat Reduction Agency (DTRA) grant number HDTRA1-17-1-0001, and from multiple UW fellowships. I am extremely grateful to have had the financial support necessary to perform this research – it is a gift to not worry about funding as a graduate student.

Finally, and most importantly, thanks to family and friends for supporting me through this process. I would not have finished without the love, patience, support, and understanding of my wife, Christina Elderkin, my parents Jack and Gayle, and my brother Michael.

1. Introduction

Supercritical water (SCW) continues to gain importance as a green reaction medium to facilitate gasification and/or oxidation of organic compounds. At supercritical conditions, water exhibits unique thermophysical properties beneficial for waste treatment, organic compound gasification, and material synthesis. As water is heated and pressurized past its critical point (374°C, 22.1 MPa), the H-bond network begins to dissipate and the dielectric constant drops, vastly increasing the solubility of simple and complex organic molecules [1]. At conditions near the critical point, the physical properties of water, such as density and viscosity can be varied continuously from liquid-like to gas-like without a true phase change. Lowered density and viscosity allow reactions to occur in a single fluid phase with minimal mass transfer limitations. These and other unique thermophysical characteristics have led to the exploration of SCW as a means to produce gaseous fuel from biomass or sewage [2-7], to mineralize complex waste streams [8], and to synthesize metal oxide nanoparticles [9, 10], among other applications.

Reactions of organic compounds in supercritical water can broadly be lumped into three categories, depending on the oxidant-to-fuel stoichiometric equivalence ratio (OFR), which indicates the amount of oxygen added to the reaction environment. These are: (i) supercritical water gasification (SCWG), (OFR = 0), (ii) supercritical water partial oxidation (SWPO), ($0 < OFR < 1$), and (iii) supercritical water oxidation (SCWO), ($OFR \geq 1$). Laboratory-scale supercritical water reactors (SCWRs) have primarily been used to study SCWO and SCWG of model compounds, biomass feedstocks, and chemical warfare agent surrogates, and have led to the development of several pilot and industrial scale reactors [2]. SCWRs have also been constructed for hydrothermal synthesis of metal oxides and metal-organic frameworks, although such particle formation is undesirable in SCWO and SCWG reactors [9, 10].

1.1. Supercritical Water Gasification

SCWG is a thermochemical process for generating H_2-rich syngas from organic feedstocks. Gasification in SCW was first explored in the 1970s for hydrothermal refining of glucose to gaseous products [11] and has since been investigated for a variety of model organic compounds [12] and complex organic feedstocks [2, 6, 7]. The unique thermophysical properties of SCW are exploited to produce a gaseous product rich in H_2 from organic feedstocks, which can be processed without the energetically costly drying step necessary for conventional gasification [3]. Copious wet organic wastes exist as potential gasification feedstocks, including food industry waste, paper mill waste, and sewage sludge; feedstocks with water contents as high as 80% are energetically and economically viable [3, 13].

In a SCWG regime, decomposition reactions take place in the absence of an external oxidant. Gasification reactions are reductive and endothermic, as fuel value in the feedstock is conserved into the final gaseous mixture. Active reactions which occur during SCWG include hydrolysis, dehydration, decarboxylation, dehydrogenation, pyrolysis, water-gas shift (WGS), and methanation, among others. Broadly, heterogeneous feedstocks in the SCWG environment react along two general and competing reaction pathways. The desired pathway leads to yields of hydrogen (H_2), carbon monoxide (CO), carbon dioxide (CO_2), and methane (CH_4). The undesired pathway leads to refractory products, such as char [14]. Much SCWG research is focused on improving capabilities for processing biomass [2, 6, 7], sewage sludge [3-5], or other organic wastes into gaseous products while minimizing char formation. Several general strategies have been explored to accomplish this, including optimizing reaction parameters (e.g. temperature, residence time), designing clever strategies for reagent introduction and solid collection, and/or

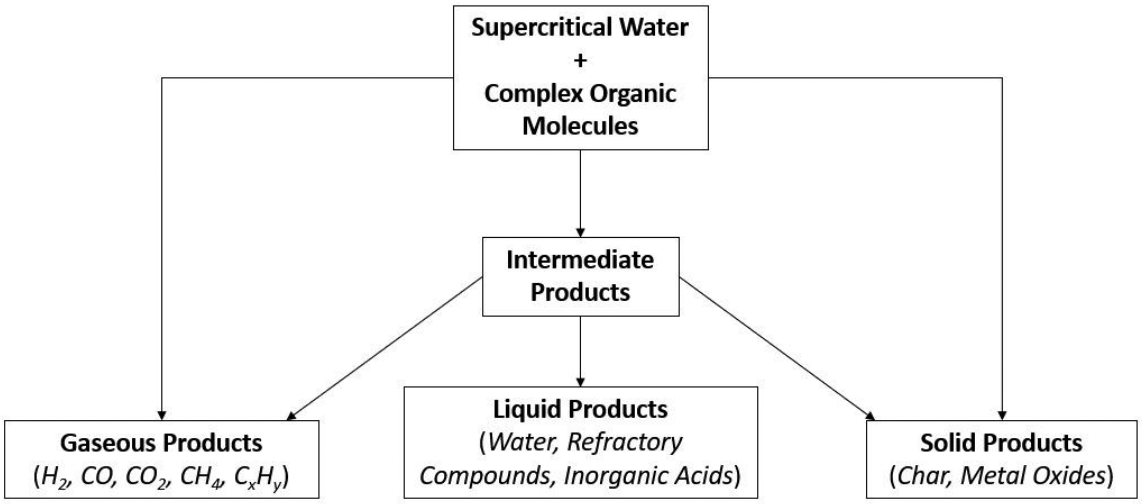

Figure 1: Generalized reaction network for supercritical water gasification of complex organic molecules. Desirable reaction pathways lead to high yields of gaseous products, while undesirable reactions lead to the formation of char. Heteroatoms or metals present in the feedstock can form metal oxides or inorganic acids, causing significant issues with reactor clogging and corrosion.

introducing a catalyst. For a practical benchmark, an effectively designed SCWG reactor may be able to produce hydrogen and methane from waste biomass with >20% solid content at an economically competitive cost if the issues of char suppression, energetic efficiency, and reagent introduction are solved [3].

1.2. Supercritical Water Partial Oxidation

SCWG typically requires external heat input to maintain reaction temperatures due to systemic heat loss and endothermic reactions. Heat recovery via heat integration is one opportunity to improve SCWG efficiency as the technology advances beyond the lab-scale. In a SWPO regime, a fraction of the feedstock fuel value is consumed in exothermic oxidation reactions providing the heat required for decomposition of parent compounds. By introducing sub-stoichiometric oxygen into the reactor, heating efficiency is improved, and a syngas is still produced. SWPO has the potential to reduce char formation, a hallmark limitation to SCWG at high feedstock

concentrations. Practical implementation of syngas production using SCW processes will likely involve partial oxidation, although fundamental research on kinetic rates and competing reaction pathways at varied oxidant concentrations is lacking.

1.3. Supercritical Water Oxidation

In a SCWO regime, all fuel value of the feedstock is sacrificed in favor of destruction of the parent compound; for this reason, SCWO is primarily used for mineralizing toxic feedstocks. Under supercritical conditions, organic compounds and oxygen become fully miscible in water, allowing oxidation to occur in a single fluid phase with excellent transport properties. Many organic compounds are completely oxidized in under one minute with optimized temperatures and oxygen concentrations. SCWO has been successfully commercialized for neutralizing chemical and biological wastes, while SCWG has not to-date been successfully commercialized due to numerous technical and economic barriers [15].

Despite similarities between SCWO and SCWG, the design challenges of respective reactors are substantially different. The SCWO environment is oxidative, while the SCWG environment is reductive, thus the corrosion behavior of many materials differs between SCWO and SCWG [13, 16]. Additionally, thermal management strategies are different, as SCWG reactors require heat input, while SCWO reactors require heat removal, especially when reactors are used for kinetic studies. Some reactors have been designed to operate with or without an oxidant, such as the Sandia Supercritical Fluids Reactor (SFR) [17], but most are tailored towards a single processing regime. In general, a reactor optimized for SCWO may not function effectively for SCWG, and vice versa.

1.4. Reactions of Model Compounds in Supercritical Water

Basic knowledge of reaction rates, pathways, and mechanisms for key model compounds is required to advance SCWG towards large-scale applications. Maximizing H_2 production is a common goal for biomass gasification; insight into reaction pathways and rates allows for the optimization of reaction temperatures, residence times, and selected catalyst [12, 15, 18, 19].

Only a limited number of studies of fundamental SCWG reaction kinetics have been performed in continuous, tubular reactors, which simulates the catalytic wall behavior in industrial-scale systems. To advance basic understanding of chemical reactions in SCW, the reaction kinetics of model alcohols in SCW are studied in detail. The reaction kinetics of methanol, ethanol, and isopropyl alcohol in SCW have been poorly characterized in the literature, and the reaction pathways and mechanisms are unknown. *In situ* Raman spectroscopy is incorporated to facilitate collecting highly time-resolved data of the decomposition products at short residence times. This time-resolved yield data will close gaps in the understanding of active reaction mechanisms in continuous SCWG reactors and will clarify the role of heterogeneous catalytic activity at the reactor wall. A limited number of SWPO experiments are also conducted with ethanol, to elucidate the interaction of key reaction intermediates.

As an initial proof-of-concept study for using *in situ* Raman spectroscopy to quantify reaction kinetics, formic acid (HCOOH) is gasified in subcritical and supercritical water. Formic acid has two simple decomposition pathways and its first-order decomposition rates have been previously reported in the literature, allowing for a quick validation of the data collection and processing methodologies.

2. Previous SCWG Reactor Designs and Known Challenges

Industrial application of SCW processing requires an understanding of physical phenomena linked to pressure, temperature, transport properties, compound solubility, and chemical reactions. As interest in supercritical water processes has grown, research groups have built lab-scale SCWRs to study gasification, oxidation, and/or particle synthesis. A thorough literature review allowed for identification of common design solutions to standard issues in SCWG reactors, including methods for heating, pressurization, mass flow rate control, corrosion mitigation, catalysis, and effective mixing of reagent and water [20].

2.1. Batch vs. Continuous Reactors

SCWG reactors exist in batch and continuous configurations. Batch reactors are often manufactured as quartz capillary tubes, which are filled with reactants and heated to reaction temperatures, often in a fluidized bath or electric furnace. Reactions occur at a fixed temperature and pressure for a desired residence time, before the reactor is quenched, and products are recovered for sampling. Quartz creates a non-reactive and non-catalytic surface for investigations of chemical reaction kinetics and mechanisms. Industrial applications of batch reactors are limited. Continuous reactors have more complicated designs but facilitate gasification with improved process economics, higher throughput, and operational flexibility at the industrial scale. Continuous reactors are typically manufactured from nickel-base alloys, such as Inconel 625 or Hastelloy C-276, due to excellent corrosion resistant, strength at high temperatures, and a beneficial catalytic effect. Nickel significantly catalyzes gasification reactions, which offers practical benefits, but causes chemical reaction rates and mechanisms to vary considerably

between batch and continuous reactors [21]. Decomposition rates and pathways determined in quartz batch reactors and continuous nickel-base alloy reactors are not comparable.

2.2. Heating and Pressurization

Reactant pressurization in continuous SCWG reactors is accomplished with a constant flow rate pump operated in conjunction with a back pressure regulator (BPR). Pumps must be capable of reaching pressures above the critical point at a range of user-specified flow rates. Groups report using HPLC pumps [18, 22-26], diaphragm pumps [22, 27], syringe pumps [28], and piston pumps [24]. The ideal choice depends on the feedstock and flow rates needed. For example, diaphragm pumps can readily handle viscous slurries or feeds with high solid content, while HPLC pumps offer precise flow rate control, but cannot handle complex feedstocks. For studies of reaction kinetics, HPLC pumps are popular due to commercial availability, lack of flow pulsation, compact size, and ease of control.

At 25 MPa, increasing the temperature of water from 20°C to 400°C requires a heat input of 2483 kJ/kg [29, 30]. Heating water to supercritical temperatures is typically accomplished with electric resistive heaters, radiative furnaces, or fluidized baths. Unique heat transfer characteristics of supercritical water can lead to difficulty in bringing the water past the critical point. Enhanced heat transfer (HTE) and deteriorated heat transfer (HTD) can occur during the heating process due to optimal or sub-optimal thermophysical properties, and factors such as reactor geometry and the ratio of mass flux to heat flux [31]. When HTD occurs (typically due to the low thermal conductivity seen in the vapor-like regime), heat transfer from the reactor wall into the fluid is poor, which can cause wall temperatures to significantly increase. With all heating methods, care must be taken not to heat reactor walls past the safe operating limit, especially if HTD is taking

place. Immersive fluidized baths are an excellent option for maintaining isothermal conditions in the reactor section; however, they are expensive and large [32]. Contact resistive heaters offer the smallest form factor but have less precise temperature control and must be insulated to minimize heat loss [17, 22, 33]. Electric furnaces are an excellent option both for preheating and for maintaining isothermal reactor conditions, due to precise control and built-in insulation [17, 23, 24, 28, 33]. A combination of these heating methods can provide an ideal balance of cost, size, and precise control for a SCWG reactor.

2.3 Corrosion Mitigation and Material Selection

Minimizing corrosion is another thoroughly studied design challenge in SCWG reactors. The high-temperature, high-pressure (HTHP) hydrolysis environment leads to the corrosion of many common reactor materials, particularly if heteroatoms or alkali salts are present. Marrone et al. [13] identified four primary categories of corrosion control strategies in a review on the subject: (i) preventing corrosive species from interacting with the reactor walls, (ii) forming a corrosion-resistant barrier on the reactor wall, (iii) selecting reactor wall materials resistant to corrosion, and (iv) tuning reactor operating conditions to minimize regions of severe corrosion. For lab-scale reactors used to study reaction kinetics, preventing contact with reactor walls could introduce a concentration gradient in the flow, invalidating the assumption of a plug-flow regime. The catalytic wall effect would also be diminished by preventing contact or by forming a barrier on the inside surface of the reactor. For lab-scale reactors, the most practical corrosion mitigation technique is an appropriate material selection.

Nickel-based alloys resist corrosion in the presence of salt precipitates that are likely to form during the gasification of complex feedstocks. The majority of continuous SCWRs have been

constructed from Hastelloy C-276 or Inconel 625 due to the combination of excellent corrosion resistance, high strength at elevated temperature, and commercial availability. Tang et al. [16] demonstrated that these two alloys tend to gain mass in the presence of corrosive species, while stainless steel alloys tend to lose mass. A buildup of deposits can be cleaned periodically, but lost mass in stainless steel reactors would eventually lead to system failure. Also, multiple studies have proven that nickel is catalytic to gasification reactions and the WGS reaction, thus the presence of nickel in reactor walls leads to more complete gasification with higher hydrogen yields. Groups studying reactor geometry and the catalytic wall effect reported that higher surface-to-volume (S/V) ratios resulted in faster and more complete gasification. The catalytic effect was seen to diminish slightly with longer reactor use, an effect referred to as "reactor aging". This is due to buildup of carbon or intermediate compounds on reactor walls. While aged reactors are less catalytic, they show more consistent catalytic behavior. Titanium alloys were also shown to perform well at supercritical conditions with corrosive species present, but titanium does not provide beneficial catalytic activity [16].

2.4. Reagent Mixing

Two mixing strategies have been reported: (i) premixing water and reagents before heating, and (ii) injecting cold reagents in supercritical water. Premixing allows for solid or viscous feedstocks to reach operating pressures as an emulsion. One drawback to premixing is char and tar formation in the preheater, due to slow heating of the reactant [13, 22]. Char formation is reduced by rapidly heating the reagents to supercritical temperatures, which is accomplished with post-critical injection. Post-critical injection creates a definitive reaction start time, allowing for reasonably accurate calculations of residence time for chemical kinetic studies [6, 34, 35]. The

design of an appropriate mixing section introduces challenges. In systems with low flow rates, the high kinematic viscosity of supercritical water yields low Reynolds numbers, resulting in laminar mixing limited by molecular diffusion. Larger reactors and higher flow rates promote rapid mixing through an increase in Reynolds number. In general, optimization of the operating conditions and the critical reactor dimension is required to achieve adequate mixing rates for plug flow conditions in the reactor section. Most authors do not report mixing section design, but variation in mixing profiles could explain discrepancies in reported reaction pathways and rates [12].

2.5. Reactor Clogging

A significant challenge with SCWG of real feedstocks is reactor clogging, either from char buildup of precipitation of insoluble compounds. Salts, either added as catalysts or naturally present in biomass feedstocks, have low solubility in supercritical water [1]. Alkali metal salts exist in molten form at temperatures above 300°C, and adhere to reactor surfaces, corroding metal and poisoning catalytic pores. Buildup can be cleaned by periodic flushing with cold water, but frequent cooldown of the system is impractical. Salt precipitation can be suppressed by avoiding the addition of alkali metal salts, or by pretreatment to remove alkali compounds.

2.6. Heat Exchanger and Back Pressure Regulator

Once the supercritical effluent exits the reactor section, it is typically quenched by a heat exchanger and throttled to atmospheric pressure by a BPR. The design of the heat exchanger is subtly important for chemical reaction studies. *In situ* Raman spectroscopy has demonstrated that for a heat exchanger that is not oriented vertically, flow separation can lead to accumulation of insoluble gases within the heat exchanger. Separation occurs when the effluent transitions to a

two-phase flow below the critical point. At subcritical temperatures in the range of 240°C to 260°C, formic acid was shown to be an intermediate of the WGS reaction [36]. Synthesis of formic acid in the heat exchanger due to trapped gases would lower H_2 yields and would lead to inaccuracies in chemical kinetic studies. The exchanger should be oriented vertically, taking advantage of buoyancy effects to allow insoluble gases to exit [37].

BPR selection is important, as solid precipitates can clog ports, and the wetted material must be compatible with corrosive reaction products or refractory organic solvents in the effluent stream. Diaphragm style BPRs are the most common choice for SCWG reactors, with pressure control from spring loading or from dome loading.

2.7. Reactor Monitoring, Control, and Data Acquisition

Real-time process monitoring allows for safe operation of SCWG systems prone to clogging, corrosion, leaks, or structural failure. Knowledge of temperature, pressure, residence time and chemical composition are required for chemical reaction rate studies. Some standard monitoring approaches are reported in the literature. Thermocouples immersed in the flow directly measure the reactor temperature with a fast response time but are exposed to corrosion. Thermowells can reduce exposure of thermocouples to corrosion but reduce precision of temperature measurements. Reactor pressure can be monitored in the cold zones, preferably before any preheaters, where a sudden rise in pressure would indicate a clog downstream. Installation of rupture discs or pressure relief valves on the front end of the reactor is recommended.

The vast majorities of SCWG studies rely on *ex situ* analysis techniques to quantify reaction products, at differing levels of thoroughness. However, *ex situ* analysis is time-consuming, and standard techniques such as gas chromatography (GC) or total organic carbon

(TOC) analysis only allow for calculation of gasification efficiency, hydrogen efficiency, and/or carbon conversion efficiency. For detailed studies of chemical kinetic rates and reaction pathways, detailed knowledge of all product yields is needed. High pressure liquid chromatography (HPLC), Raman spectroscopy, Fourier transform infrared (FTIR) spectroscopy, and nuclear magnetic resonance (NMR) spectroscopy can all be used to analyze liquid products. In general, *ex situ* analysis is most suited to studies where only gasification efficiency measurements are needed.

Alternatively, *in situ* product identification has the potential to significantly speed chemical kinetic studies and could be advantageous for automated process control. Raman spectroscopy [17] with an excitation wavelength in the visible range is a promising *in situ* process monitoring technique for effluent composition analysis. Raman spectroscopy in a continuous flow SCWG was first demonstrated by Sandia National Laboratories [38, 39] to investigate the oxidation kinetics of methanol and isopropyl alcohol in supercritical water. However, long-term use of the optical cell in the HTHP environment led to cell failure due to thermal expansion and thermal cycling. A sapphire or diamond window is necessary for optical access to the flow. In the HTHP environment, it becomes a significant design challenge to keep the window sealed and intact. Thermal stresses can cause the window to fracture, and gaskets (typically gold or graphite) creep due to thermal cycling [40]. Several researchers have designed and used HTHP Raman cells that address the sealing issues, although most of these cells are designed for batch-type experiments and would be expensive and difficult to reproduce from scratch for a continuous configuration [41-46]. Even with the recent development of commercially available immersion Raman probes for high-pressure applications, use in HTHP environments remains difficult.

2.8. Performance Metrics

From a system perspective, effective SCWG is best described as complete conversion of the mass and energy content of the original feedstock into gaseous products. Three performance metrics are commonly used in the literature to quantify this conversion: (i) gasification efficiency (GE), (ii) carbon conversion efficiency (CE), and (iii) hydrogen efficiency (HE). GE is defined as the ratio of total mass of the gaseous products to initial mass of the feedstock, expressed mathematically as:

$$GE(\%) = \frac{m_{H_2+}\, m_{CO_2+}\, m_{CO+}\, m_{CH_4+}\, m_{C_xH_y}}{m_{feedstock}} * 100 \quad (1)$$

GE is an effective metric for quantifying the overall completeness of gasification reactions. CE is another metric used to quantify completeness of gasification, defined as the ratio of moles of carbon in the gaseous product to moles of carbon in the feedstock:

$$CE(\%) = \frac{2n_{CO_2+}\, n_{CO+}\, n_{CH_4+x}\, n_{C_xH_y}}{n_{C,feedstock}} * 100 \quad (2)$$

Another, less frequently used, metric is HE, defined as the ratio of moles of hydrogen in the gaseous product to moles of hydrogen in the feedstock:

$$HE(\%) = \frac{2n_{H_2+}\, 4n_{CH_4+y}\, n_{C_xH_y}}{n_{H,feedstock}} * 100 \quad (3)$$

HE and GE values from SCWG can be well above 100%, due to the prominent role of the WGS reaction during gasification.

2.9. Summary of Reactor Design Review

Several key trends emerged through the reactor design review, and the resulting insights were incorporated in the resulting reactor design. For example, using HPLC pumps in conjunction

with a BPR was common for internal pressure control, and was the configuration that was ultimately chosen. Insights towards suitable alloys for reactor components ensured that corrosion and operating temperatures were not of concern.

A continuous, tubular reactor with post-critical reagent injection was chosen as the preferred configuration for conducting reaction kinetic studies, leveraging the plug-flow assumption. The use of *in situ* Raman spectroscopy for data collection was selected as a suitable product analysis method, as Raman is particularly amenable for analyzing aqueous mixtures. A more detailed description of the reactor components and design is provided in Chapter 4.

3. Known Model Compound Decomposition Routes and Rates

A first step in determining relevant model compounds to study was to review prior work investigating the SCWG of model compounds in continuous supercritical water reactors [12]. This review focused exclusively on gasification of model compounds in continuous reactors, due to the aforementioned differences in kinetic rates between batch and continuous reactors. This review also did not consider SCWG of model compounds in the presence of an externally added homogenous or heterogeneous catalyst.

Many researchers have investigated the decomposition behavior of model compounds in subcritical and supercritical water, quantifying the effects of temperature, pressure, residence time, and feedstock concentration on the gasification process. In some cases, other variables have also been studied, including reactor geometry, heterogeneous catalytic activity of various alkali and transition metals, and homogenous catalytic activity of mixed feedstocks.

Interest in gasifying biomass has prompted studies where phenolic compounds are gasified as model compounds for lignin [47-49], glucose and fructose are gasified as model compounds for cellulose [22, 24, 25, 33, 34, 50-57], alcohols are used as model compounds for common liquid intermediates and byproducts, [7, 21, 58-66], and amino acids are used as model compounds for proteins found within biomass and agricultural waste [67-74]. Often chemical reaction mechanisms, routes, and kinetic rates are not reported, with gasification efficiency or carbon efficiency being the most frequently reported metrics. Much previous work investigated the gasification of glucose, due to its prevalence in biomass feedstocks and low temperatures needed for gasification. Little work has been done investigating the gasification kinetics and reaction pathways of model alcohols, such as ethanol and isopropyl alcohol.

3.1. Model Aromatic Compounds

Known refractory compounds in the SCWG of biomass feedstocks include phenol, benzene, furfurals, and char. Non-catalyzed SCWG is not effective at cleaving C-C bonds, thus decomposition of phenol and benzene are typically rate-limiting steps in the gasification of complex biomass. The gasification rates of model aromatic compounds, such as phenol (C_6H_5OH), benzene (C_6H_6), and guaiacol ($C_7H_8O_2$), are of interest in determining necessary operating parameters for gasifying biomass feedstocks. Phenol is particularly noteworthy, as it is a stable intermediate product present in the decomposition routes of cellulose and biomass [47].

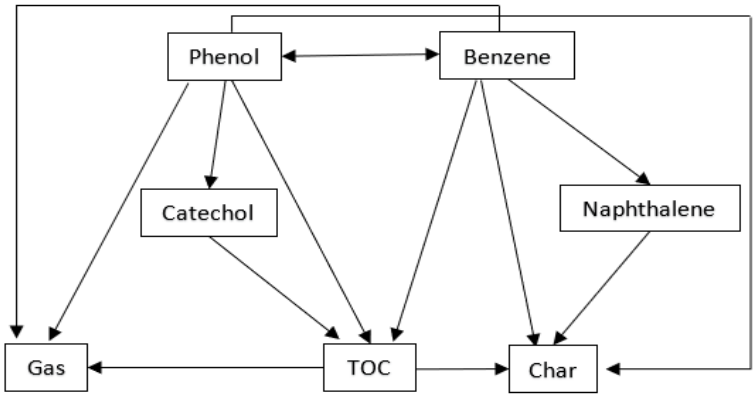

Figure 2: Proposed reaction pathways for phenol and benzene in SCWG from [49].

In a 2013 study, Yong and Matsumura [49] performed a kinetic analysis of phenol and benzene decomposition in a continuous SCWR. Reactants were mixed with preheated supercritical water to obtain rapid heating and to minimize char formation. Gasifying the two compounds at temperatures from 370 to 450°C, 25 MPa, and residence times from 0.5 to 100 s, the group determined activation energies and pre-exponential factors for the overall decomposition reaction and proposed kinetic parameters for intermediate reactions. A proposed decomposition pathway for the two compounds is shown in Figure 2, and Arrhenius parameters for the decomposition reactions are shown in Table 1. Notably apparent in Figure 2 is that phenol and benzene decompose

along two competing reaction pathways, one leading to gaseous products, and the other leading to char. Knowledge of the rates and activation energies along these competing pathways can lend insight towards optimal reactor operating conditions for maximum gaseous yield.

Castello et al. [26] investigated the presence of phenol on the gasification rates of glucose to understand the decomposition behavior of heterogeneous biomass. No change in the conversion rate of glucose was observed, but H_2 production was inhibited in the presence of phenol, while CH_4 production was promoted. Weiss-Hortala et al. [75] also studied the influence of phenol on glucose gasification and found that the presence of phenol decreased gas yield, likely due to the influence of phenol on the intermediate products of glucose gasification. The results show that gasification pathways are not entirely decoupled.

Yong and Matsumura [48] monitored the decomposition of guaiacol in sub- to supercritical water and reported corresponding Arrhenius parameters. Experiments were conducted at temperatures from 300 to 450°C, 25 MPa, and residence times from 0.5 to 40 s. Reactants were mixed with preheated water for rapid heating. Analyzing gaseous, liquid, and solid products, guaiacol was found to decompose rapidly into phenol, benzene, o-cresol, m-cresol, gaseous products, and char in the subcritical and supercritical water environment. Char formation from guaiacol gasification was so significant that reactant concentration had to be limited to 0.1 wt% to prevent reactor plugging. Arrhenius parameters for overall guaiacol decomposition is presented in Table 1. It should be noted that although guaiacol decomposes rapidly into intermediate products, those intermediates products decompose slowly in the gasification environment. Therefore, complete conversion to gaseous products takes significantly longer than is seemingly indicated by the reported Arrhenius parameters.

3.2. Model Carbohydrates

Glucose ($C_6H_{12}O_6$) is the most thoroughly studied model compound in SCWG due to its prevalence in biomass feedstocks. Most studies of glucose gasification report only gasification efficiency and do not calculate kinetic rates or analyze decomposition routes. Initial studies of glucose gasification in supercritical water determined that complete gasification could be achieved after 20 s at 600°C and 34.5 MPa without significant char or tar formation [55, 56].

Kabyemela et al. [53] investigated the effects of temperature and pressure on decomposition kinetics and intermediate products of glucose gasification in supercritical water. High temperatures significantly increased the decomposition rate, and pressure dependence was found to be minor. Intermediate products from gasification at residence times of 0.02 to 2 s were identified as fructose, saccharinic acids, erythrose, glyceraldehyde, dihydroxyacetone, 1,6-anhydroglucose, pyruvaldehyde, and 5-hydroxymethylfurfural (5-HMF). Aida et al. [33] identified similar intermediate compounds from glucose gasification – fructose, erythrose, glycolaldehyde, glyceraldehyde, hydroxyacetone, lactic acid, 5-HMF, and furfural.

Glucose has been used as a model compound to investigate novel reactor designs. Goodwin and Rorrer [50] gasified glucose at temperatures from 650 to 750°C at a pressure of 25 MPa in a microchannel reactor, characterized by an enhanced heat transfer surface area and small inner reactor diameters. The microchannel design was credited with enhancing gasification rates, and intermediate products were identified as acetic, lactic, formic, and propanoic acids, 5-HMF, 2,5-hexanedione, and furfural. A discrepancy with reported intermediate products relative to [33] and [53] may be due to the high gasification temperatures. Hao et al. [76] also demonstrated that small inner reactor diameters increased the gasification rate of glucose, an affect attributed to a higher catalytic S/V ratio. While small reactor diameters may increase gasification rates, they are not

practical for industrial systems gasifying real feedstocks, due to the propensity for solid formation and clogging in small diameter reactors.

Promdej and Matsumura [54] gasified glucose at temperatures from 300 to 460°C, 25 MPa, and 1.5 wt% initial glucose concentration to determine global Arrhenius parameters. Subcritical temperatures led to char formation due to the polymerization of refractory intermediates 5-HMF and furfural. Hendry et al. [34] studied glucose gasification at temperatures from 750 to 800°C, 25 MPa, concentrations of 10 to 15 wt%, and residence times from 4.0 to 6.5 s. The intent was to investigate economically feasible operating conditions for gasifying glucose. Increasing the reaction temperature to 800°C from 750°C significantly increased gasification efficiency and decomposition rate. Table 1 presents reported Arrhenius parameters for glucose decomposition from [34] and [54].

Fructose ($C_6H_{12}O_6$) has also been studied as a model carbohydrate, due to its presence as an intermediate of glucose gasification, and its presence in agricultural waste feedstocks [24, 25, 51]. Kabyemela et al. [51] gasified fructose at temperatures from 300 to 400°C, pressures from 25 to 40 MPa, and residence times from 0.02 to 2 s, in order to determine decomposition pathways and rates. Intermediate products from fructose decomposition were similar to glucose intermediates, including 5-HMF, dihydroxyacetone, glyceraldehyde, erythrose, pyruvaldehyde, acetic acid, and formic acid. A proposed general reaction pathway for glucose and fructose decomposition in subcritical and supercritical water is presented in Figure 3.

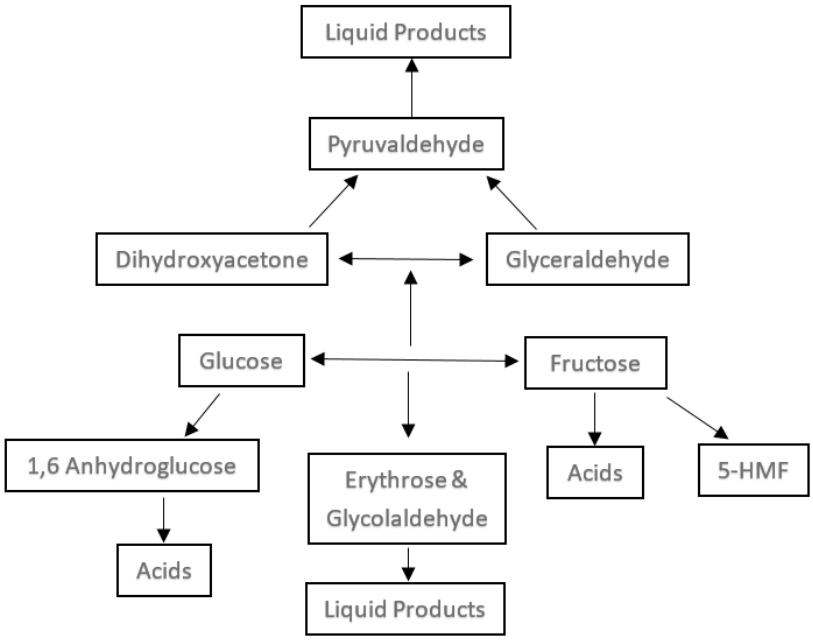

Figure 3: Generalized reaction pathways for glucose and fructose in sub- and supercritical water [51].

Aida et al. [52] studied fructose gasification at residence times from 0.14 to 0.78 s, identifying intermediate products as glyceraldehyde, dihydroxyacetone, pyruvaldehyde, lactic acid, and 5-HMF, in good agreement with [51]. Nanda et al. [24] gasified fructose at residence times from 30 to 75 s, temperatures from 550 to 700°C and concentrations from 4 to 10 wt% to determine optimum gasification parameters for maximizing H_2 yield. The highest tested temperature and lowest tested reactant concentration were observed to yield maximum H_2, while a residence time of 60 s was determined to be optimal. At residence times beyond 60 s, methanation reactions became significant in converting H_2 to CH_4. Higher H_2 conversion at high temperatures and low feedstock concentration is a common trend for the gasification of real biomass as well.

Nanda et al. [57] gasified lactose ($C_{12}H_{22}O_{11}$) as a model compound for dairy industry waste. The same experimental conditions were tested as in [24], and maximum H_2 yield was again observed at maximum temperature, minimum feedstock concentration, and a 60 s residence time.

3.3. Model Alcohols

Motivated by the potential to use methanol (CH_3OH) for chemical storage of hydrogen fuel, several research groups have investigated methanol decomposition in supercritical water. Boukis et al. [62, 63] studied methanol decomposition in supercritical water at temperatures from 400 to 600°C, pressures from 25 to 45 MPa, residence times from 3 to 100 s, and feed concentrations from 5 to 64 wt%. Gaseous products and overall conversion were analyzed. Decreasing initial methanol concentration led to a higher yield of H_2, while increasing residence time led to lower yields of H_2 and higher yields of CH_4, due to the methanation reaction. Complete conversion of methanol was achieved after 4 s at 600°C. No rate parameters were reported.

Hack, Masten, and Buelow [58] gasified methanol and ethanol (C_2H_5OH) to determine activation energies and hydrolysis rates. Reaction products for methanol decomposition were identified as H_2, CH_4, CO_2, and formic acid. Bennekom et al. [59] investigated methanol gasification at temperatures from 450 to 650°C, residence times from 6 to 173 s, and feed concentrations from 3 to 20 wt%. The authors propose that methanol decomposes through intermediate products of formaldehyde and formic acid, which each decompose rapidly to gaseous products. Proposed first-order activation energies from [58] and [59] are reported in Table 1.

Glycerol ($C_3H_8O_3$) is a common byproduct of biodiesel production and could be a potential H_2 fuel source. Buhler et al. [65] gasified glycerol at temperatures from 350 to 575°C, pressures from 25 to 45 MPa, residence times from 32 to 165 s, and varied concentrations. Reaction products were identified as methanol, acetaldehyde, allyl alcohol, propionaldehyde, acrolein, ethanol, formaldehyde, and gaseous products. Buhler concluded that competing ionic reactions and free radical degradation pathways led to non-Arrhenius behavior for glycerol decomposition. May et al. [64] also gasified glycerol in a continuous reactor at 510 to 550°C, 35 MPa, and residence times

from 2 to 10s. Major intermediate compounds were identified as acetaldehyde, hydroxyacetone, and acetic acid. Antal Jr. et al. [7, 66] also reported products of glycerol gasification at 500°C as acetaldehyde, acrolein, and gaseous products.

Guo et al. [60] investigated the effects of gasification parameters on H_2 yield from glycerol gasification. A temperature of 600°C and a residence time of 9 s (highest values tested) were found to result in the highest yield of H_2. First-order kinetics were assumed for the temperature range of 445 to 600°C and Arrhenius parameters were reported. Bennekom et al. [59] gasified glycerol at temperatures from 450 to 650°C, residence times from 6 to 173 s, and feed concentrations from 5 to 20 wt%. First-order activation energies were reported. Results from [59] and [60] are presented in Table 1.

3.4. Model Amino Acids

Decomposition of amino acids in supercritical water has been studied to understand the behavior of proteins in supercritical water, for processing agricultural and fish waste. The differentiating factor between amino acids is the functional group, which is hypothesized to be a key influence on overall gasification rates and products. To quantify this behavior, Islam et al. [69] gasified various amino acids as model compounds for larger proteins to determine the effects of temperature on the composition of intermediate and final products. Glycine and alanine were identified as common intermediate gasification products of more complex amino acids; focus was placed on glycine and alanine as key compounds in the gasification of proteins.

Glycine ($C_2H_5NO_2$) is the chemically simplest amino acid, containing a single H atom as its functional group. Samanmulya and Matsumura [74] investigated glycine gasification at temperatures from 500 to 650°C, a pressure of 25 MPa, and feedstock concentrations of 1.0, 3.0,

and 5.0 wt%. Higher concentration led to a decrease in gasification efficiency, due to the production of tar and char, while higher temperatures increased gasification efficiency.

Sato et al. [70] investigated the subcritical decomposition of glycine, at temperatures from 200 to 340°C and a pressure of 20 MPa. Gaseous products were not measured or identified, but key liquid decomposition products were specified as ammonia, methylamine, glycolic acid, and formic acid.

In 2007, Klingler et al. [67] gasified glycine at temperatures from 250 to 450°C, and a pressure of 35 MPa. A strong temperature dependency was found, with drastic changes in decomposition rates over the experimental temperature range. Liquid products were identified as methylamine, diketopiperazine, glycolic acid, and formaldehyde.

Alanine ($C_3H_7NO_2$) is another chemically simple amino acid, serving as a useful model compound. In a separate study from Samanmulya et al. [72], alanine was gasified at temperatures from 500 to 650°C, at 25 MPa, fixed mass flow rate of 2 g/min, and reactant concentrations of 1.0, 2.0, and 3.0 wt%. No change was observed in gasification efficiency for varied reactant concentrations, indicating first order decomposition behavior. Additionally, carbon efficiency was highly temperature dependent. Results showed that the gasification rate for alanine is comparable to glycine, despite the different functional groups. Sato et al. [71] investigated the decomposition of alanine at subcritical conditions, identifying liquid products as ammonia, ethylamine, carbonic acid, lactic acid, and pyruvic acid. Klingler et al. [67] also studied sub- and supercritical gasification of alanine, identifying liquid reaction products as lactic acid, ethylamine, and acetaldehyde.

Both Samanmulya et al. [72] and Sato et al. [71] gasified more complex amino acids to determine carbon conversion rates, decomposition rates, and final products. Gasifying valine

($C_5H_{11}NO_2$), leucine ($C_6H_{13}NO_2$), and proline ($C_5H_9NO_2$) led to the conclusion that the functional group of the amino acid has a significant effect on conversion rates and final products yields, as does the reaction temperature. Arrhenius parameters of all amino acids studied [67, 70-72] are summarized in Table 1.

3.5. Formic Acid

Some intermediate gasification products are common across a range of compounds. One is formic acid, which has been identified as an intermediate product from the gasification of glucose [50], fructose [51], methanol [58], and glycine [70]. One can assume that formic acid will be an intermediate from the gasification of any real biomass feedstock.

In 1998, Yu and Savage [77] studied the gasification of dilute formic acid in a continuous SCWR, to analyze the decomposition pathways and rates under hydrothermal conditions. Tests were conducted at temperatures between 320 and 500°C, pressures between 18 and 30.7 MPa, and residence times between 1.4 and 80 s. Major decomposition products were consistently CO_2 and H_2, indicating that decarboxylation is the dominant reaction pathway, as shown below. CO was also observed as a reaction product in low concentrations, suggesting the existence of a dehydration reaction pathway:

$$HCOOH \rightarrow H_2 + CO_2 \quad (4)$$

$$HCOOH \rightarrow H_2O + CO \quad (5)$$

For temperatures above 420°C, decomposition happened too rapidly for kinetic rates to be determined. Pressure dependency was noted for decomposition occurring near the critical point, possibly indicating a density-dependent reaction mechanism. Kinetic rates were calculated for temperatures from 320 to 420°C and a pressure of 25.3 MPa. Arrhenius parameters for the first-

order decomposition of formic acid were calculated based on these kinetic rates and are presented in Table 1.

Zhang et al. [78] gasified formic acid in a continuous SCWR, at temperatures between 550 and 650°C, pressures between 24 and 30 MPa, residence times between 16 and 46 s, and formic acid concentrations between 0.05 and 0.7 M. Dominant reaction products were reported as H_2 and CO_2, with minor yields of CO. The authors reported that gasification with a high concentration of formic acid led to the formation of formaldehyde and methanol, decreasing hydrogen yield. Kinetic rates were not reported.

Table 1: Arrhenius parameters of model compounds in SCWG, from reviewed literature.

Compound	Temperature Range (°C)	Pressure (MPa)	Pre-Exponential Factor 'A' (s^{-1})	Activation Energy 'E_A' (kJ/mol)	Source
Guaiacol	300 - 450	25	6.52×10^1	32.40	[48]
Phenol	370 - 450	25	7.72×10^1	53.06	[49]
Benzene	370 - 450	25	2.78×10^4	91.16	[49]
Glucose	300 - 460	25	6.9×10^7	95.54	[54]
Glucose	750 - 800	22	1.2×10^3	70	[34]
Methanol	324 - 524	31.5	Not reported	164	[58]
Methanol	450 - 650	26	Not reported	191	[59]
Ethanol	324 - 524	31.5	Not reported	145	[58]
Glycerol	445 - 600	25	7.94×10^5	104.5	[60]
Glycerol	450 - 650	26	Not reported	196	[59]
Glycine*	200 - 340	20	3.51×10^{13}	166	[70]
Glycine	250 - 450	34	3.6×10^{11}	160	[67]
Alanine*	200 - 340	20	2.65×10^{12}	154	[71]
Alanine	250 - 450	34	1.4×10^{12}	156	[67]
Serine*	200 - 340	20	9.85×10^{12}	149	[71]
Aspartic Acid	500 - 650	25	5.40×10^{13}	148	[72]
Formic Acid	320 - 420	25.3	1.58×10^6	85.77	[77]

* Subcritical Decomposition Parameters

3.6. General Trends and Observations

Across all compound classes, it was found that higher temperatures, longer residence times, and lower feedstock concentrations resulted in more complete gasification, and many compounds exhibited first-order decomposition behavior when gasified in the absence of other compounds at

low concentrations. Observed first-order decomposition behavior may be due to the low feedstock concentrations used, as water is known to catalyze and participate in many gasification reactions. Some studies indicate that higher feedstock concentrations result in slower decomposition, likely due to increased feedstock-feedstock reactions and decreased feedstock-water reactions, as evidenced by increased char formation, and supported by the known role of water molecules in decomposition reactions. Pressure was only shown to have an effect on decomposition rates around the critical point, where water is highly compressible, and pressure changes result in significant changes in density, viscosity, and other thermophysical properties.

Few studies on the gasification of model compounds in continuous reactors reported chemical kinetic rates or overall Arrhenius parameters, due to the experimental challenges of collecting and identifying liquid and gaseous products using standard *ex-situ* analysis techniques. The standard for many gasification experiments is to separate liquid and gaseous products, use gas chromatography to analyze the yield of gaseous products (H_2, CO, CO_2, CH_4, and occasionally light hydrocarbons) and calculate GE. This lends insight into how complete the gasification process is for given process parameters but leaves many open questions about the chemical reactions taking place in the SCWG environment. Many groups also used a TOC analyzer on liquid products to calculate CE. Only a handful of researchers identified liquid product yields, and only a few reported decomposition rates or overall Arrhenius parameters [12].

Of the reported Arrhenius parameters, insufficient data exist to perform proper cross-validation between studies. An Arrhenius plot of reported Arrhenius parameters is shown in Figure 4. Kinetic rates were calculated for compounds at temperatures from 375 to 750°C, using the standard first-order Arrhenius expression relating kinetic rate to temperature:

$$\ln(k) = \ln(A) - \frac{E_A}{RT} \quad (6)$$

Figure 4 lends immediate insight into which compounds decompose fastest in the SCWG environment. Glycine, alanine, and glucose decompose rapidly, while phenol and benzene are slowest to decompose at supercritical conditions. Notably absent from this plot, as mentioned before, are simple model alcohols such as methanol, ethanol, and isopropyl alcohol. Also, reported parameters should be validated by subsequent studies.

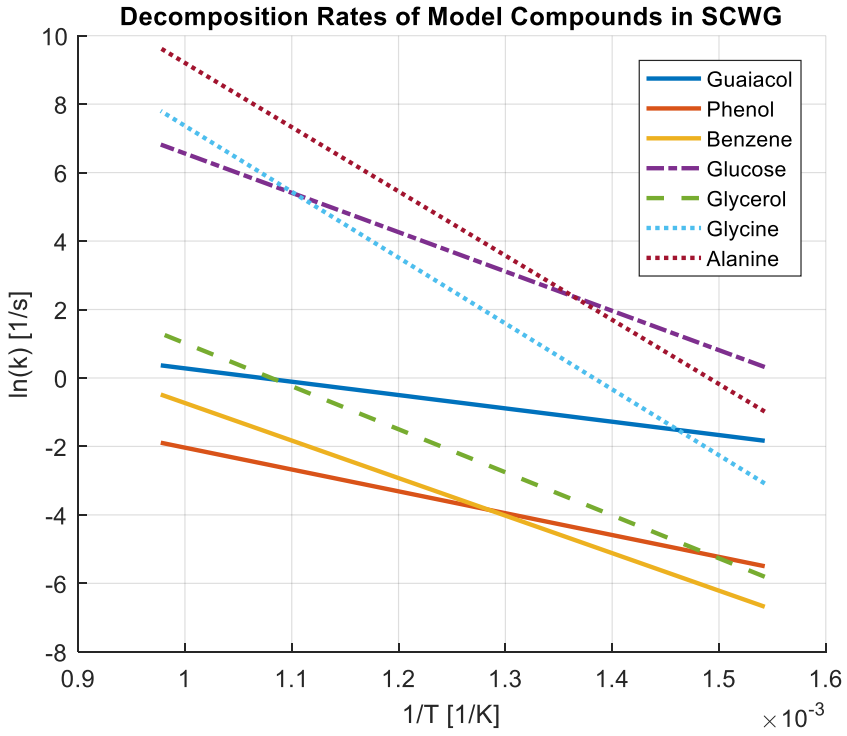

Figure 4: Arrhenius plot of decomposition rate constants of model compounds in SCWG environment.

Formation of benzene, phenol, furfurals, and char as refractory intermediate compounds is a challenge for the design of commercial reactor systems. In practical applications, high reactor temperatures (>600°C) may be required to minimize reactor size, promote rapid gasification, and increase throughput. Alternatively, the use of a catalyst may be required to increase reaction rates. An important consideration is that reported rates are linked to reactor geometry, S/V ratio, and

catalytic wall effects. Reactor configurations are often minimally described, and these uncertainties may lead to discrepancies in observed rate constants.

One prevalent finding is the importance of the WGS reaction and methanation reactions to the final gaseous yield. If a reactant is fully gasified, the concentrations of H_2, CO, CO_2, and CH_4 are highly dependent on these mechanisms. The fact that SCWG takes place in water allows for the conversion of CO and H_2O to H_2 and CO_2 via the WGS reaction, which is catalyzed by nickel reactor walls [1]. Methanation converts CO or CO_2 and H_2 into CH_4, which can lower H_2 yields.

Based on reported gasification results, an optimum continuous SCWG reactor for industrial applications must be able to reach temperatures of at least 700°C, with controllable residence times and feedstock concentrations. Reactors should also be constructed to maximize the catalytic wall effect by maximizing S/V ratio.

4. Supercritical Water Reactor Design

A continuous, tubular SCWR is used for all experiments, designed to operate at pressures up to 35 MPa, temperatures up to 560°C, and residence times of 3 to 120 s. A system schematic is shown in Figure 5.

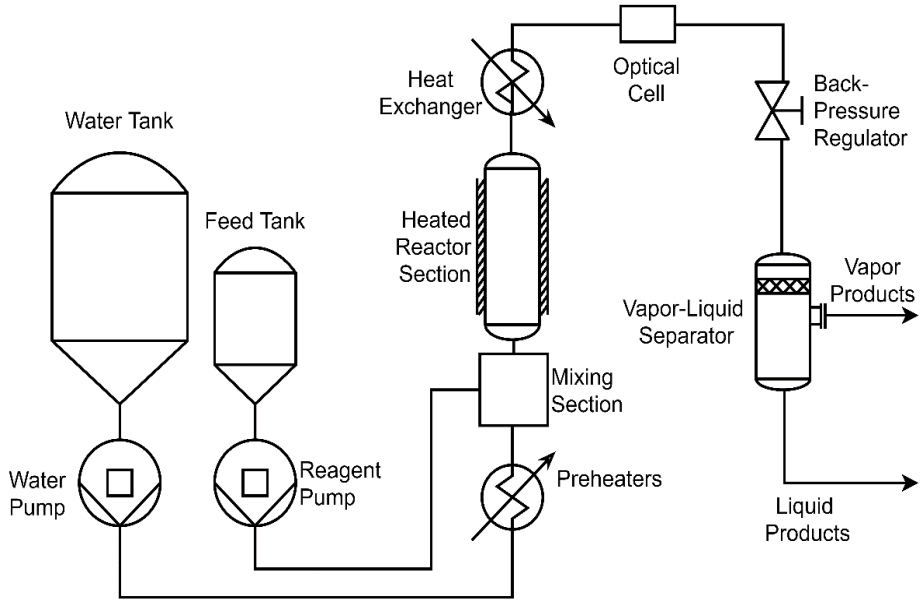

Figure 5: Supercritical water gasification reactor schematic.

Two SSI (State College, PA) HPLC pumps provide constant, user-defined flow rates of reagent and deionized (DI) water (ρ = 18.2 M-Ω) into the system, while an Equilibar (Fletcher, NC) BPR controls the internal reactor pressure. Separate pumps facilitate independent selection of mass flow rates, residence times, and the initial mass fraction of the reagent. Two heating sections preheat water to supercritical conditions: a 2000 W TEMPCO (Wood Dale, IL) coil-heater and an 1800 W OMEGA (Norwalk, CT) ceramic radiant cylinder heater.

Reagents are injected without preheating into the bulk flow of supercritical water using a custom mixing section. Post-critical injection of cold reagent is ideal for rate studies, as it establishes a clear reaction initiation point, minimizes char formation, and prevents pyrolysis or

decomposition reactions in the reagent line. The mixing section introduces the reagent via four axisymmetric 0.254 mm inner diameter (ID) injector ports into a central flow channel with a 3.05 mm ID. A challenge for post-critical injection is quickly obtaining a well-mixed flow and a uniform temperature distribution. A numerical computational fluid dynamic (CFD) study was performed to design the mixing section, ensuring rapid mixing and heating in the laminar and transitional (to turbulence) flow regions in the reactor; this process is detailed in Tiwari et al. [79]. The reactor is assumed to function in a plug flow reactor (PFR) configuration.

After mixing, the reagents enter an isothermal, Inconel 625 reactor section with an internal volume of 18.6 and an ID of 3.05 mm, giving a S/V ratio of 13.1 cm^{-1}. All high-temperature components are manufactured from Inconel 625, due to excellent corrosion resistance and strength at elevated temperatures. The reactor section is coiled to induce Dean vortices, which minimizes the potential for flow profile to affect observed kinetic rates. Such variation could lead to mass transfer limitations of the catalytic wall effect. A 700 W OMEGA radiative cylinder heater maintains the isothermal conditions in the reactor section, which is verified with two type-K thermocouples in contact with the flow after the mixing section and before the heat exchanger. The reactor is followed by a custom-built vertical heat exchanger, which rapidly quenches high-temperature reactions. A Raman immersion ball probe from MarqMetrix (Seattle, WA) is located immediately after the heat exchanger for *in situ* monitoring of product species in the quenched effluent stream.

4.1. Residence Time

To estimate the reaction residence time, the reactor is assumed to be operated as a PFR, removing the need to consider concentration gradients or fluid property variations. Molecular

concentration in the direction of flow is assumed to be a function only of residence time. Reported residence times for all experiments are calculated based on the internal volume of the reactor (18.6 mL) and the density of water at reaction conditions. Because the density of reactants and reaction products at reaction temperatures and pressures are not well reported, and because molecular composition changes through the reactor section, it is not possible to consider the effects of reactant and product densities on residence time. The point of reagent introduction in the mixing section is assumed as the reaction initiation point ($t = 0$), while the inlet port of the heat exchanger is assumed as the reaction termination point.

4.2. In Situ Raman Spectroscopy

A Raman immersion ball probe from MarqMetrix (Seattle, WA) allows for *in situ* monitoring of product species concentrations. The Raman spectroscopic cell is positioned in the low-temperature region to simplify quantitative spectroscopy, and to avoid issues with thermal expansion and sealing [12, 20]. Raman spectroscopy is ideal for *in situ* product identification and quantification in aqueous mixtures, as water has a weak Raman signal which offers a large spectral "window" for analyzing the effluent, yet its characteristic peaks can be used as an internal standard to aid with quantitative calibration. By varying residence time and/or reactor temperature, the effect of process parameters on the extent of reactions is investigated without having to collect products and perform *ex situ* analysis for each parameter.

The original goal was to place the Raman optical cell in the HTHP zone of the reactor, between the reactor section and the heat exchanger shown in Figure 5. However, initial tests of the MarqMetrix immersion Raman probe in the HTHP environment led to cell failure after a single experiment at temperatures above 300°C. The Raman cell is fabricated from Inconel 625, except

for a sapphire ball lens, which provides optical access and signal focusing. A backing nut holds the sapphire ball in place with a gold gasket on the flow side, providing a tight and non-reactive seal at ambient temperatures. Thermal expansion and gasket creep cause failure at high temperatures. Varying the torque applied by the backing nut does not remedy the issue. At high torques, the stress caused by thermal expansion of the surrounding Inconel block causes the sapphire ball to crack. At lower torques, the cell leaks upon cooldown, presumably due to differences in thermal expansion between sapphire and Inconel. Creeping of the gold gasket, as noted by Sandia National Labs [40] may also cause the cell to leak during cooldown. As a solution, a copper gasket is added between the backing nut and the ball, which allows for operation at temperatures up to 420°C. The copper gasket distributes force from the backing nut more evenly along the sapphire, resolving the issue of window cracking.

With the Raman cell operating successfully at high temperatures, the decomposition of formic acid is monitored *in situ* at temperatures from 365 to 420°C. In theory, the cell placed in the HTHP reactor zone allows for the identification of reaction intermediates (such as free-radicals and ionic compounds) and products in a single fluid phase. Multiple trials show that the optical function of the Raman cell is lost at temperatures near 400°C and above, as shown in Figure 6. It is unclear whether the reason for this is optical, spectral, or mechanical. It is not due to cell failure, as the optical cell functions perfectly when cooled to room temperature. Some variability in the data collected at high temperatures is expected due to temperature-dependent spectral effects and decreased densities at high temperatures. The magnitude of the temperature dependency shown by the data presented in Figure 6 demonstrates that accurate quantitative analysis of the high-temperature signals is challenging. Any quantitative measurements would require correcting for the density of reaction products, which are poorly tabulated at HTHP conditions.

For reliable and consistent use of a Raman cell in the HTHP environment, two design challenges must be addressed. First, the issue of creep of the gold gasket resulting from thermal cycling must be mitigated. A small groove in the Inconel wall could serve as a seat for a gold gasket, which may prevent creep. Second, an internal or external spring force must be used to hold the sapphire ball in place, allowing for thermal expansion and providing a consistent force against the gold gasket during cooldown. A simple alteration of the backing nut or the addition of Belleville washers may be sufficient to provide this spring force. The design of a robust HTHP Raman cell is beyond the scope and focus of this research, but it remains an open and significant design challenge.

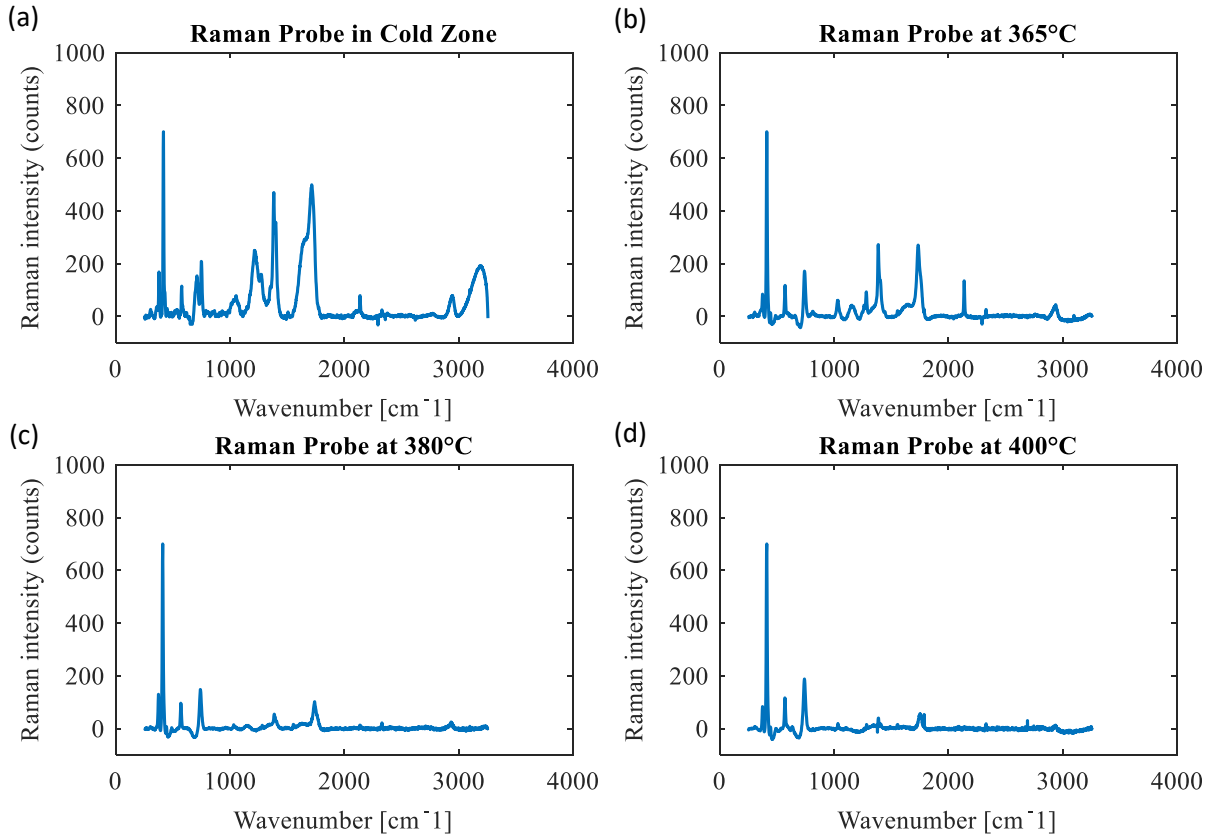

Figure 6: Plots of baseline-subtracted Raman spectra from formic acid decomposition experiments with (a) Raman probe in cold zone, (b) Raman probe in hot zone at 365°C, (c) Raman probe in hot zone at 380°C, and (d) Raman probe in hot zone at 400°C. Significant reduction in signal intensity appears to be due to temperature-dependent optical effects, which significantly complicate quantitative spectroscopy.

As a solution to provide *in situ* product monitoring while avoiding issues with thermal expansion, thermal cycling, and temperature-dependent spectral effects, the Raman cell is placed downstream of the heat exchanger. While this allows the cell to function properly, it eliminates the ability to analyze intermediate reaction products in the HTHP hydrolysis environment.

4.3. Data Collection and Analysis of Raman Spectra

The fiber-optic Raman laser has an excitation wavelength of 785 nm and is operated at 300 mW. A sapphire ball lens focuses the laser 0.6 mm in front of the lens, which protrudes 0.5 mm into the flow. Spectra are collected in the backscatter configuration where the exciting laser and the scattered light enter and exit the measurement volume through the same optical window, and along the same axis. Five replicate spectra, each with a total integration time of 20 s, are collected and averaged for each experimental condition, to ensure an acceptable signal-to-noise ratio.

Water has a significant fluorescent signal which must be subtracted to obtain useful data. This fluorescent signal is approximately linear, with a maximum value at low wavenumbers and a minimum value at high wavenumbers, but linear subtractions leave large signal errors. Various algorithms and methods exist for fluorescent background subtraction, including polynomial fits, wavelet algorithms, manual baseline selections, and others [80-82]. For consistent data analysis, a semi-manual background subtraction algorithm is implemented in MATLAB, which interpolates between fixed points based on the known reaction products [83]. The Raman signal intensity is theoretically zero at wavenumbers where known Raman peaks do not exist. The MATLAB code functions by defining “anchor points” where the Raman signal should be zero and interpolating between these points to form the baseline. This baseline is then directly subtracted from the measured signal. Figure 7 demonstrates the efficacy of the baseline subtraction algorithm.

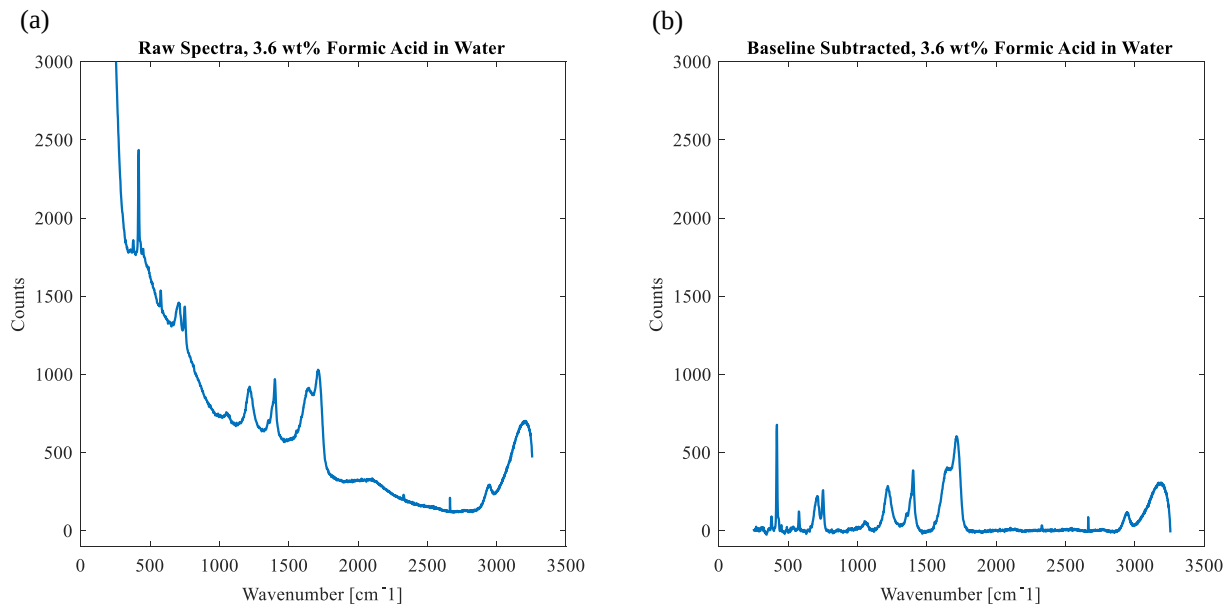

Figure 7: 3.6 wt% formic acid in DI water (a) before fluorescent background subtraction and (b) after baseline subtraction.

Quantitative spectroscopic techniques are used to extract concentration measurements from Raman spectra, using PEAXACT (Aachen, Germany) quantitative spectral analysis software. A molecule's Raman signal scales linearly with molar concentration, thus peak heights and peak areas can be measured to extract molar concentration measurements. In order to measure species concentration from peak height or area, a compound must have a dominant characteristic peak in a spectral "window," where no other spectral constituent exists. For regions in which multiple characteristic peaks of separate compounds are convoluted, direct hard modeling or indirect hard modeling (IHM) can be used to calculate concentrations [84-86]. For both hard modeling techniques, characteristic peaks are modeled as Voight curves, which are superposed with weightings that correspond to concentrations. IHM also corrects for non-linear effects which can arise due to pressure, temperature, hydrogen bonding, and ongoing reactions.

One challenge with quantitative Raman spectroscopy is producing one's own calibration data. While Raman libraries exist for identifying molecular constituents, no calibration data exists

publicly, due to differences between Raman systems. It is especially challenging to generate calibration data for reacting systems where some constituents may be unstable. It is desirable to accurately calibrate Raman spectra of reacting systems with limited spectral information about constituents. Due the hazardous and flammable gases produced during gasification (e.g., CO, H_2) an indirect calibration technique is used for data collected in all experiments.

Beumers et al. [86] proposed a calibration methodology for Raman spectra that relies on reaction stoichiometry; a mixture within a closed control volume has a fixed atomic composition. Molecular species can change due to chemical reactions, but any species must be composed of the atoms that are initially present. The method was demonstrated for a mixture of monoethanolamine, water, and CO_2 in a batch reactor. Likewise, for an open control volume operating at steady-state conditions, the atomic composition entering the control volume must equal the atomic composition exiting the control volume. Thus, atom balances for gasification of a known quantity of any compound must close for a given system.

The molar concentration of each molecular constituent in the optical control volume is proportional to the area of the molecule's Raman spectra. Following the method proposed by Beumers et al. [86] the molar concentration (c_C) of each compound exiting the reactor through the optical control volume can be expressed as

$$c_C = k_C A_C \tag{7}$$

and the total molar flow rate of each compound exiting the reactor is correspondingly

$$\dot{n}_C = k_C A_C \dot{n}_{tot} \tag{8}$$

where $\dot{n}_{tot}$ is the total molar flow rate exiting the reactor, A_C is the area of a given constituent's Raman signal, and k_C is the calibration proportionality constant. The quality of calibration depends on accurately determining k values for each molecule.

An IHM for the effluent constituents is constructed using pure compound spectra of reactants and products. Raw spectral areas are calculated using PEAXACT, which are then entered into MATLAB to determine k_C values with a least squares error minimization of stoichiometric atom balances in the reactor. A more in-depth discussion and validation of this methodology was conducted for the formic acid gasification experiments and is available in [37].

It should be noted that direct calibration was attempted using mixture spectra of known concentrations of CO_2, formic acid, and water. However, this method failed due to the narrow range of molar yields possible for each gaseous species. At low concentrations, non-linear spectral effects become more significant and calibration must be performed within a narrow range. Any error in producing mixture spectra could result in drastic errors in final concentration measurements.

Table 2: Compounds present in effluent streams, with locations of significant Raman peaks.

Compound	Wavenumbers of Significant Raman Peaks (cm^{-1})	Source
Sapphire (Al_2O_3)	379, 418, 751	Direct
Water (H_2O)	1640, 3185	Direct
Formic Acid (HCOOH)	712, 1219, 1400, 1714, 2943	Direct
Isopropyl Alcohol (C_3H_7OH)	816, 945, 1459, 2920, 2982	Direct
Ethanol (C_2H_5OH)	879, 1046, 1085, 1445, 2929, 2981	Direct
Methanol (CH_3OH)	1017, 1469, 2845, 2954	Direct
Acetone (C_3H_6O)	799, 1240, 1427, 1699, 2930	Direct
Acetaldehyde (C_2H_4O)	860, 1098, 1432, 1716, 2928	Direct
Acetic Acid (CH_3COOH)	892	Direct
Formaldehyde (CH_2O)	2917	[87]
Hydrogen (H_2)	355, 587, 814, 1034	Direct
Carbon Dioxide (CO_2)	1272, 1383	Direct
Carbon Monoxide (CO)	2138	Direct
Methane (CH_4)	2915	[87]
Ethylene (C_2H_4)	1343, 1624	[87]
Ethane (C_2H_6)	992, 2898, 2953	[87]
Propene (C_3H_6)	919, 1298, 1649	[87]
Propane (C_3H_8)	869	[87]
Benzene (C_6H_6)	992	[88]

5. Formic Acid Decomposition

The decomposition kinetics of formic acid are studied in a continuous water reactor at temperatures from 300 to 430°C, a pressure of 25 MPa, residence times between 4 and 65 s, and a fixed initial concentration of 3.6 wt%. Formic acid is a common intermediate gasification product with simple decomposition chemistry; analyzing its decomposition is a useful proof-of-concept for *in situ* Raman analysis techniques. From Yu and Savage [77], Zhang et al. [78], and Bjerre and Sorensen [89], the primary decomposition pathway of formic acid in supercritical water is reported as decarboxylation. A minor reaction pathway of dehydration also exists; both are presented and discussed in Section 3.5.

The single-step decomposition of formic acid into gaseous products allows for simple analysis of reaction products with Raman spectroscopy. With five compounds present in the effluent stream, the process of quantitatively converting Raman spectra to chemical decomposition rates is validated. Validation of this process with a simple compound allows for generalization to analyzing the decomposition of more complex model compounds in supercritical water.

An 88% formic acid solution from Fisher Scientific (Hampton, NH) is diluted with DI water to a 30 vol% solution. DI water and the aqueous formic acid are fed to the reactor at a fixed volumetric flow ratio of 9:1, which corresponds to an initial formic acid mass fraction of 3.6 wt%. Gasification resulted in yields of H_2, CO, and CO_2. Monitoring gasification with Raman spectroscopy proved to be an effective *in situ* technique for identifying reaction products and calculating effluent species concentrations.

Table 2 in Section 4.3 lists compounds present in collected Raman spectra and the associated wavenumbers of significant Raman peaks. Peaks may be slightly shifted from reference data due to the operating pressure. Figure 8 shows a representative *in situ* Raman spectrum

collected during the study, clearly showing the decomposition products formed from gasifying formic acid. The significant peaks of corresponding molecular constituents are noted in the plot.

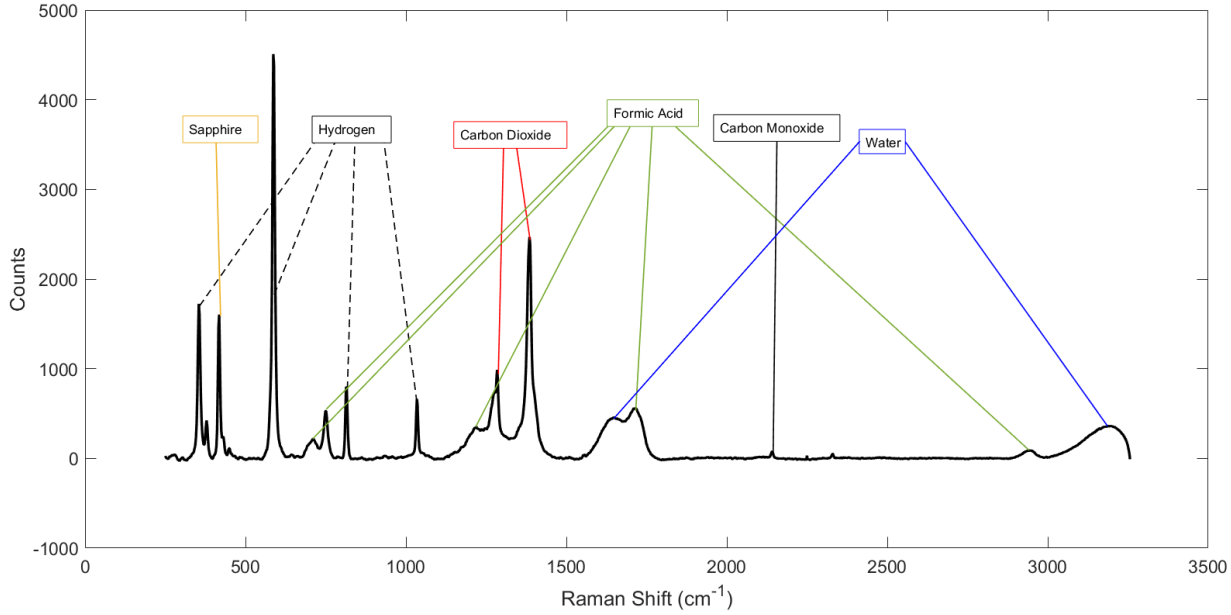

Figure 8: Raman spectra collected *in situ* of formic acid decomposition products. Significant Raman peaks are correlated with corresponding molecular constituents.

5.1. Experimental Results

The full decomposition behavior of formic acid in water at 380°C is shown in Figure 9. The baseline signal of 3.6 wt% formic acid dissolved in DDI water is shown in Figure 9(a) for comparison to the spectra of decomposition products. Some fluctuation of H_2 and CO peaks are witnessed despite steady-state reactor operation, as the two gases are insoluble in subcritical water, and the transition to a two-phase flow forms bubbles in the heat exchanger. Averaging the signal over a long integration time negates signal fluctuations, which result from phase separation. This is verified by the relatively low uncertainty values associated with H_2 and CO measurements, as

seen in Table 3, and Figures 10 and 11. Table 3 presents compound yield percentages by weight after gasification at all tested temperatures and residence times.

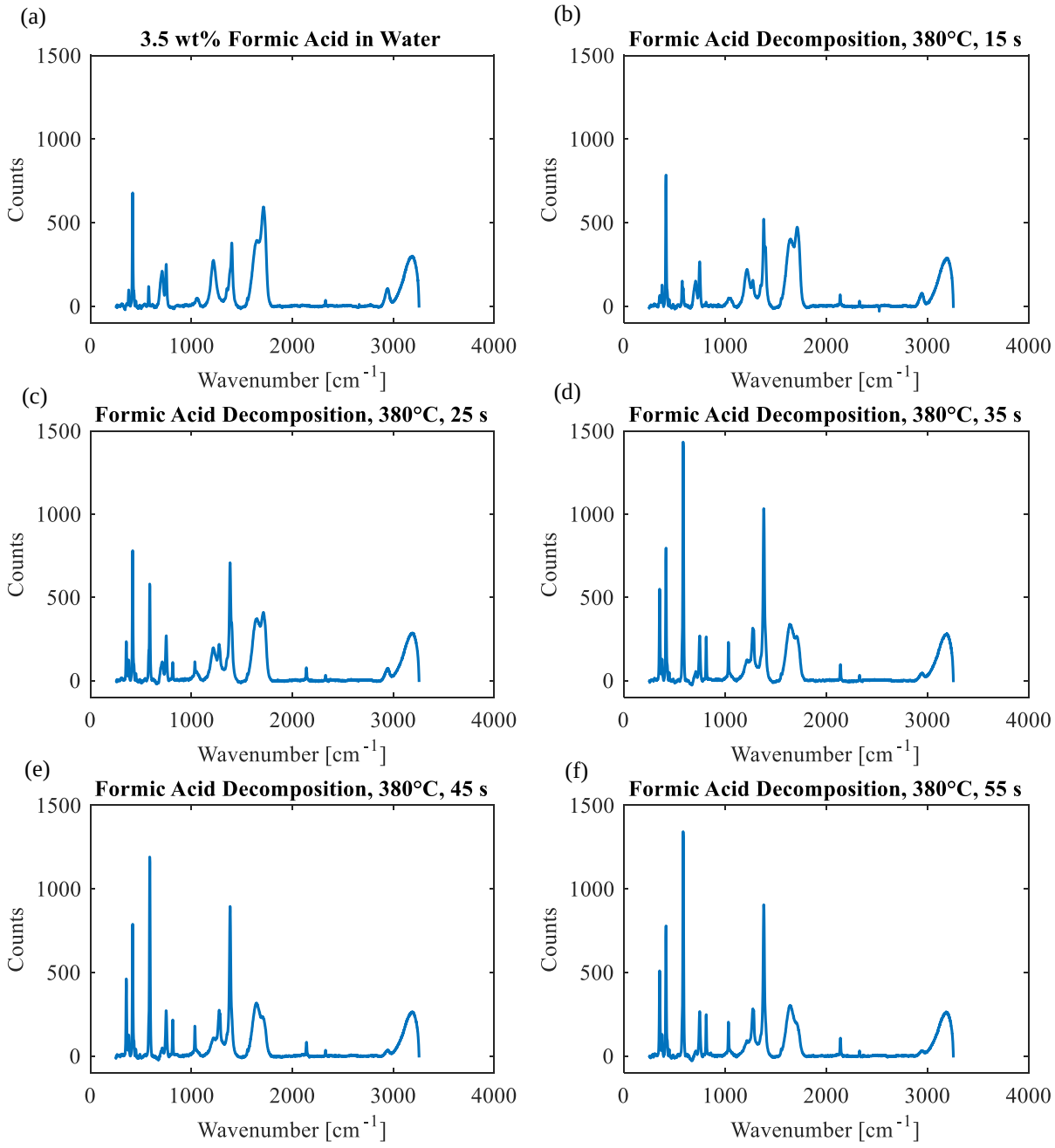

Figure 9: Raman spectra of (a) formic acid and (b) – (f) decomposition products at 380°C and residence times between 15 and 55 s. Spectra show increased yields of H_2 and CO_2 as residence time is increased.

Table 3: Formic acid decomposition yields at tested conditions, with measurement uncertainty to CI of 95%.

Temp. (°C)	Res. Time (s)	Formic Acid Yield (%wt)	H_2 Yield (%wt)	CO Yield (%wt)	CO_2 Yield (%wt)	Total Gas Yield (%wt)	Gasification Efficiency (%)
300	25	2.18±0.014	0.00392±0.0019	0.191±0.016	0.104±0.0064	0.299±0.017	8.30±0.48
300	35	2.24±0.019	0.00403±0.00043	0.313±0.023	0.108±0.0056	0.425±0.026	11.8±0.75
300	45	2.17±0.062	0.00280±0.00048	0.480±0.034	0.166±0.017	0.648±0.037	18.0±1.1
300	55	2.15±0.024	0.00383±0.00057	0.505±0.033	0.157±0.021	0.665±0.037	18.5±1.1
300	65	2.11±0.020	0.00303±0.00019	0.649±0.052	0.253±0.0082	0.905±0.054	25.2±1.5
320	25	2.11±0.016	0.00404±0.00041	0.361±0.0093	0.128±0.0093	0.493±0.019	13.7±0.53
320	30	2.13±0.022	0.00307±0.00072	0.447±0.021	0.179±0.013	0.629±0.029	17.5±0.82
320	40	2.06±0.023	0.00325±0.0011	0.654±0.019	0.272±0.0095	0.929±0.020	25.8±0.58
320	50	1.91±0.097	0.00416±0.0012	0.749±0.025	0.424±0.010	1.18±0.024	32.7±0.69
320	60	1.80±0.026	0.00805±0.0020	0.774±0.064	0.521±0.011	1.30±0.063	36.2±1.8
340	20	1.96±0.019	0.00±0.00014	0.430±0.023	0.232±0.0089	0.662±0.028	18.4±0.79
340	30	1.99±0.027	0.00377±0.00047	0.727±0.021	0.382±0.015	1.11±0.034	30.9±0.96
340	40	1.78±0.030	0.0110±0.0027	0.772±0.050	0.572±0.018	1.35±0.042	37.6±1.2
340	50	1.64±0.014	0.0172±0.0055	0.845±0.084	0.708±0.016	1.57±0.10	43.6±3.0
340	60	1.53±0.035	0.0209±0.0046	0.871±0.089	0.855±0.033	1.75±0.12	48.5±3.3
360	20	1.88±0.033	0.00332±0.00023	0.620±0.039	0.403±0.0065	1.03±0.040	28.5±1.1
360	30	1.75±0.045	0.0115±0.0022	0.712±0.043	0.665±0.030	1.39±0.069	38.5±2.0
360	40	1.53±0.052	0.0190±0.0029	0.780±0.061	0.823±0.027	1.62±0.079	45.1±2.3
360	50	1.33±0.091	0.0254±0.0034	0.803±0.051	0.917±0.032	1.75±0.072	48.5±2.1
360	60	1.26±0.061	0.0375±0.0082	0.824±0.095	1.16±0.068	2.02±0.11	56.2±3.2
380	15	1.81±0.057	0.00476±0.0010	0.474±0.030	0.610±0.040	1.09±0.069	30.2±2.0
380	25	1.66±0.040	0.0257±0.0014	0.538±0.014	1.01±0.029	1.57±0.031	43.6±0.89
380	35	1.28±0.040	0.0696±0.0080	0.656±0.036	1.71±0.19	2.44±0.22	67.7±6.3
380	45	1.13±0.030	0.0612±0.019	0.665±0.11	1.62±0.12	2.35±0.22	65.3±6.3
380	55	0.981±0.062	0.0706±0.0095	0.820±0.090	1.70±0.055	2.59±0.14	71.9±3.9
390	10	1.92±0.098	0.0572±0.015	0.279±0.036	1.57±0.089	1.90±0.14	52.8±3.9
390	15	1.64±0.021	0.0751±0.017	0.433±0.085	1.88±0.055	2.39±0.11	66.3±3.1
390	20	1.23±0.046	0.105±0.0072	0.571±0.035	2.40±0.11	3.08±0.15	85.5±4.3
390	25	0.613±0.062	0.132±0.010	0.462±0.037	2.43±0.12	3.02±0.16	84.0±4.5
390	30	0.590±0.047	0.124±0.013	0.498±0.057	2.79±0.22	3.41±0.27	94.8±7.7
400	5	1.73±0.023	0.0144±0.0027	0.265±0.012	0.817±0.023	1.10±0.033	30.5±0.95
400	7.5	1.49±0.039	0.0344±0.0082	0.353±0.045	1.17±0.15	1.56±0.19	43.3±5.6
400	10	0.706±0.10	0.204±0.024	1.48±0.12	4.11±0.26	5.79±0.40	161±11
400	12.5	0.911±0.045	0.102±0.011	0.610±0.066	2.20±0.14	2.91±0.22	80.8±6.1
400	15	0.622±0.077	0.107±0.020	0.623±0.075	2.48±0.14	3.21±0.21	89.1±6.0
410	5	1.33±0.025	0.0565±0.0097	0.399±0.047	1.45±0.12	1.91±0.17	52.9±4.8
410	7.5	0.925±0.042	0.0990±0.020	0.567±0.074	2.14±0.10	2.81±0.19	78.0±5.4
410	10	0.516±0.096	0.111±0.010	0.575±0.052	2.38±0.11	3.06±0.11	85.0±3.1
410	12.5	0.249±0.10	0.127±0.026	0.698±0.15	2.47±0.22	3.29±0.39	91.5±11
410	15	0.201±0.037	0.132±0.037	0.662±0.21	2.61±0.26	3.40±0.50	94.5±14
420	5	1.15±0.023	0.0747±0.0057	0.504±0.031	1.78±0.079	2.35±0.10	65.4±2.9
420	6.25	0.747±0.041	0.111±0.0099	0.756±0.061	2.20±0.089	3.07±0.15	85.3±4.4
420	7.5	0.712±0.066	0.136±0.018	0.779±0.096	2.63±0.17	3.54±0.27	98.4±7.8
420	8.75	0.508±0.037	0.113±0.0070	0.742±0.046	2.46±0.095	3.32±0.14	92.2±4.0
420	10	0.438±0.054	0.126±0.013	0.684±0.050	2.62±0.070	3.43±0.12	95.2±3.5
430	4	0.979±0.030	0.0935±0.0068	0.678±0.044	1.91±0.090	2.68±0.13	74.4±3.8
430	5	0.736±0.038	0.111±0.014	0.740±0.097	2.24±0.046	3.08±0.15	85.7±4.3
430	6	0.502±0.034	0.113±0.012	0.757±0.061	2.40±0.057	3.27±0.12	90.7±3.6
430	7	0.464±0.046	0.116±0.016	0.782±0.095	2.53±0.053	3.43±0.15	95.3±4.2
430	8	0.456±0.039	0.131±0.014	0.849±0.11	2.57±0.070	3.54±0.17	98.5±4.9

Figure 10 shows subcritical product yields with kinetic rate curve fits. Small error bars on product yields reflect steady-state reactor operation and low measurement uncertainty. At the lowest tested temperatures, the formic acid decomposition does not adhere well to a first-order decomposition curve. However, it is known that formic acid exists as an intermediate of the WGS reaction at temperatures above 240°C [36]. Thus, the reformation of formic acid from CO is likely, and the reverse dehydration reaction may be responsible for the observed formic acid yields at 300°C and 320°C.

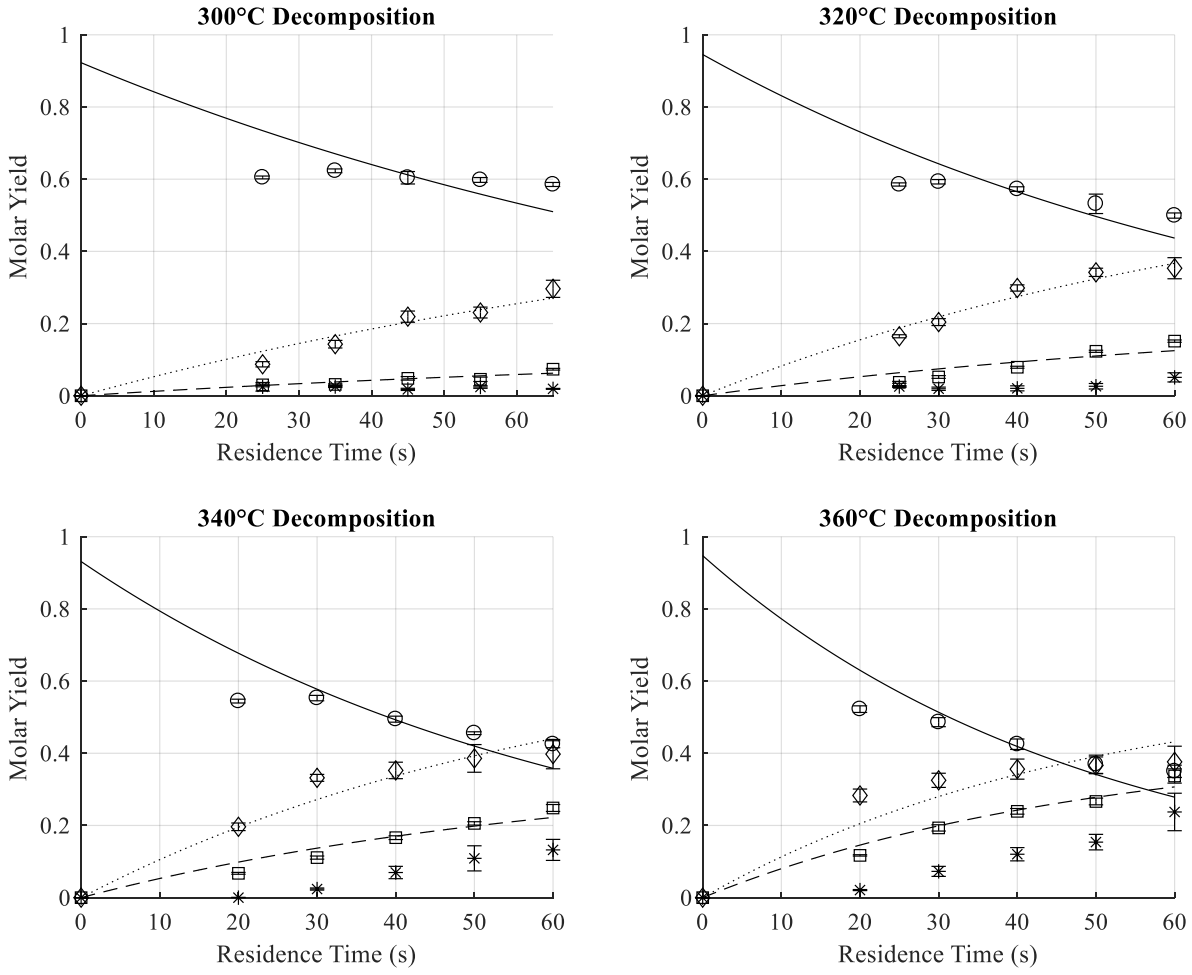

Figure 10: Subcritical formic acid decomposition and gas production profiles with corresponding curve fits used to determine global and pathway kinetic rates. Error bars represent 95% confidence interval.
○ Formic Acid, * H_2, ◊ CO, □ CO_2, – Global Decomposition, -- Decarboxylation, ··· Dehydration

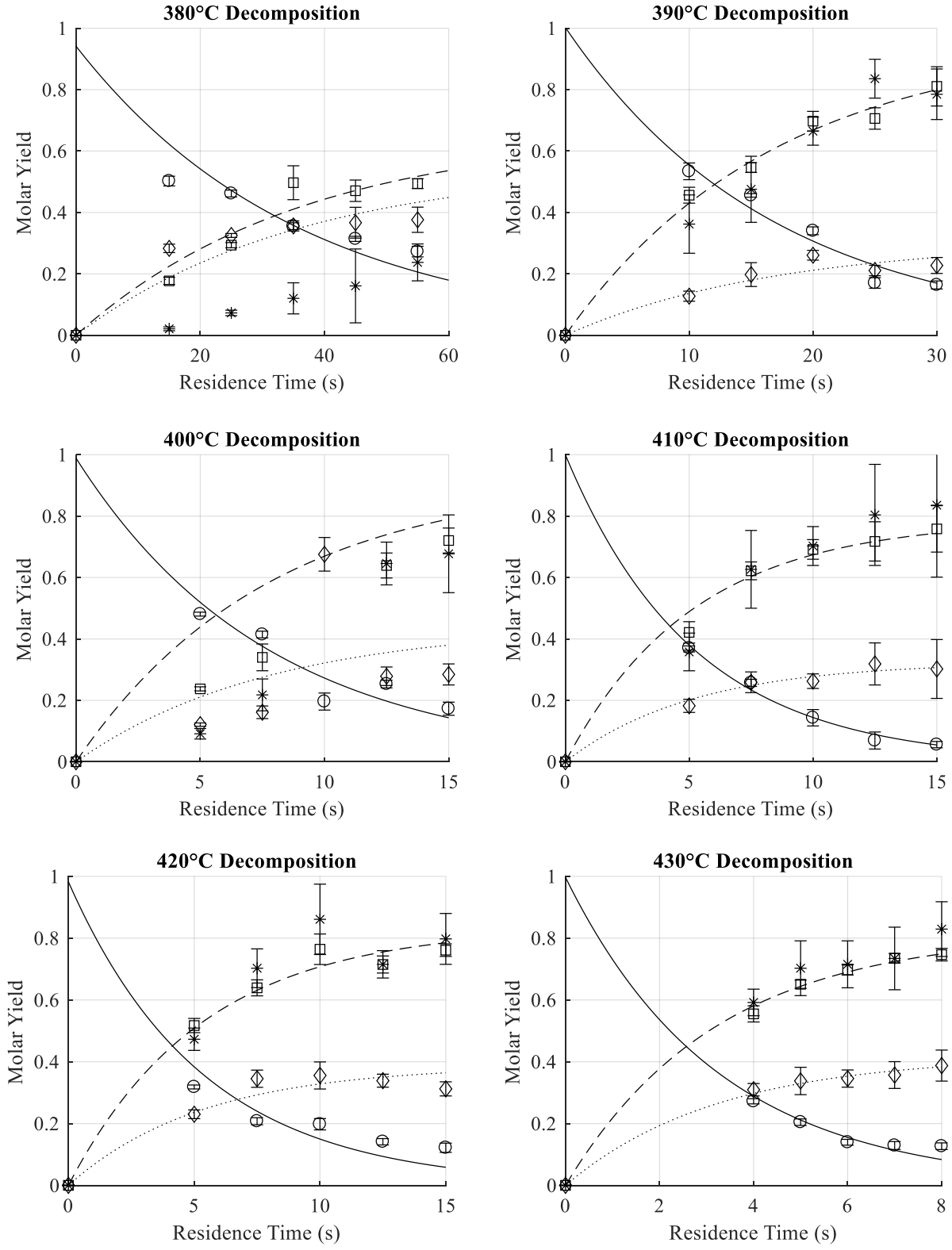

Figure 11: Supercritical formic acid decomposition and gas production profiles with corresponding curve fits used to determine global and pathway kinetic rates. Error bars represent 95% confidence interval.
○ Formic Acid, * H_2, ◊ CO, □ CO_2, – Global Decomposition, -- Decarboxylation, ··· Dehydration

First-order decomposition of formic acid, where k_g represents the global decomposition rate, is expressed with:

$$\frac{d[HCOOH]}{dt} = -k_g[HCOOH] \tag{9}$$

The solution to this first-order differential equation yields the following time-dependent decay equation, where the initial molar concentration of formic acid is normalized to 1 mol. Analyzing the yield data collected at each temperature, first-order global decomposition kinetic rates are calculated using the MATLAB curve-fit toolbox by fitting an exponential decay curve to the collected data.

$$[HCOOH] = e^{-k_g t} \tag{10}$$

Similarly, the first-order formation expressions for H_2, CO_2, and CO are

$$\frac{d[H_2]}{dt} = k_1[HCOOH] \tag{11}$$

$$\frac{d[CO_2]}{dt} = k_1[HCOOH] \tag{12}$$

$$\frac{d[CO]}{dt} = k_2[HCOOH] \tag{13}$$

with k_1 and k_2 representing the reaction rates along the decarboxylation and dehydration pathways respectively. Substituting the time-dependent formic acid expression in Equation 10 yields the following first-order differential equations for Equations 11 through 13:

$$\frac{d[H_2]}{dt} = k_1 e^{-k_g t} \tag{14}$$

$$\frac{d[CO_2]}{dt} = k_1 e^{-k_g t} \tag{15}$$

$$\frac{d[CO]}{dt} = k_2 e^{-k_g t} \tag{16}$$

Integrating this expression with respect to time yields time-dependent formation expressions for H_2, CO_2, and CO.

$$[H_2] = \frac{k_1}{k_g}(1 - e^{-k_g t}) \quad (17)$$

$$[CO_2] = \frac{k_1}{k_g}(1 - e^{-k_g t}) \quad (18)$$

$$[CO] = \frac{k_2}{k_g}(1 - e^{-k_g t}) \quad (19)$$

with the constant resulting from the initial molar concentration of each product gas being zero. A least-square curve fit between product yields and Equations 18 and 19 allows for the calculation of k_1 and k_2, using the k_g values that are previously determined for each temperature. Only data for CO_2 yield is used to calculate k_1, as H_2 yields are observed to be more temporally variable due to bubble formation during effluent quenching. From observation, H_2 is difficult to detect at low concentrations, hence molar yields of H_2 are seemingly lower than molar yields of CO_2 when decarboxylation is less prevalent. CO_2 exists as a liquid at operating pressures; thus, the CO_2 Raman signal is more reliable for calculating the decarboxylation rate. The calculated kinetic parameters are presented in Table 4, and plots of the corresponding curve fits are presented alongside product yield data in Figures 10 and 11.

Plotting $\ln(k_g)$ vs. T^{-1} suggests that formic acid decomposition follows a noticeably different trend in subcritical vs. supercritical water, as seen in Figure 12. Because kinetic rates increase more rapidly above the critical point, separate Arrhenius parameters were proposed for subcritical decomposition and supercritical decomposition. Table 5 presents Arrhenius parameters determined by performing a least-squares curve fit for the data collected above and below the critical point. Figure 12 shows the calculated kinetic rates at each tested temperature, compared to data previously reported by Yu and Savage [77], along with curve fits yielding the reported Arrhenius parameters.

Table 4: First-order global decomposition rates and individual pathway rates of formic acid in subcritical and supercritical water.

Temperature (°C)	Pressure (MPa)	k_g (s^{-1})	k_1 (s^{-1})	k_2 (s^{-1})
300	25	0.00913±0.0067	0.00128±0.00022	0.00552±0.00072
320	25	0.0129±0.0062	0.00299±0.00077	0.00879±0.00069
340	25	0.0159±0.0081	0.00575±0.00085	0.0114±0.0013
360	25	0.0204±0.0078	0.00812±0.00060	0.0125±0.0021
380	25	0.0276±0.011	0.0149±0.0021	0.0153±0.0029
390	25	0.0592±0.011	0.0370±0.0049	0.0116±0.0028
400	25	0.129±0.033	0.0861±0.042	0.0411±0.028
410	25	0.194±0.015	0.153±0.0089	0.0629±0.0043
420	25	0.188±0.054	0.157±0.0088	0.0728±0.0094
430	25	0.310±0.037	0.191±0.0084	0.0975±0.0072

Table 5: Rate parameters for formic acid decomposition in subcritical and supercritical water.

Reaction	Pre-Exponential Factor log A (log s^{-1})	Activation Energy E_A (kcal/mol)
Subcritical Decomposition	1.6 ± 0.20	9.5 ± 0.55
Supercritical Decomposition	12.56 ± 1.96	41.90 ± 6.08
Subcritical Decarboxylation	5.67 ± 0.88	22.36 ± 2.43
Supercritical Decarboxylation	13.83 ± 2.59	46.33 ± 8.02
Subcritical Dehydration	1.52 ± 0.70	9.82 ± 1.92
Supercritical Dehydration	11.38 ± 2.49	39.65 ± 7.72

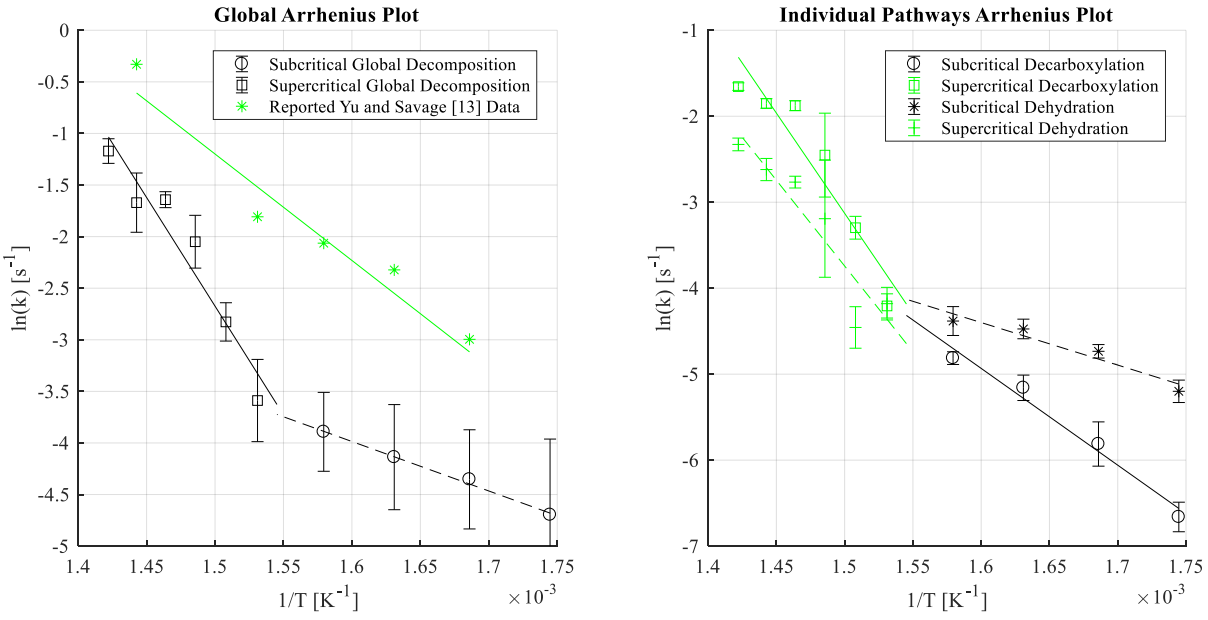

Figure 12: Arrhenius plots of global formic acid decomposition and decomposition along competing decarboxylation and dehydration reaction pathways.

5.2. In Situ Raman Spectroscopy

Raman spectroscopy allows for accurate *in situ* monitoring of liquid and gaseous products in the effluent stream. Because Raman spectra can be collected during reactor operation, all necessary experimental data are collected quickly – ten experimental conditions can be tested in a single day. This shows great promise for expediting gasification studies of more complex model compounds.

One challenge with collecting *in situ* Raman spectra comes from gas separation in the effluent stream. Initially, a Graham (Batavia, NY) Heliflow heat exchanger was used in which the inlet stream flows upward, and the outlet stream flows downward, trapping H_2 and CO. Raman spectra collected with short integration times confirmed that H_2 and CO bubbles were forming within the Graham heat exchanger and exiting at an unsteady frequency. To resolve this issue, a vertically oriented custom heat exchanger was installed that allows insoluble gases to escape and pass through the Raman cell without encountering any locations where bubbles could be trapped. A comparison of data collected with each heat exchanger confirmed that trapped bubbles of H_2 and CO were reforming formic acid within the Graham heat exchanger via the reverse dehydration pathway, as yields of formic acid were much lower with the custom heat exchanger. This is consistent with the accepted knowledge that formic acid is an intermediate of the WGS reaction at temperatures above 240°C [36]. The custom vertical heat exchanger allows for quantitative measurements of gas in the effluent stream, and Raman spectroscopy proves to be an effective *in situ* technique for monitoring gasification products and calculating effluent species concentrations. For future studies of SCWG in a continuous reactor, it is recommended to consider gas separation and flow behavior during quenching.

5.3. Water-Gas Shift Reaction

The literature clearly demonstrates the role of the WGS reaction to convert CO and H_2O into CO_2 and H_2 in supercritical water [1, 77]. Numerous studies have acknowledged that the WGS reaction is significant to the final hydrogen gas yield during SCWG of organic compounds, especially considering that the WGS reaction is catalyzed by nickel. However, formic acid exists as an intermediate of the WGS at temperatures above 240°C [36], thus there is no direct reaction that converts CO and H_2O to CO_2 and H_2 in supercritical water without the reformation of formic acid. At these conditions, the decarboxylation pathway is thought to be irreversible, while the backward dehydration pathway is possible and thermodynamically favored at higher concentrations of CO and lower temperatures. This explains the formic acid yields at 300°C and 320°C, which appear to be nearly constant over the range of tested residence times. Unfortunately, it was not possible to calculate the back reaction rate of the dehydration pathway.

Researchers have investigated the WGS reaction under similar temperatures and pressures, which could lend insight towards the rate of formation of formic acid from CO under the studied conditions [90-93]. Rice et al. [90] studied WGS reaction kinetics in a non-catalytic environment at temperatures from 410 to 520°C and pressures from 2 to 60 MPa, and noted a significant change in reaction rate with changing pressure at 450°C. This was attributed to a density-dependent reaction, with the formation of formic acid from CO being the limiting reaction step. Araki et al. [93] studied the WGS reaction at temperatures from 380 to 450°C and pressures from 20 to 35 MPa. A water density dependence was reported on the order of 1.5±0.1; however, reported density dependence does not agree well with previous studies under similar conditions. Overall, water density is thought to be significant to the conversion of CO to CO_2 through formic acid in

supercritical water, but the exact dependence is not known. Various kinetic rates quantifying the production of formic acid from CO in supercritical water are proposed in [90-93].

5.4. Reaction Mechanisms

Fully characterizing the reaction mechanisms which facilitate formic acid decomposition in supercritical water is challenging without *in situ* monitoring within the hot zone of the reactor. *In situ* spectroscopy in the HTHP zone of the reactor would allow for the identification of ions such as $HCOO^-$, or free-radicals such as COOH or OH. Relative concentrations of these ions or free-radicals could more definitively identify reaction mechanisms. This would be scientifically advantageous but is technically challenging to accomplish, as mentioned above [12, 17, 20, 40]. As such, it is only possible to speculate about reaction mechanisms based on quantum chemical simulations and experimental results.

Interesting discrepancies between Yu and Savage [77] and this study show that for the present work (i) the molar yields of CO are consistently higher, and (ii) yields of CO are higher than yields of CO_2 or H_2 at low temperatures. The discrepancies can plausibly be explained by a difference in the catalytic wall effect between the two studies. Yu and Savage report inner reactor diameters of 1.40 mm and 1.08 mm, while the reactor used for this study has an inner diameter of 3.05 mm. The S/V ratio of the reactor used for this study is 13.1 cm^{-1}, while the S/V ratios of the reactors used in [77] are 28.6 cm^{-1} and 37.0 cm^{-1}. Multiple studies on glucose gasification have shown that reduced reactor diameters contribute to faster reaction kinetics, and higher yields of H_2 [12, 50]. The WGS reaction is significantly catalyzed by a nickel surface; likewise, the higher reactor S/V ratio in [77] is expected to favor CO_2 production through enhanced decarboxylation.

An argument for a surface-catalyzed decarboxylation pathway can be made by closely examining the two plots presented in Figure 12. The decarboxylation trendline looks remarkably similar to the data and trendline for temperatures tested in [77]. In fact, the Arrhenius parameters are close, with the Arrhenius parameters for subcritical decarboxylation determined as log A (s^{-1}) = 5.67 ± 0.88 and E_A = 22.36 ± 2.43 kcal/mol, and Yu and Savage reporting global parameters as log A (s^{-1}) = 6.2 and E_A = 20.5 kcal/mol. Considering Yu and Savage mostly tested subcritical temperatures, and considering data at 380°C seems to follow the subcritical trendline, it is reasonable that these parameters would closely align. A more significant catalytic effect could hypothetically lower the activation energy for this pathway and speed the reaction rate, causing decarboxylation to manifest as the dominant pathway.

Although both pathways can proceed through molecular elimination mechanisms, the significant increase in reaction rates across the critical point, as seen in Figure 12, and the discrepancy in rates between different reactors suggests that a free-radical mechanism is significant to hydrothermal formic acid decomposition in the presence of a catalytic surface. Wei and Iglesia [94] studied the catalytic effect of nickel on the decomposition of CH_4 in the presence of CO_2 and H_2O and proposed that the catalyzed reaction proceeds through the adsorption of C and H atoms from CH_4 on the nickel surface. These adsorbed species increase the reactivity of the surface and increase the radical concentration in the bulk flow. The adsorption of a single H onto the nickel surface from a formic acid molecule would form a COOH radical in the bulk flow, which could decompose into CO_2 and H, or CO and OH. The formed H or OH radicals would abstract H from other formic acid molecules promoting a chain-branching reaction. Figure 13 demonstrates the procession of this reaction mechanism. The decomposition of COOH into CO_2 and H is thought

to be more likely [77], which would support the observation of a favored decarboxylation reaction at conditions supporting free-radical reactions (e.g., higher S/V ratio, lower density).

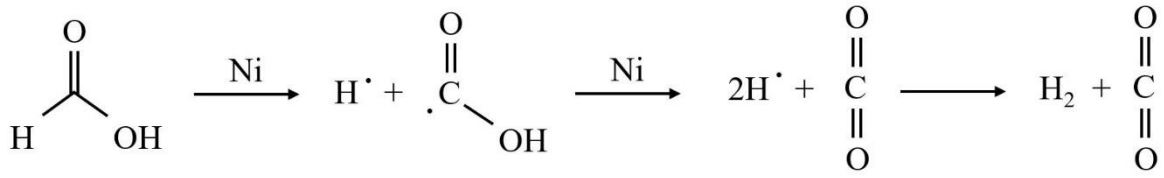

Figure 13: Proposed free-radical mechanism, with hydrogen abstraction (C-H and O-H bond scission) facilitated by catalytic surface and/or other free-radicals in the bulk flow.

6. Methanol Gasification

Several previous studies have investigated methanol decomposition in SCW. Boukis et al. [62] reformed methanol in an Inconel 625 continuous, tubular SCWR at 400 to 600 °C, residence times from 3 to 100 s, and initial methanol loadings from 5 to 64 wt%. H_2, CO, CO_2, and trace amount of CH_4 were detected in the gaseous product. Bennekom et al. [59] gasified methanol in a continuous reactor at temperatures between 450 and 650 °C for residence times between 6 and 173 s. Yields of H_2, CO, and CO_2 were observed. Trace CH_4 yields were reported. Analysis of liquid products revealed trace yields of formaldehyde and formic acid. It was hypothesized that both existed as short-lived reaction intermediates, which is consistent with previous research demonstrating formic acid as an intermediate of the WGS reaction [36, 37].

DiLeo and Savage [21] investigated the role of nickel as a catalyst for methanol gasification in SCW. The presence of a nickel wire in a quartz batch reactor increased conversion from 20% after 2 h to 90% after 5 min at 550 °C. It should be noted that nickel catalysis in a continuous reactor is more significant, as the catalytic effect in the batch setup is limited by the diffusion rate of methanol molecules, while turbulent flow in a continuous reactor can increase interactions with the catalytic wall surface. H_2, CO, and CO_2 were the only products consistently detected in the gaseous phase.

Chakinala et al. [95] proposed that methanol can decompose to gaseous products in SCW primarily through C-H bond scission to a hydroxymethyl radical (CH_2OH) or O-H bond scission to a methoxy radical (CH_3O) followed by loss of an additional H to reach formaldehyde (CH_2O). Formaldehyde is proposed to decompose to CO and H_2 or to reach formic acid (HCOOH) via oxidation with an OH radical. A minor pathway to methane via the formation of a methyl (CH_3) radical by C-O bond scission is also proposed.

In this investigation methanol is continuously fed to the SCWG reactor at an overall volumetric loading of 10 vol%, corresponding to an initial mass fraction of 8.09 wt%. Temperatures were tested from 500 to 560 °C, with pressure fixed at 25 MPa and residence times ranging from 3 to 8 s. Methanol was used as received with no further manipulation or purification. Data are collected, as described in Section 4.3.

SCWG of methanol primarily yields H_2 and CO, with secondary yields of CO_2 and trace formaldehyde production, as shown in Figure 14. These profiles illustrate the sequential nature of product formation; H_2 is detectable at 4 s, followed by CO at 5 s, and CO_2 at 7 s. Formaldehyde is confirmed as a short-lived reaction intermediate; however, no yields of formic acid or methane are detected. We propose the global reaction network shown in Figure 15, with methanol dehydrogenating to formaldehyde, followed by decomposition to CO and H_2.

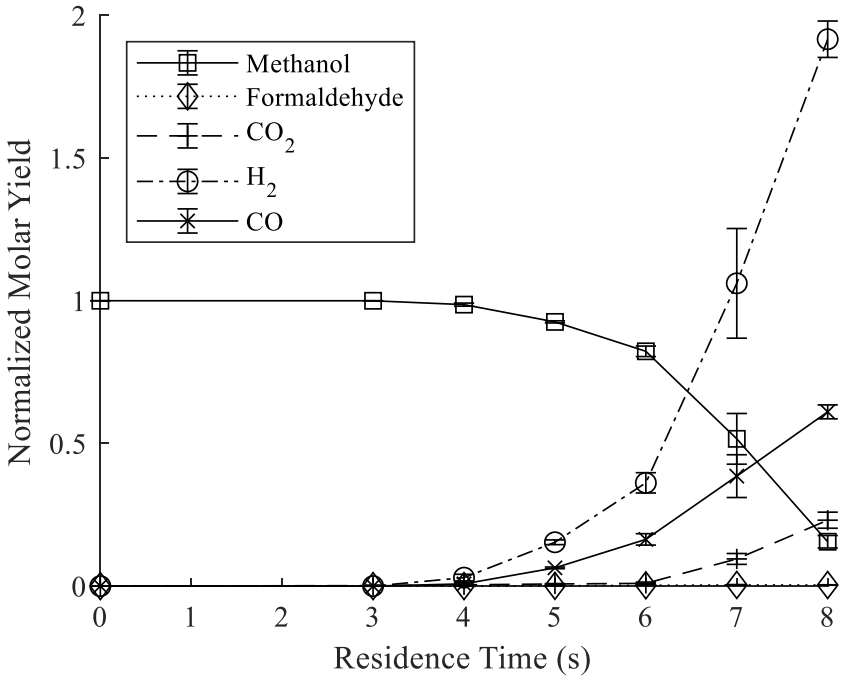

Figure 14: Formation and decomposition of reaction products during SCWG of methanol at 560 °C.

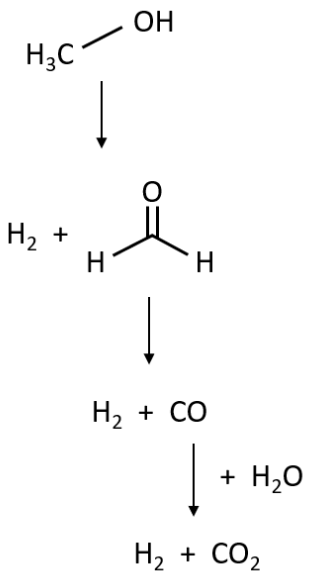

Figure 15: Methanol decomposition network in supercritical water.

Our results indicate that the reaction mechanisms hypothesized by Chakinala et al. [95] to generate formic acid (formaldehyde oxidation) or methane (methyl radical generation) are unlikely to be active during SCWG. Trace methane yields have been reported [59, 62], but it is more likely

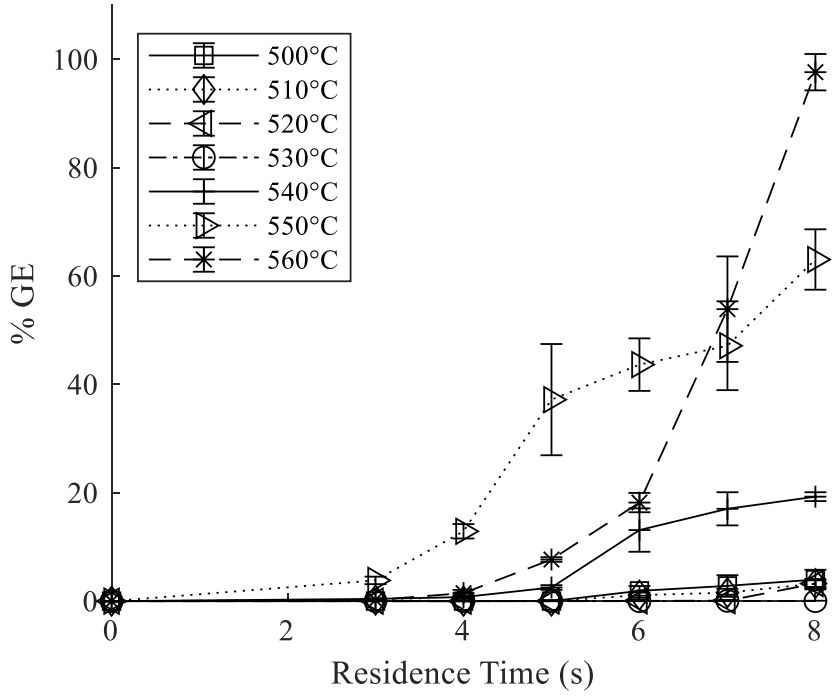

Figure 16: Gasification efficiency of methanol at all tested conditions.

that secondary methanation reactions are responsible for this observation. The time scales and temperatures necessary for methanol conversion in these experiments are similar to those reported for continuous SCWG of methanol by Boukis et al. [62] and Bennekom et al. [59]. Conversion rates at similar conditions were much slower in quartz batch reactors as reported by DiLeo and Savage [21], highlighting the significance of the catalytic reactor walls.

The WGS reaction is responsible for the observed maximum CO_2 yield of 0.23 mol-CO_2/mol-MeOH, but low CO_2 yields indicate that the WGS reaction does not have sufficient residence time to reach completion. The full conversion of methanol along the network in Figure 15 would result in a maximum of 1 mol-CO_2/mol-MeOH and 3 mol-H_2/mol-MeOH. Complete conversion of CO would increase H_2 yields past the observed maximum of 1.92 mol-H_2/mol-MeOH. Gasification efficiency is plotted against residence time for all tested temperatures in

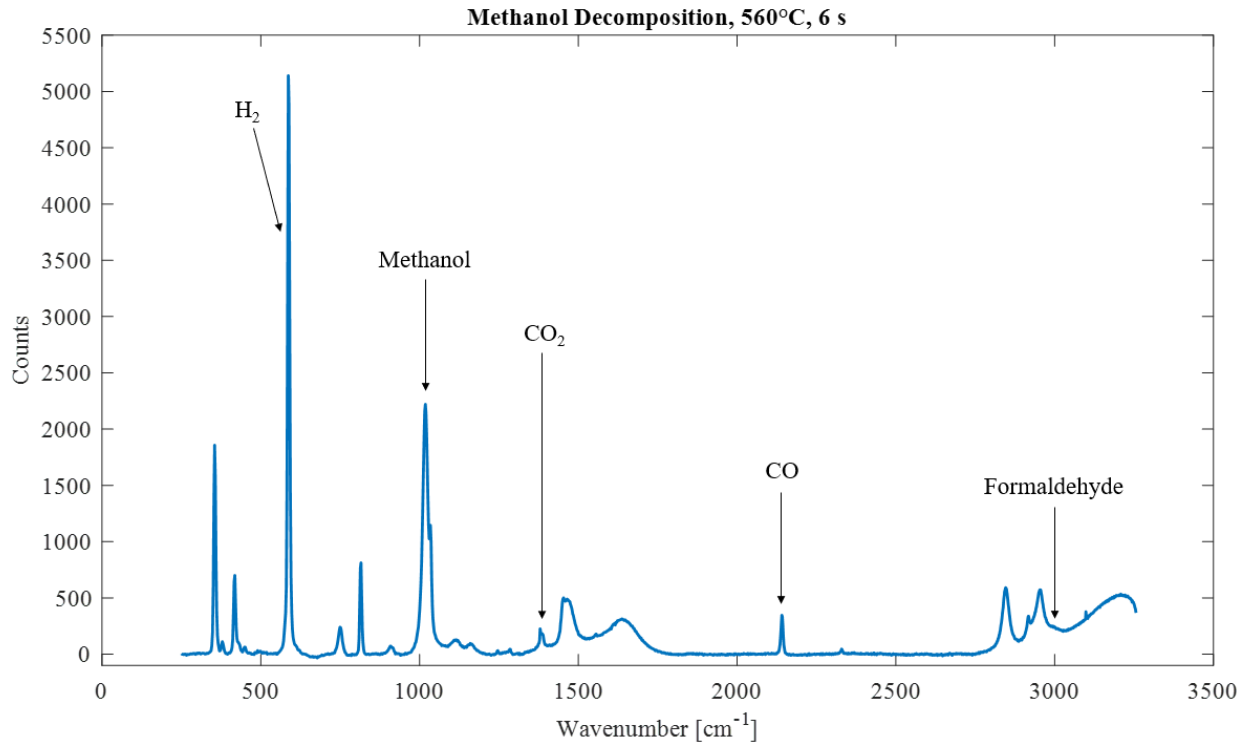

Figure 17: Representative Raman spectrum of methanol decomposition products after gasification for 6 s at 560 °C, with significant peaks identified.

Figure 16. GE approaches values above 100% at 560 °C, due to the conversion of liquid H_2O to gaseous H_2 via the WGS. No other methanol decomposition products are detected over the tested temperature and residence time range, and reaction profiles at all temperatures follow similar trends. Plots of compound formation and decomposition at all tested temperatures are available in Figure 18, and a representative Raman spectrum of methanol gasification products is shown in Figure 17.

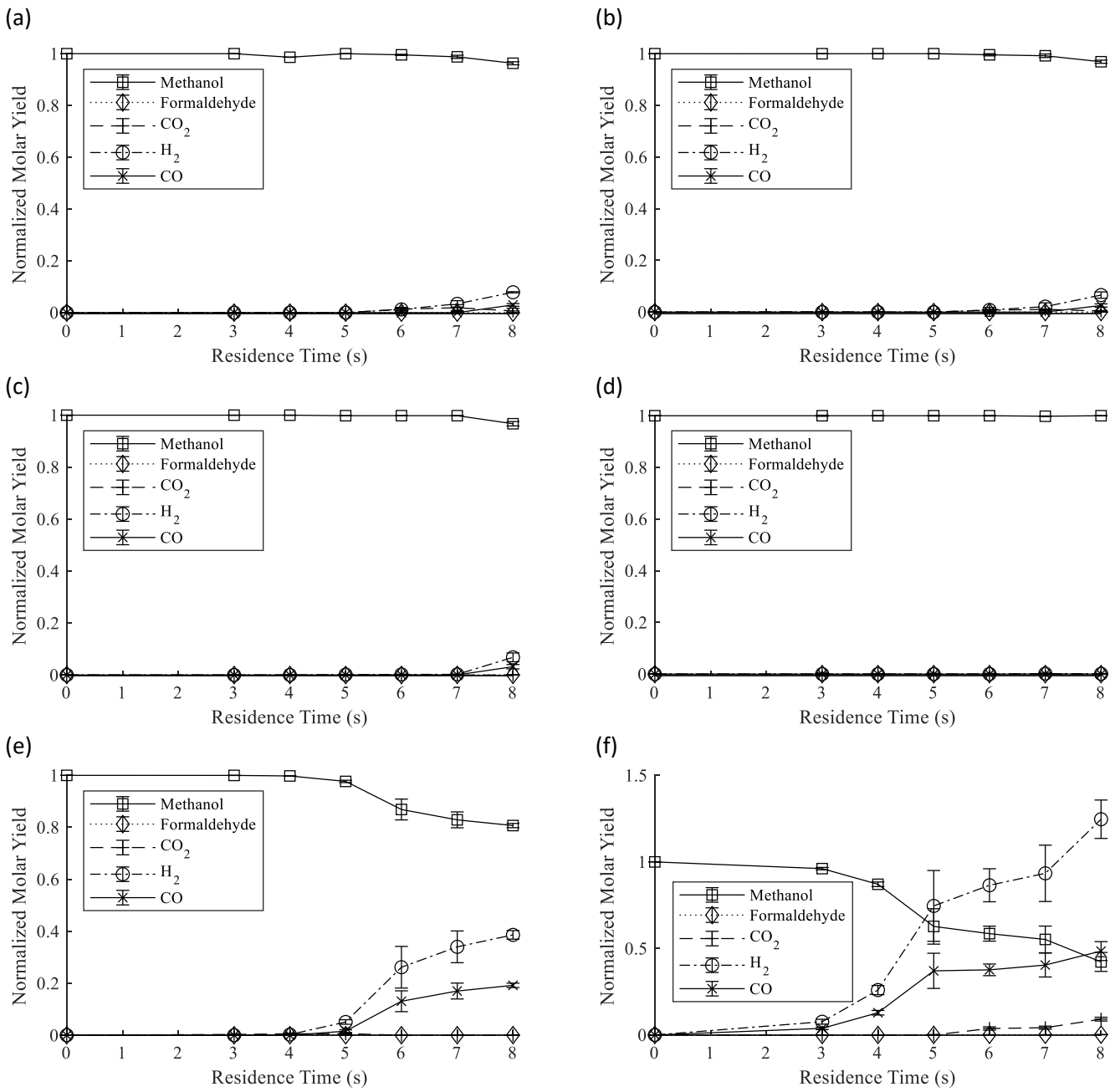

Figure 18: Formation and decomposition of reaction products during methanol gasification in SCW at (a) 500 °C, (b) 510 °C, (c) 520 °C, (d) 530 °C, (e) 540 °C, and (f) 550 °C.

7. Ethanol Gasification

Schanzenbächer et al. [96] gasified ethanol in a continuous SCWR at temperatures from 433 to 494 °C, constant pressure of 24.6 MPa, and residence times from 2 to 12 s. Maximum conversion was reported as 16.5%; only acetaldehyde (C_2H_5O) was identified as a reaction product.

Arita et al. [97] studied non-catalytic reaction pathways of ethanol in a batch SCWR. Temperatures from 450 to 500 °C were maintained for 10 to 60 minutes, with primary reaction products identified as H_2, CH_4, and CO_2, and minor yields of CO, acetaldehyde, ethylene, and ethane. Two competing reaction pathways were proposed: (i) dehydrogenation of ethanol to acetaldehyde followed by acetaldehyde decomposition to CO and CH_4, or (ii) dehydration of ethanol to ethylene followed by hydrogenation of ethylene to ethane. Global reactions for the two pathways are as follows:

$$C_2H_5OH \rightarrow C_2H_4O + H_2 \quad (20)$$

$$C_2H_4O \rightarrow CH_4 + CO \quad (21)$$

$$CO + H_2O \rightarrow CO_2 + H_2 \quad (22)$$

$$C_2H_5OH \rightarrow C_2H_4 + H_2O \quad (23)$$

$$C_2H_4 + H_2 \rightarrow C_2H_6 \quad (24)$$

Chakinala et al. [95] hypothesized that ethanol decomposes via O-H or C-H bond scission to produce acetaldehyde. At various points in the proposed reaction network, the C-C bond can be broken, forming a methyl radical, which ultimately forms CH_4. The proposed network is based on observed yields of H_2, CO, CO_2, CH_4, and ethane.

Ethanol is continuously fed to the SCWG reactor at an overall volumetric loading of 10 vol%, corresponding to an initial mass fraction of 8.06 wt%. Temperatures were tested from 500 to 560 °C, with pressure fixed at 25 MPa and residence times ranging from 3 to 8 s. Ethanol was used as received with no further manipulation or purification. Data are collected as described in Section 4.3.

Acetaldehyde and ethylene are the first observable products during the SCWG of ethanol, as shown at 3 s in Figure 20. This is followed by a significant increase in H_2, CO, and CH_4 yields at 5 s, as seen in Figure 19. Acetaldehyde yields continue to increase to a maximum of 0.12 mol-C_2H_4O/mol-EtOH at 6 s, followed by a similarly paced decrease to 0.005 mol-C_2H_4O/mol-EtOH, confirming its role as a short-lived intermediate. Once sufficient H_2 is generated for ethylene hydrogenation, ethane emerges as a detectable product at 6 s. Finally, a CO_2 yield of 0.04 mol-CO_2/mol-EtOH is measured at 8 s, again resulting from the WGS reaction. Figure 19 demonstrates

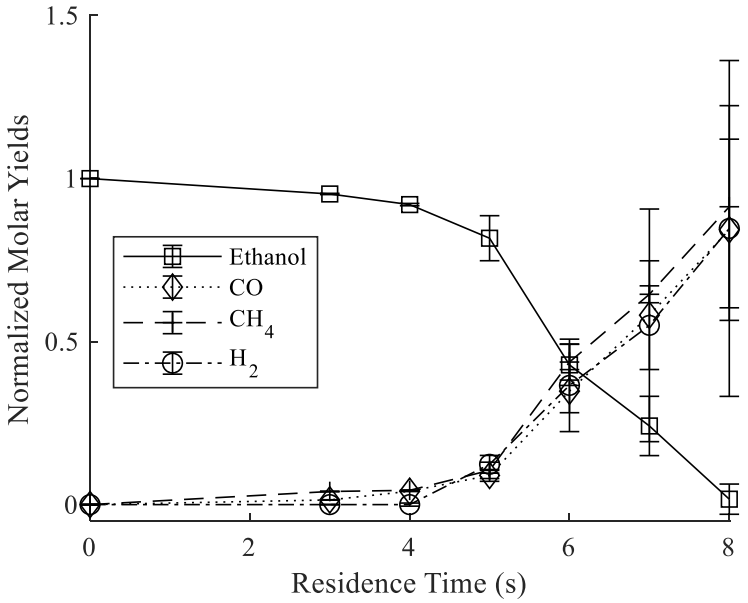

Figure 19: Formation and decomposition of major reaction products during SCWG of ethanol at 560 °C.

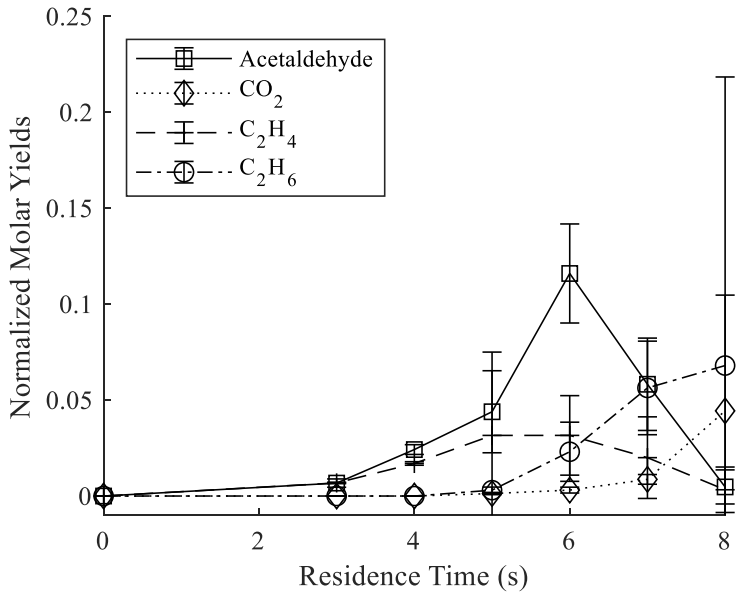

Figure 20: Formation and decomposition of minor reaction products during SCWG of ethanol at 560 °C.

that H_2, CO, and CH_4 are produced in nearly equimolar quantities, reaching maximum respective yields of 0.85 mol-H_2/mol-EtOH, 0.84 mol-CO/mol-EtOH and 0.91 mol-CH_4/mol-EtOH. This supports the hypothesis that acetaldehyde decomposition is responsible for the formation of CO and CH_4, with molar CO yields slightly lower due to consumption via the WGS. The trends

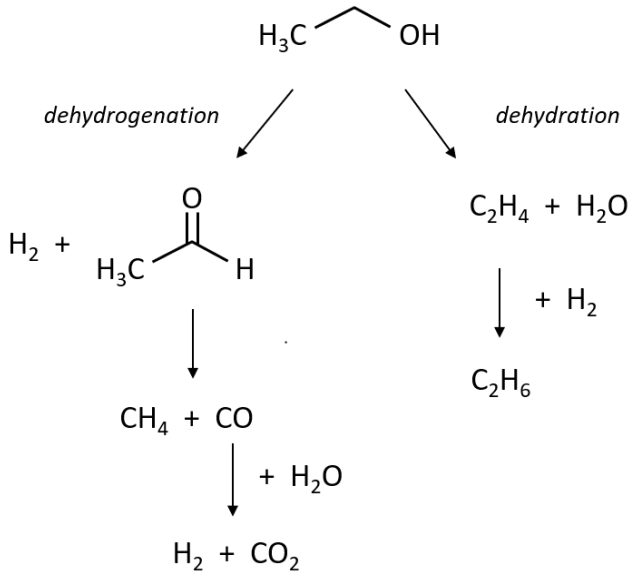

Figure 21: Ethanol decomposition network in supercritical water.

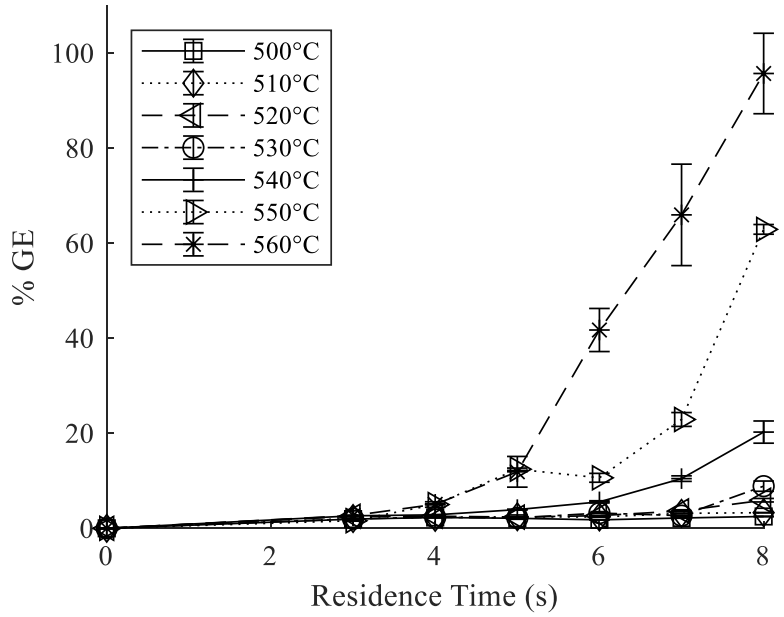

Figure 22: Gasification efficiency of ethanol at all tested conditions.

described here are also observed during SCWG of ethanol at other tested temperatures; these formation and decomposition profiles are available in Figures 24 and 25.

Interpreting the observed product yields, ethanol decomposition follows the reaction pathways illustrated in Figure 6, confirming the global reactions proposed by Arita et al. [97]. However, the time scale for conversion at similar temperatures is orders of magnitude quicker during continuous gasification, again attributable to the catalytic wall effect. Two competing reaction pathways are active, the primary being dehydrogenation to acetaldehyde, with a secondary pathway of dehydration to ethylene. Acetaldehyde is rapidly converted to CO and CH_4, while ethylene can hydrogenate to ethane if suitable H_2 is present. The production of ethane through the reaction of two methyl radicals does not appear to be an active pathway, considering that ethane is only produced subsequent to ethylene production. This also appears to indicate that ethane dehydrogenation to ethylene is a negligible reaction under these conditions. Gasification efficiency

is plotted against residence time for all tested temperatures in Figure 22. A representative Raman spectrum showing reaction products is available in Figure 23.

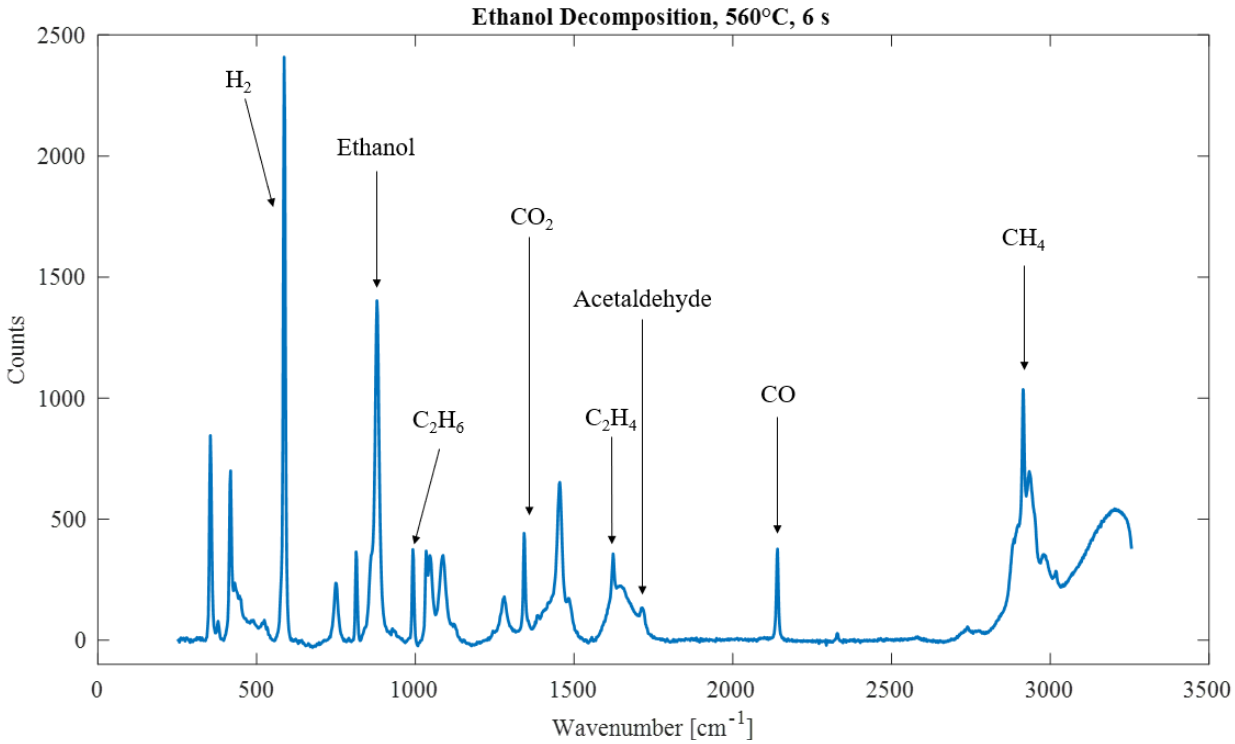

Figure 23: Representative Raman spectrum of ethanol decomposition products after gasification for 6 s at 560 °C, with significant peaks identified.

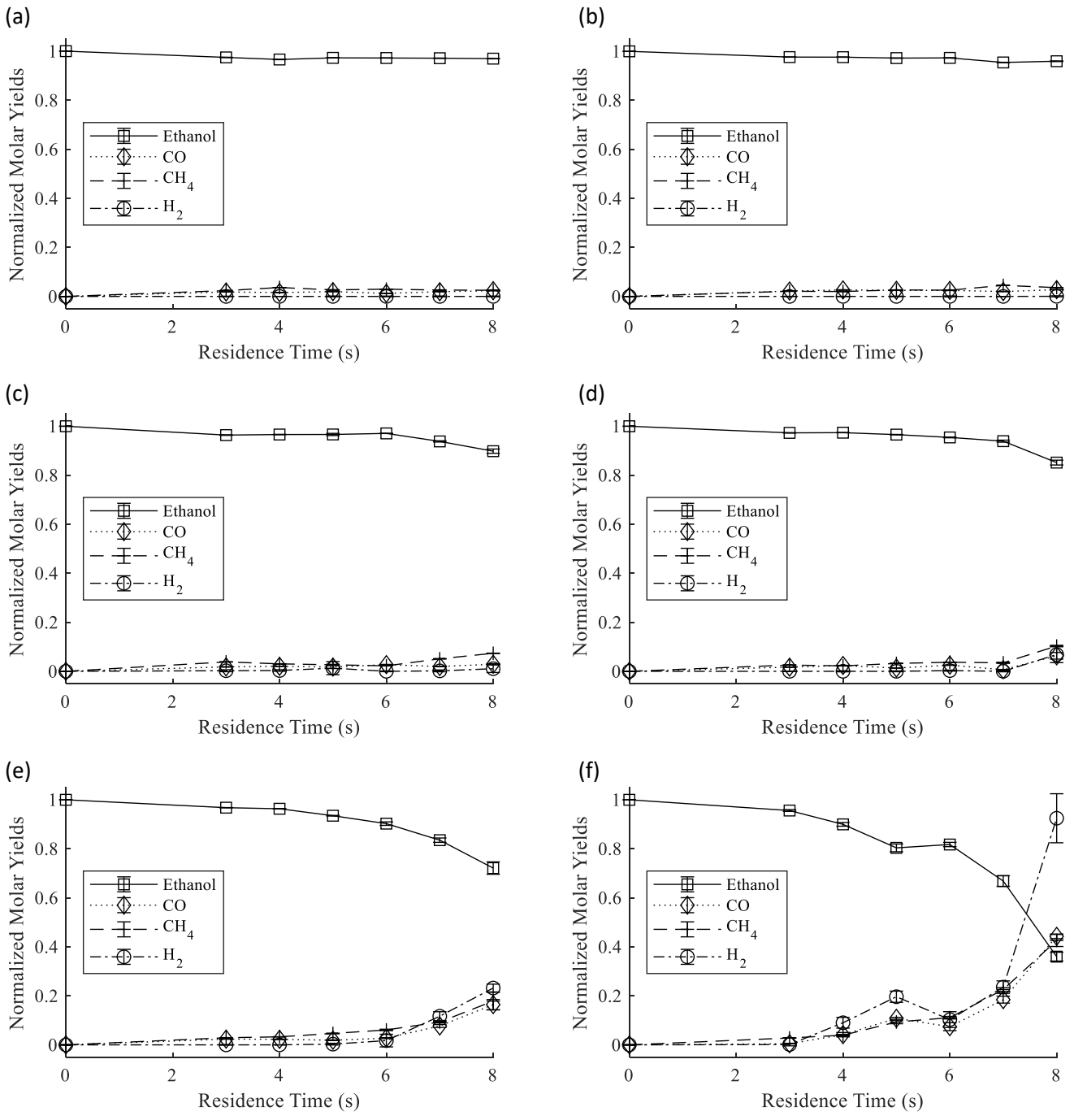

Figure 24: Formation and decomposition of major reaction products during ethanol gasification in SCW at (a) 500 °C, (b) 510 °C, (c) 520 °C, (d) 530 °C, (e) 540 °C, and (f) 550 °C.

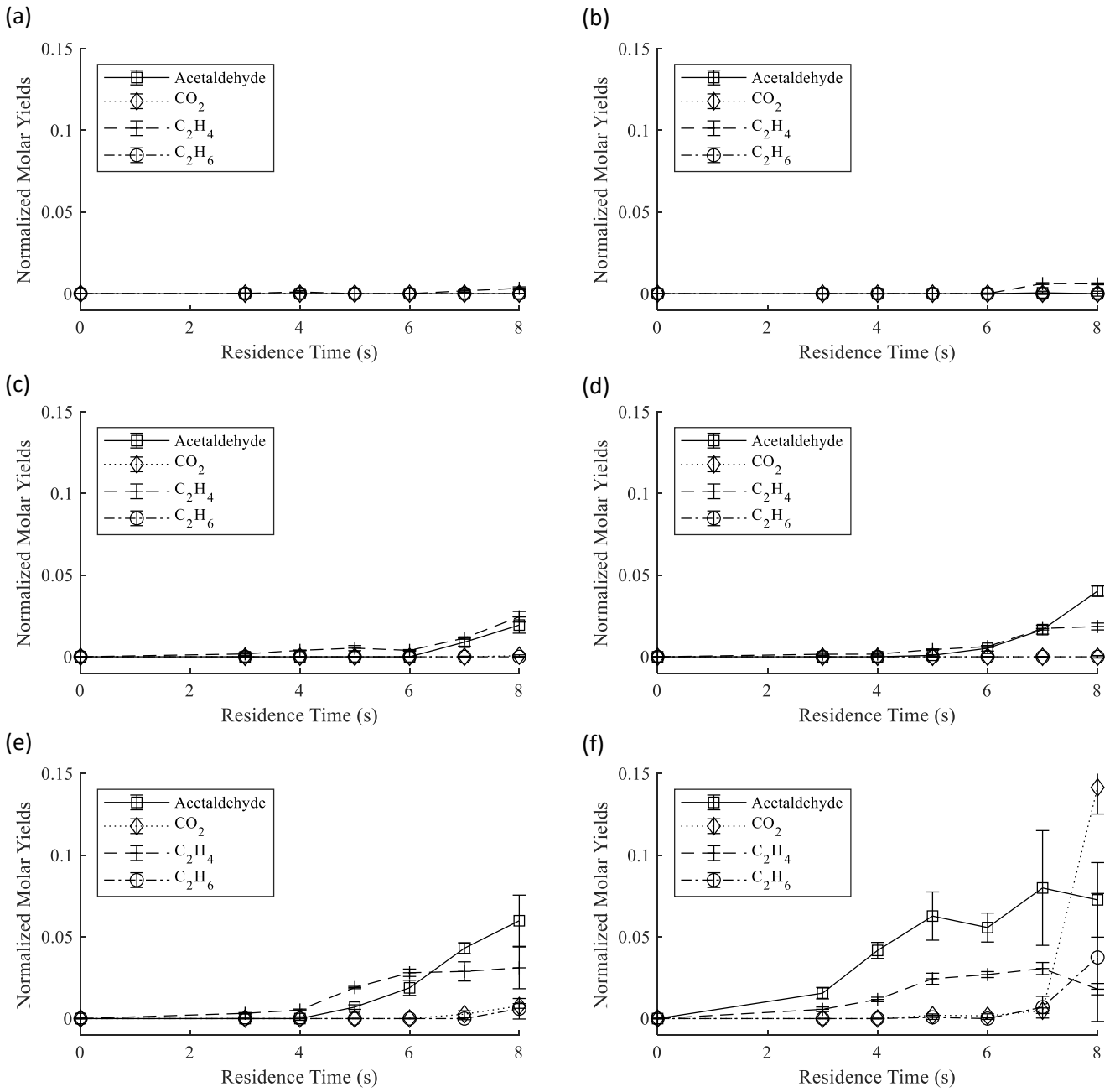

Figure 25: Formation and decomposition of minor reaction products during ethanol gasification in SCW at (a) 500 °C, (b) 510 °C, (c) 520 °C, (d) 530 °C, (e) 540 °C, and (f) 550 °C.

8. Isopropyl Alcohol Gasification

Previous work on SCWG of 1- or 2-propanol is limited. Antal Jr., Carlsson, and Xu [98] report yields of propene (C_3H_6) and 1-propanol after acid-catalyzed dehydration of 2-propanol in subcritical water at 34.5 MPa and 320 °C for residence times up to 100 s. Chakinala et al. [95] gasified 1-propanol in SCW, noting trace yields of benzene and toluene. The postulated reaction network again includes initial C-H and O-H bond scission steps, leading to acetone (C_3H_6O), which is thought to break down to CH_4 and CO. Other theorized steps include reactions to form ethylene, ethane, and various intermediate products.

Isopropyl alcohol (IPA) is continuously fed to the SCWG reactor at an overall volumetric loading of 10 vol%, corresponding to an initial mass fraction of 8.03 wt%. Temperatures were tested from 500 to 560 °C, with pressure fixed at 25 MPa and residence times ranging from 3 to 8 s. IPA was used as received with no further manipulation or purification. Data is collected as described in Section 4.3.

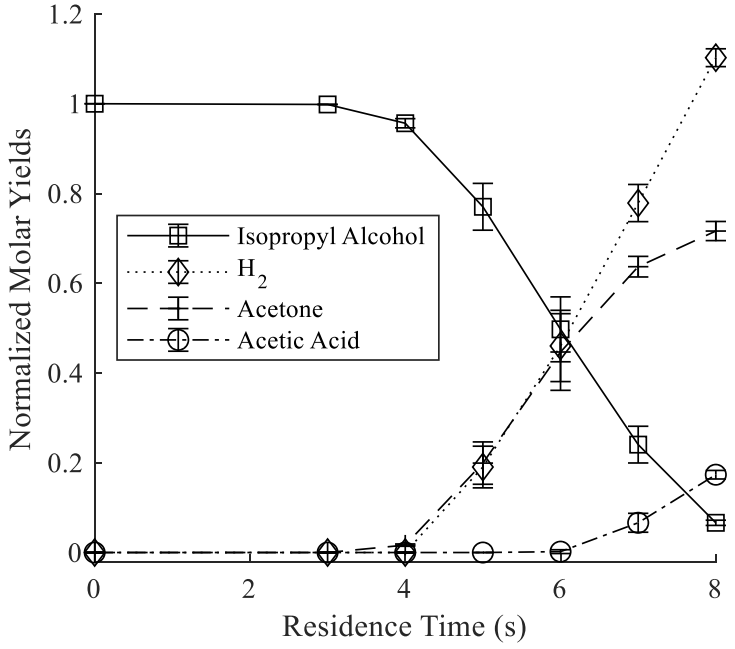

Figure 26: Formation and decomposition of major reaction products during SCWG of IPA at 560 °C.

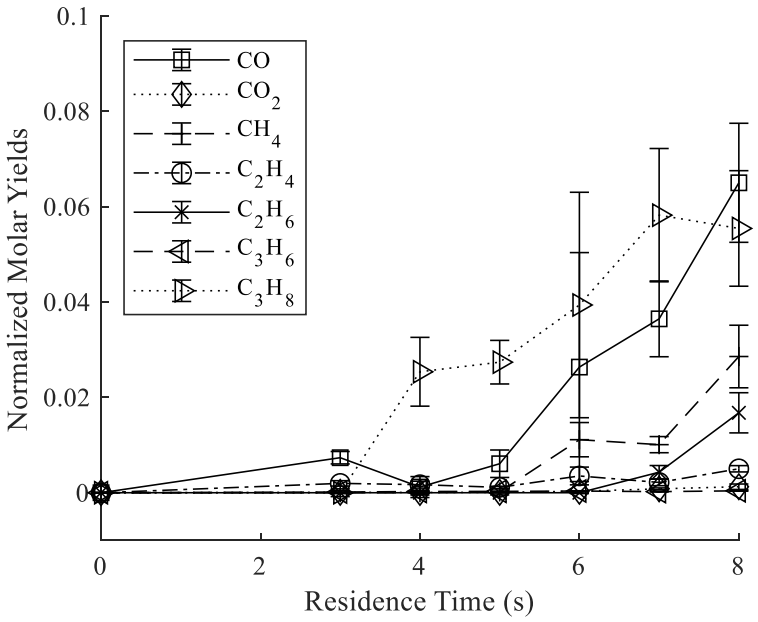

Figure 27: Formation and decomposition of minor reaction products during SCWG of IPA at 560 °C.

Production of H_2 and acetone begin simultaneously and in nearly equimolar quantities from 4 - 6 s, as shown in Figure 26. Acetone can subsequently decompose to several different product species, which leads to its maximum observed yield of 0.72 mol-C_3H_6O/mol-IPA. To identify acetone decomposition products, SCWG of acetone was performed at 560 °C for 8 s. The collected Raman spectrum is available in Figure 31, from which major acetone gasification products were identified as acetic acid and CH_4, with minor yields of H_2, CO, CO_2, ethylene, and ethane. The formation of acetic acid at 7 s in Figure 26 supports this observation, as does the minor production of methane in Figure 27. These observed product formation profiles suggest the proposed acetone decomposition pathways presented in Figure 28. Analysis of IPA data shows many similarities with trends from SCWG of methanol and ethanol, such as the delayed appearance of CO_2 at 7 s. Only trace amounts of C_2H_4, and C_2H_6 are witnessed indicating that conversion of acetone to these products is not favorable.

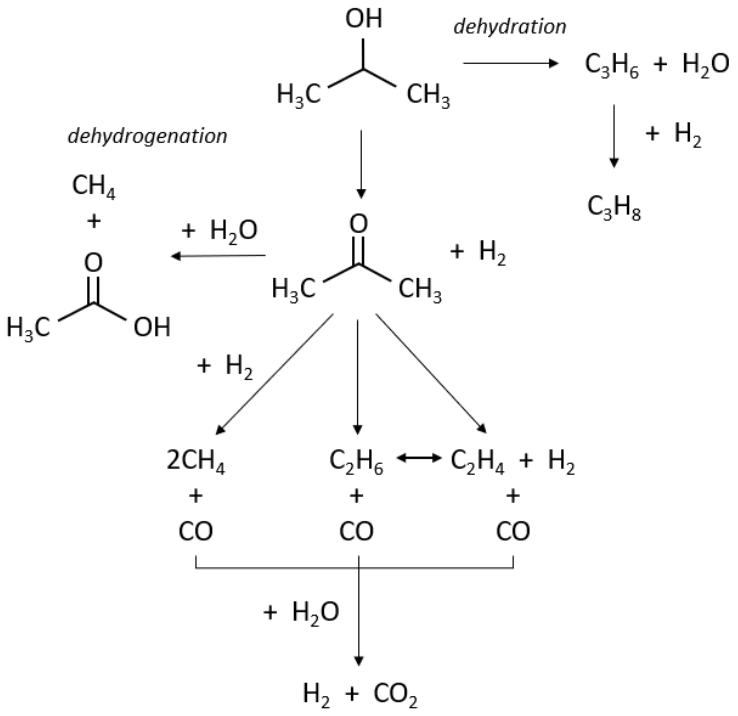

Figure 28: IPA decomposition network in SCW.

Trace propene yields of are detected, which rapidly hydrogenates to a maximum propane yield of 0.06 mol-C_3H_8/mol-IPA at 7 s. Detection of propene and propane confirm the dehydration

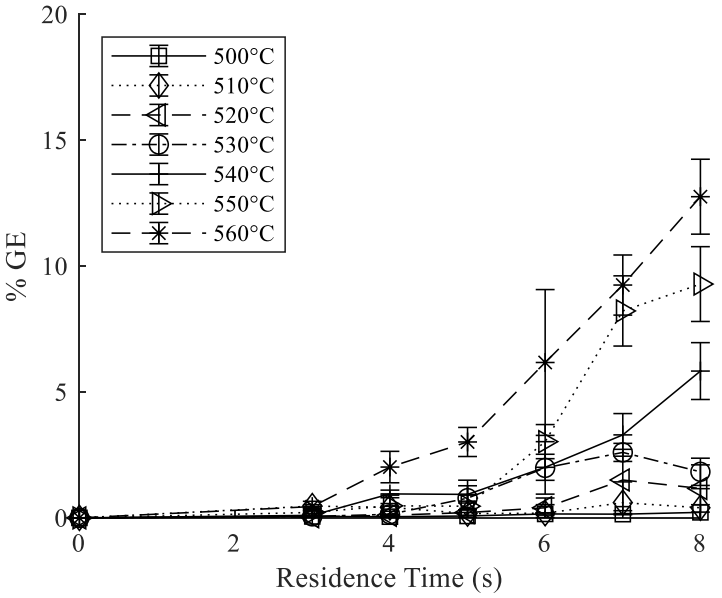

Figure 29: Gasification efficiency of IPA at all tested temperatures.

pathway is active for SCWG of IPA.

Similar to ethanol, we propose that IPA decomposes via competing dehydrogenation and dehydration reaction pathways, as presented in Figure 28. Many of the reaction pathways are inferred from previous knowledge, such as ethylene hydrogenation and the WGS reaction. Acetic acid is a known refractory SCWG product, thus its decomposition to gaseous products is unlikely to be significant [95].

Gasification efficiency is plotted against residence time for all tested temperatures in Figure 29. GE is drastically lower for SCWG of IPA than methanol or ethanol, due to the formation of acetone and acetic acid in significant quantities. Decomposition and formation profiles of IPA reaction products at all tested temperatures are available in Figures 32 and 33. A representative Raman spectrum of IPA decomposition products is presented in Figure 30.

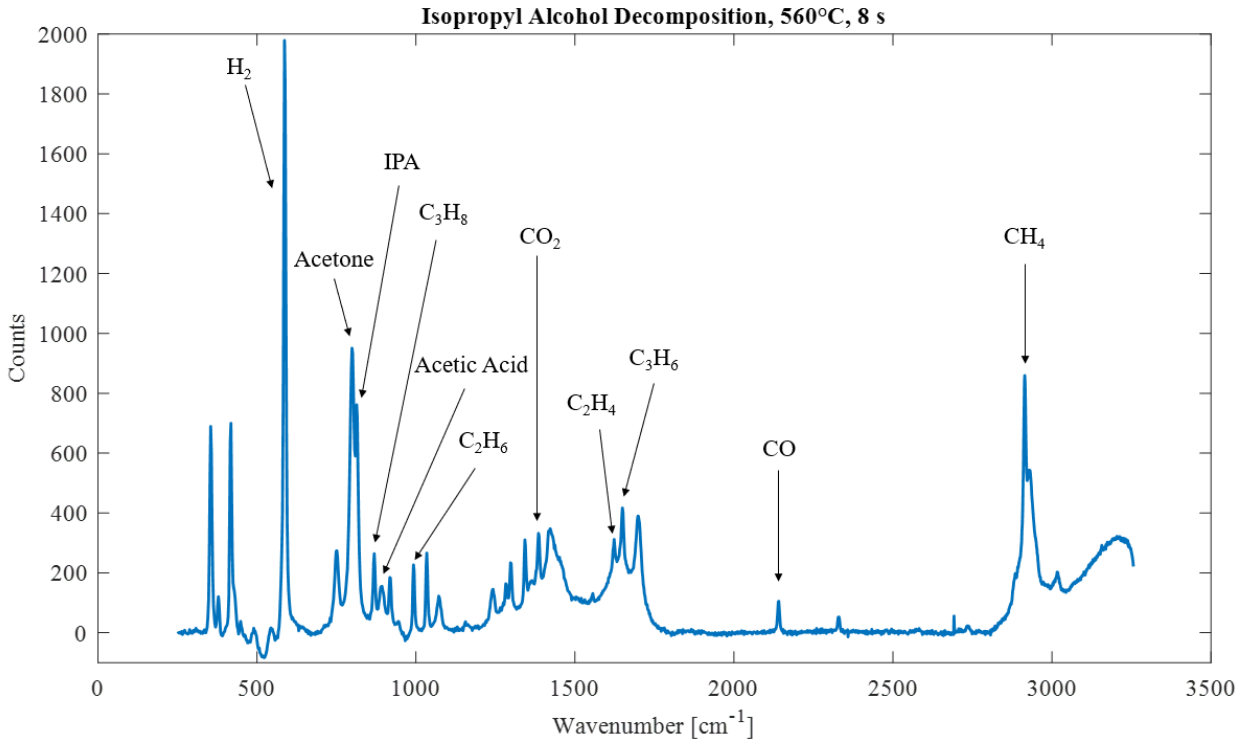

Figure 30: Representative Raman spectrum of isopropyl alcohol decomposition products after gasification for 8 s at 560 °C, with significant peaks identified.

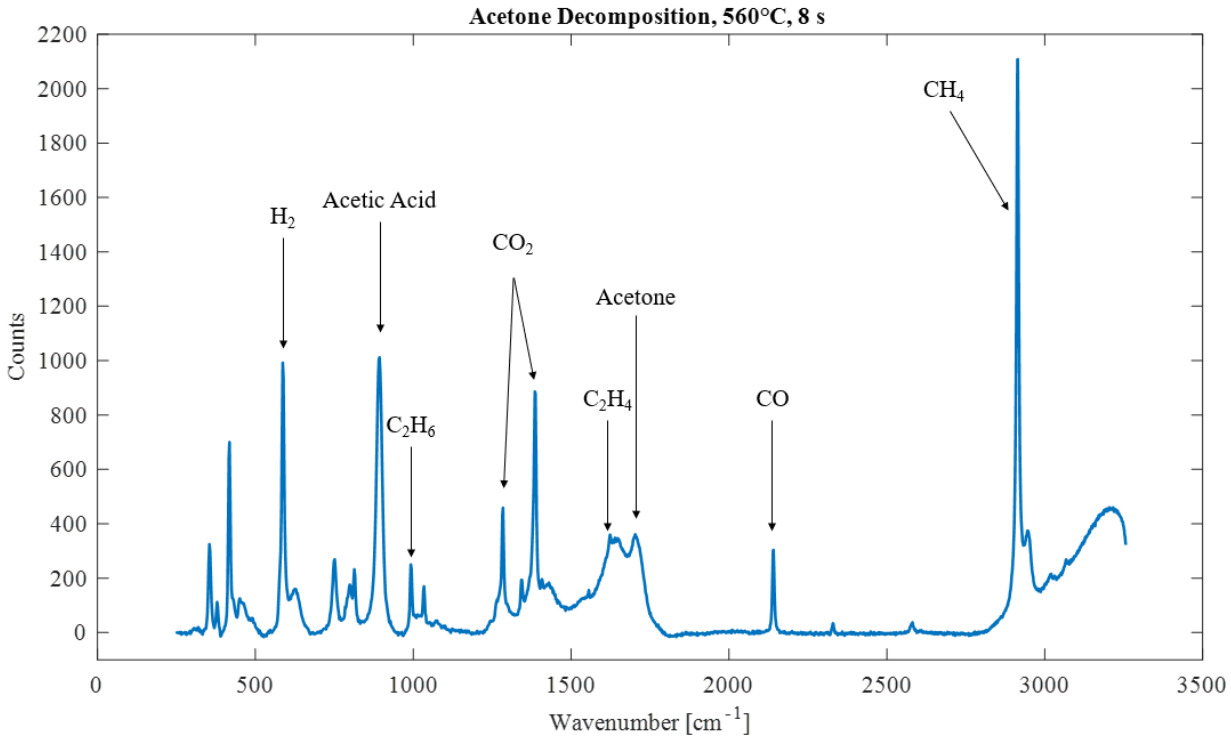

Figure 31: Representative Raman spectrum of acetone decomposition products after gasification for 8 s at 560 °C, with significant peaks identified.

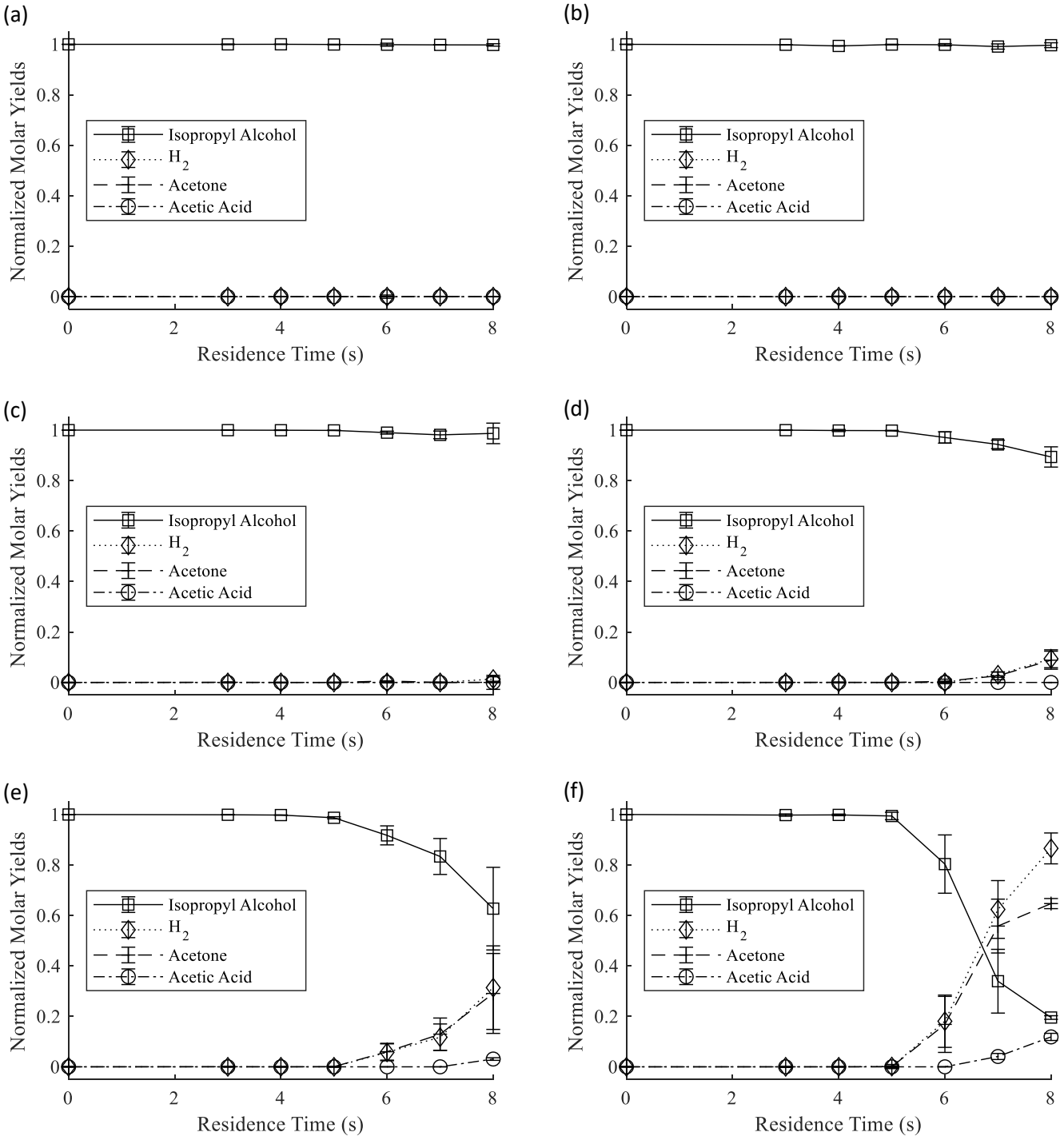

Figure 32: Formation and decomposition of major reaction products during SCWG of IPA at (a) 500 °C, (b) 510 °C, (c) 520 °C, (d) 530 °C, (e) 540 °C, and (f) 550 °C.

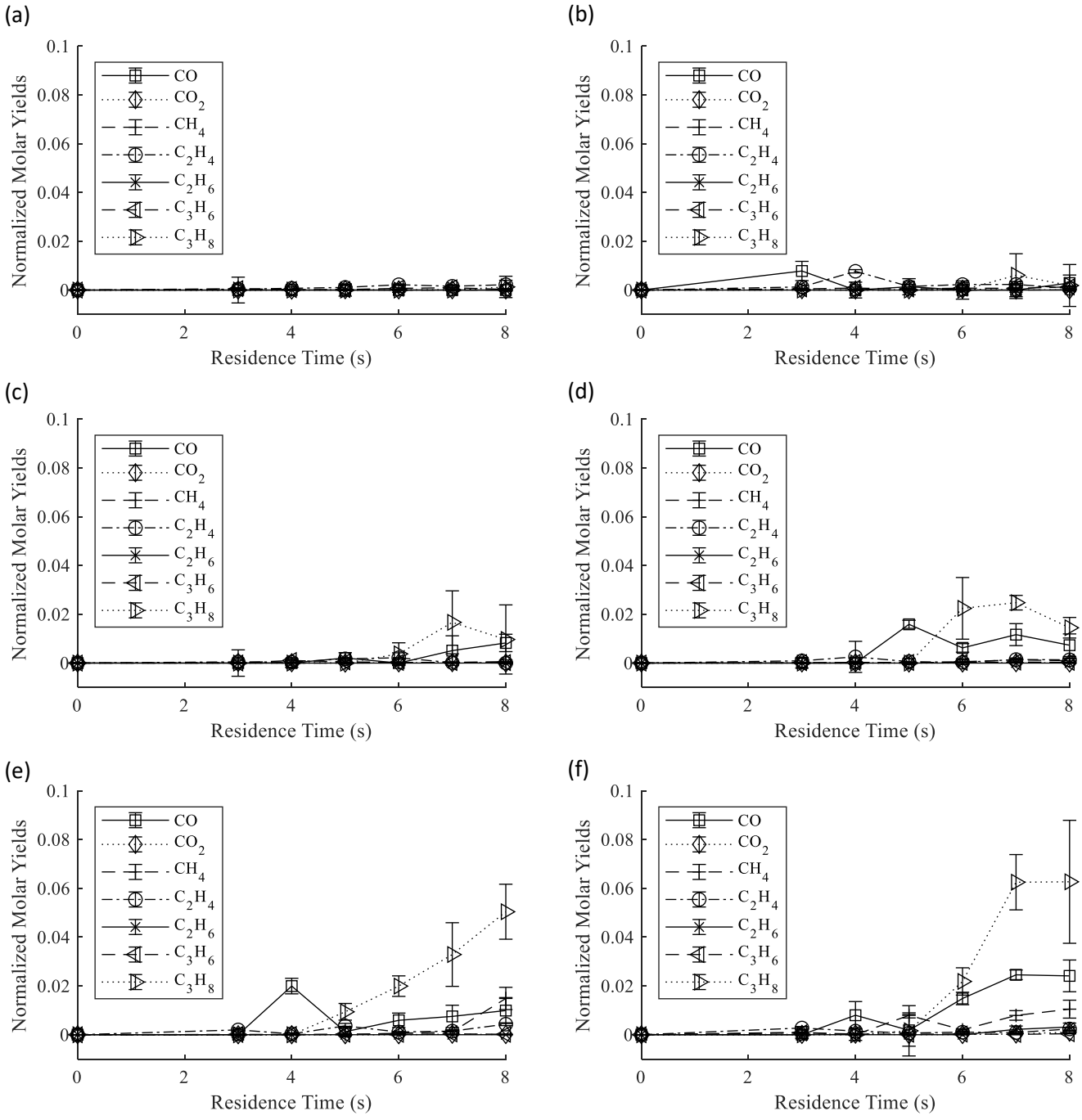

Figure 33: Formation and decomposition of minor reaction products during SCWG of IPA at (a) 500 °C, (b) 510 °C, (c) 520 °C, (d) 530 °C, (e) 540 °C, and (f) 550 °C.

9. SCWG Reaction Mechanisms

The use of *in situ* Raman spectroscopy allows us to perform experiments with much shorter residence times than most previous studies, and with vastly better time resolution, which is a huge benefit for analyzing reaction kinetics. From the resulting decomposition profiles of each model alcohol studied, it is inferred that the mechanisms driving the decomposition of alcohols in SCW are chain-branching, free radical reactions. Based on reaction profiles which consistently show a reaction induction time between 3 and 8 s, we conclude that radical pooling is a key step facilitating alcohol decomposition. The importance of free radical reactions to SCWG chemistry is not particularly surprising, but it is important to consider the chain-branching behavior further, as several previous studies have assumed first-order reaction kinetics for modeling alcohol decomposition in SCW. The next step is to distinguish between reaction initiation steps, propagation steps, and termination steps, considering experimental results presented here and in previously mentioned studies. It is also important to consider the role of heterogeneous catalysis on the surface of nickel reactor walls.

Previous modeling and experimental work have shown that SCW oxidation chemistry of alcohols is analogous to the oxidation chemistry of alcohols under standard combustion conditions [99]. It follows that reactions of alcohols in SCW without an oxidant would follow similar reaction mechanisms as those already described and quantified in the pyrolysis and combustion literature involving homolytic dissociation reactions and non-oxidative radical chain reactions.

9.1. Reaction Initiation Mechanisms

The most probable reaction initiation step during non-catalytic SCWG is homolytic dissociation of the parent alcohol via scission of the weakest bond, namely the C-O (methanol) or the C-C (ethanol and IPA) bond. However, Chakinala et al. [95] reported that alcohols are mostly stable in SCW up to 600 °C in the absence of a catalyst, which is mostly confirmed by the long conversion times reported in other batch studies in this temperature region [21, 97]. Thus, homolytic dissociation is not a likely initiation step during continuous SCWG at 500 to 560 °C within a nickel-base tubular reactor. Much more likely is that radicals are initially generated through adsorption and decomposition mechanisms on the catalytic surface of the reactor walls. This adsorption and decomposition step is thought to proceed through adsorption of an H from the parent hydrocarbon onto the catalytic surface, followed by the release of the remainder of the parent molecule back into the bulk flow in the form of a highly-reactive free radical [37, 94].

If homolytic dissociation of ethanol or IPA were key initiation steps, this would initially generate methyl radicals in the bulk flow through C-C bond scission, leading to yields of CH_4 and ethane prior to observable yields of ethylene, acetaldehyde, or acetone. However, this is not the behavior observed in these experiments. For SCWG of ethanol, methane is only found after a significant formation of acetaldehyde.

As further evidence for this hypothesis, alcohol combustion studies have shown that homolytic dissociation of methanol to methyl (CH_3) and hydroxyl (OH) radicals through C-O bond cleavage is a negligible reaction mechanism [100, 101]. The absence of CH_4 and ethane as products from methanol SCWG indicates that this finding holds in SCW environments, as both would be

present as reaction products if methyl radicals were formed in the reaction environment. It follows that C-O bond cleavage during SCWG of ethanol and IPA would also be negligible.

9.2. Reaction Propagation Mechanisms

Once intermediate radicals are catalytically generated, they can initiate chain reactions through propagation steps, such as H abstraction from the parent alcohol via intermediate radicals. For methanol, initial catalytic H abstraction most probably forms CH_2OH radicals. A less probable step is also available, via O-H scission to CH_3O. Both of these steps are consistent with the mechanism proposed by Chakinala et al. [95]. Each radical rapidly reaches formaldehyde through unimolecular beta-scission, generating a growing radical pool and propagating the chain-branching reaction. Formaldehyde rapidly reacts to CO and H_2; aldehydes are highly sensitive to radical attack and are short-lived at the conditions tested [101].

In the case of ethanol, Norton and Dryer [101] concluded that the variation in observed products during ethanol oxidation was largely dependent on the initial site of H abstraction. This finding seems to hold for SCWG of ethanol. Three potential C_2H_5O isomers are energetically available based on relative bond energies: CH_3CHOH, C_2H_4OH, and CH_3CH_2O [99, 100]. These isomers can then react via the following dissociation reactions:

$$CH_3CHOH \cdot \rightarrow C_2H_4O + H \cdot \quad (25)$$

$$C_2H_4OH \cdot \rightarrow C_2H_4 + OH \cdot \quad (26)$$

$$CH_3CH_2O \cdot \rightarrow CH_2O + CH_3 \cdot \quad (27)$$

all of which produce more free radicals in the reaction environment to speed the initial H abstraction step. No formaldehyde was detected during SCWG of ethanol; it is likely that it decomposes to CO and H_2 too quickly to be detected.

It is reasonable to extrapolate dominant IPA mechanisms based on methanol and ethanol mechanisms. The C_3 chain affords four potential C_3H_7O isomers after H abstraction from the parent IPA molecule. If the reaction behavior is similar to ethanol, (and the similarity of the reaction network and decomposition profiles seems to indicate that it is), these isomers could plausibly react via the following reactions:

$$CH_3CH_2CHOH\cdot \rightarrow C_3H_6O + H\cdot \quad (28)$$

$$CH_3CHCH_2OH\cdot \rightarrow C_3H_6O + H\cdot \quad (29)$$

$$C_3H_6OH\cdot \rightarrow C_3H_6 + OH\cdot \quad (30)$$

$$CH_3CH_2CH_2O\cdot \rightarrow CH_2O + C_2H_5\cdot \quad (31)$$

Acetone is the dominant intermediate from IPA decomposition. Similar to formaldehyde and acetaldehyde, the C=O double bond in the acetone molecule is stable under SCWG conditions. Acetone decomposition in SCW must proceed through C-C bond scission, forming a methyl radical and a methylcarbonyl radical (C_2H_3O). The methylcarbonyl radical can hydrolyze to form acetic acid and an H radical, which appears to be the favored acetone reaction pathway. The presence of methyl radicals can explain the major yield of CH_4 from SCWG of acetone, and the minor yields of ethane and ethylene. Because the molar yields of acetic acid are consistently higher than the molar yield of CH_4, it seems highly unlikely that acetone can simultaneously lose both methyl radicals along the hydrogenation pathway in Figure 28; however, it is included for completeness.

9.3. Reaction Termination Mechanisms

Stable end-products during the SCWG of all alcohols studied include H_2, CO_2, CH_4, ethane, and propane. H_2 is produced through the coupling of two H radicals, either in the bulk flow or through abstraction of a H atom via a H radical. CO_2 is reached through the forward WGS reaction, which is favored over the reverse reaction under high-temperature, aqueous conditions. Methyl radicals (likely only formed from acetaldehyde or acetone) are quick to abstract H from other hydrocarbons to form stable CH_4. The combination of two methyl radicals to form ethane is unlikely, due to the high reactivity of methyl radicals and low probability of encountering another methyl radical relative to possible H donors.

9.4. Char Formation Mechanisms

The abstraction of H atoms through C-H and O-H bond scission is shown to occur readily in SCW, even in the absence of an oxidant. The initial abstraction mechanisms must result from radicals present in SCW above 500 °C, or from catalytic abstraction. As the radical pool grows, H abstraction accelerates, leading to the observed chain-branching decomposition profiles. Additionally, open C bonding sites become active. This could explain previously published results, where char yields during SCWG of aromatic compounds or heterogeneous feedstocks are higher than expected [104].

Soot formation occurs during the combustion of hydrocarbons, via the H-abstraction, C_2H_2-addition (HACA) mechanism, as first proposed by Frenklach [105]. As H is abstracted from aromatic compounds, the open bonding sites become occupied by acetylene (C_2H_2) radicals resulting in polyaromatic hydrocarbon (PAH) growth and soot formation in flames. The HACA

regime is dominant under high concentrations of H radicals and low concentrations of O radicals. As demonstrated here, SCWG produces copious H radicals when hydrocarbons are present. During SCWG of aromatic compounds, char formation likely proceeds via mechanistically similar or identical steps to HACA. There exists support for this hypothesis in a recent study by Matsumura et al. [106], where H radical scavengers were shown to effectively suppress char formation during SCWG of guaiacol.

10. Partial Oxidation of Ethanol

A limited number of previous studies have investigated supercritical water processing of model compounds with the addition of an oxidant at low relative concentrations [107-109]. Biomass and other waste feedstocks tend to have high oxygen contents (often > 50 wt%) [110], indicating that reactions involving oxygenated species and oxidative radicals will be significant to SCWG of practical feedstocks.

From previous SCWO studies, ethanol oxidation occurs nearly instantaneously at temperatures above 500 °C [96]. SCWG reactions are not significantly initiated at temperatures below 530 °C and residence times below 8 s [111]. By studying the intermediate region where SCWO reactions occur rapidly, and SCWG reactions occur slowly, insight is sought toward the initial SCWO reaction steps, and the interaction of intermediate products at temperatures above 500 °C in the absence of further oxidant. By selecting ethanol as a simple model compound with well-described reaction chemistry, the effect of partial oxidation conditions on reaction pathways can be confidently inferred from resulting product yields.

10.1. Reactor Modifications

Minor reactor modifications are made to introduce the oxidant to the reaction environment. Figure 34 shows a schematic of the reactor, which has three independent HPLC pumps to introduce deionized (DI) water, aqueous H_2O_2 (30 wt%), and pure ethanol into the reaction environment. The oxidant pump allows for independent selection of OFR, in addition to residence time and

reagent concentration. The DI water and H_2O_2 streams are mixed prior to preheating, to ensure that the H_2O_2 is well-mixed and fully decomposed to O_2 before the introduction of the ethanol.

H_2O_2 decomposition rates in SCW were previously quantified by Croiset, Rice and Hanush [112] with a first-order Arrhenius expression of:

$$k\ (s^{-1}) = 10^{13.4\pm1.2}\exp\left[\left(-180 \pm 16\ \frac{kJ}{mol}\right)/RT\right] \quad (32)$$

H_2O_2 decomposes to H_2O and O_2 via intermediate OH and HO_2 radicals, which are assumed to exist in constant concentrations at equilibrium. Our preheater section consists of a coiled, 6.1 m Inconel 625 tube with 3.05 mm ID, resulting in an internal preheater volume of 472 mL. The

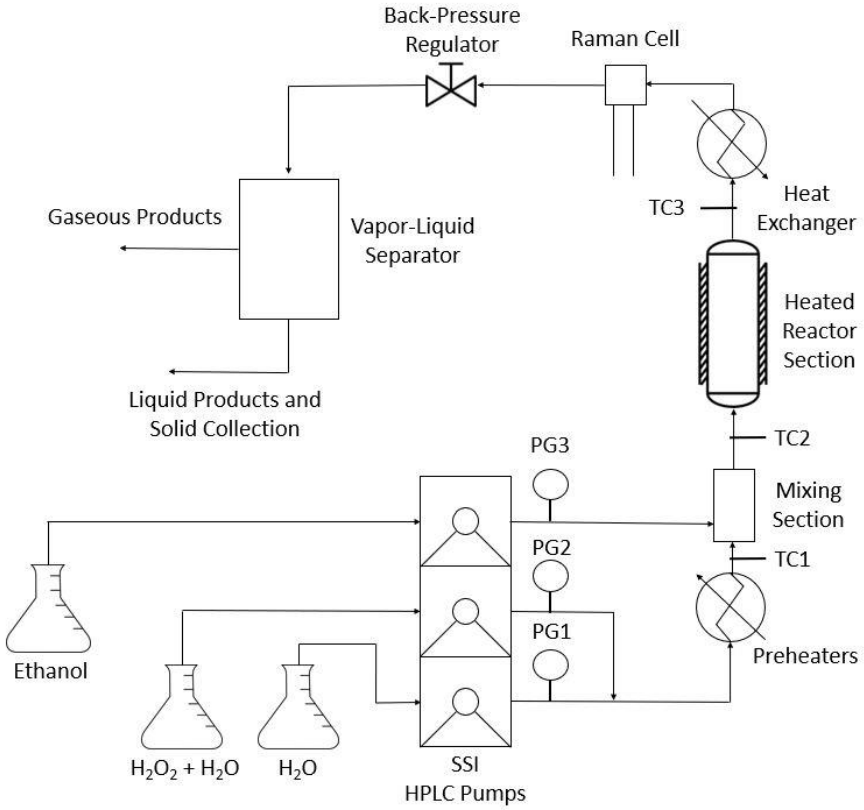

Figure 34: Schematic of the continuous supercritical water reactor used for partial oxidation experiments. PG = pressure gauge, TC = thermocouple.

maximum total mass flow rate of the premixed DI water and H_2O_2 through the preheater is 31.2 g/min. At 600 °C and 25 MPa the density of water is 0.055 g/mL [29]; thus, an approximate minimum residence time of oxygenated water in the preheater can be calculated as 49.9 s, if the maximum possible flow rate and temperature are assumed. From the above Arrhenius expression, H_2O_2 is 99% decomposed after 0.267 s at 500 °C, and 0.0108 s at 600 °C. To achieve post-mixing temperatures of 500 to 530 °C, the preheated bulk flow must consistently be heated to >600 °C, as measured by TC1; it is reasonable to assume that H_2O_2 is fully decomposed to O_2 by the time the oxygenated bulk flow reaches the mixing section.

For all partial oxidation experiments, the thermal management procedure is as follows. First, the desired experimental temperature is reached, as measured by TC2 and TC3 (Figure 34), with cold ethanol injected into a bulk flow of supercritical water. Next, the flow of H_2O_2 is initiated. When the oxygenated bulk flow reaches the mixing section and reacts with the inflowing ethanol, a measurable temperature increase is observed at TC2, recorded as the post-mixing temperature increase in Table 6. The post-mixing temperature increase is correlated to OFR, as seen in Table 6. On average, OFRs of 5, 7.5, and 10% cause respective temperature increases of 11.0, 16.4, and 21.7 °C. Across all experiments, the measured post-reactor temperature at TC3 closely matches the experimental temperature, indicating that the temperature of the bulk flow quickly returns to the intended experimental temperature.

Table 6. Temperature increase after the introduction of reagent into partially oxidative bulk flow.

Experimental Temperature (°C)	OFR (%)	Post-Mixing Temp. Increase (+°C)	Post-Reactor Temp. Increase (+°C)
500	5	11±1.1	2.7±0.56
	10	22±2.8	2.4±0.77
510	5	12±2.2	0.19±1.6
	7.5	17±3.7	1.9±0.84
	10	22±4.4	3.0±0.89

520	5	9.7±1.3	0.04±1.2
	7.5	16±3.1	2.7±1.9
	10	18±6.2	0.13±1.1
530	5	12±1.3	1.8±0.54
	7.5	16±2.4	1.9±0.61
	10	23±0.54	1.9±0.71

10.2. Product Yields

Figures 36 through 39 show molar product yields normalized to 1 mol of ethanol for all SWPO experimental conditions. Ethanol yield values in Figures 36 through 39 indirectly indicate ethanol conversion values for each experimental condition (*e.g.,* ethanol yield of 0.6 mol corresponds with 40% ethanol conversion). Measured ethanol yields show that ethanol conversion values at these conditions are consistently over four times higher than the experimental OFR. This seems to indicate that most of the initially available oxygen is rapidly consumed through reactions with the parent ethanol molecules. A lack of detectable O_2 or H_2O_2 in the product spectra indicates that oxygenated species are rapidly and completely consumed in all experiments.

During SWPO, molar H_2 yields are significantly lower than molar CO and CH_4 yields, which also supports the hypothesis that most available oxygen is rapidly consumed in the reaction with ethanol molecules. Ethanol oxidation proceeds initially to a C_2H_5O isomer through hydrogen abstraction by an oxidative radical (*e.g.,* OH or HO_2), which produces H_2O rather than H_2. Consistently, the CO yield is nearly equal to the amount of converted ethanol on a molar basis. CO_2 yields never exceed 0.04 mol/mol-EtOH, indicating that conversion of CO via the WGS reaction happens slowly at these conditions and that insufficient oxidant remains for CO oxidation by the time is forms in significant quantity [113].

Molar CH_4 yields are consistently lower than molar CO yields, indicating CO is formed via pathways additional to acetaldehyde decomposition, and/or that CH_4 undergoes partial oxidation at these conditions. Higher OFRs produce greater relative differences between molar CH_4 and CO yields. Full oxidation of CH_4 would produce H_2O and CO_2, but again CO_2 yields are consistently low. Partial oxidation of CH_4 may produce CH_2 or CH_3 radicals, which can couple to form ethylene or other C_2 species [101].

As shown in SCWG experiments, ethanol can dehydrogenate to form H_2 or dehydrate to form ethylene in the absence of an oxidant. It is possible that the temperature increase produced through exothermic oxidation reactions promote these hydrolysis pathways, which could explain the slight increase in ethanol conversion and H_2 yield with residence time.

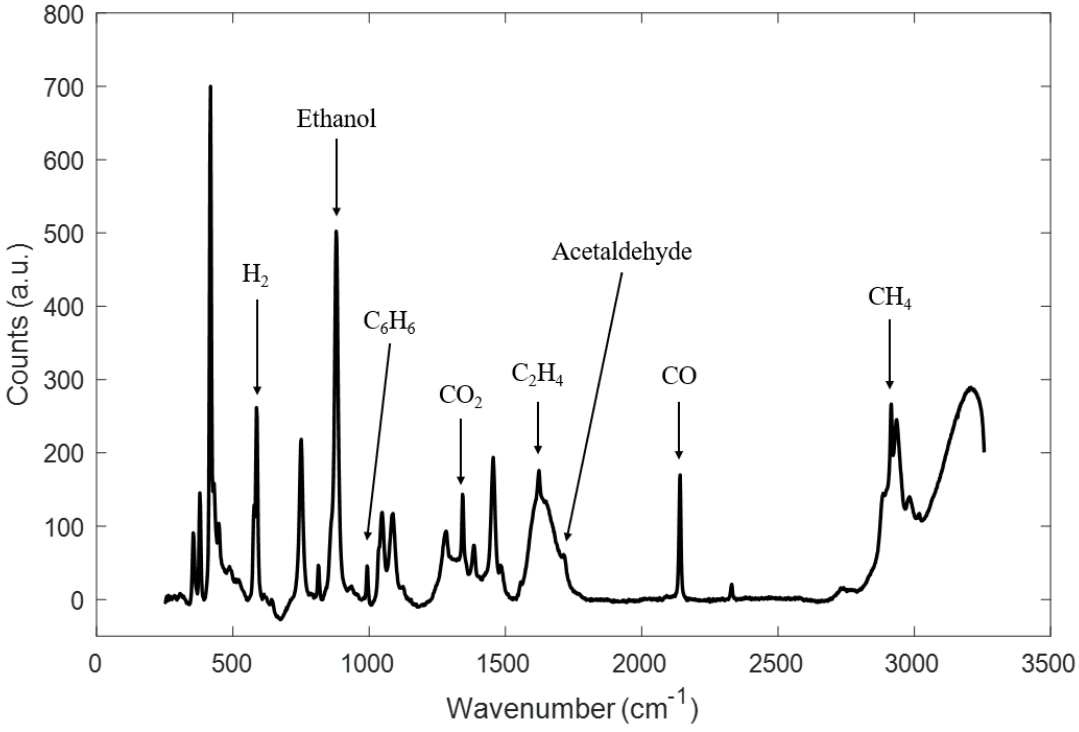

Figure 35: Representative Raman spectrum from partial oxidation of ethanol in supercritical water at 530 °C, residence time of 6 s, and OFR of 10%. Significant peaks are correlated with associated species.

A Raman peak at 992 cm^{-1} is visible in data collected at higher residence times, as shown in Figure 35. Both ethane (C_2H_6) and benzene (C_6H_6) have a characteristic peak at this wavenumber. We infer that benzene is the primary contributor to the appearance of this peak because increases in the 992 cm^{-1} peak height are consistently accompanied by increases in H_2 molar yields. Production of 1 mol ethane would require the consumption of 1 mol H_2 via ethylene hydrogenation, while production of 1 mol benzene via ethylene dehydrogenation and acetylene (C_2H_2) pyrolysis produces 3 mol of H_2 [102, 114]. The corresponding increase in the 992 cm^{-1} peak height and H_2 yield serves as an indicator that this peak is due to benzene presence. Char and coke formation within the reactor support this conclusion, as does the previous observation of trace benzene yields from bioethanol reforming in supercritical water [115]. It is probable that ethane is also present in trace amounts.

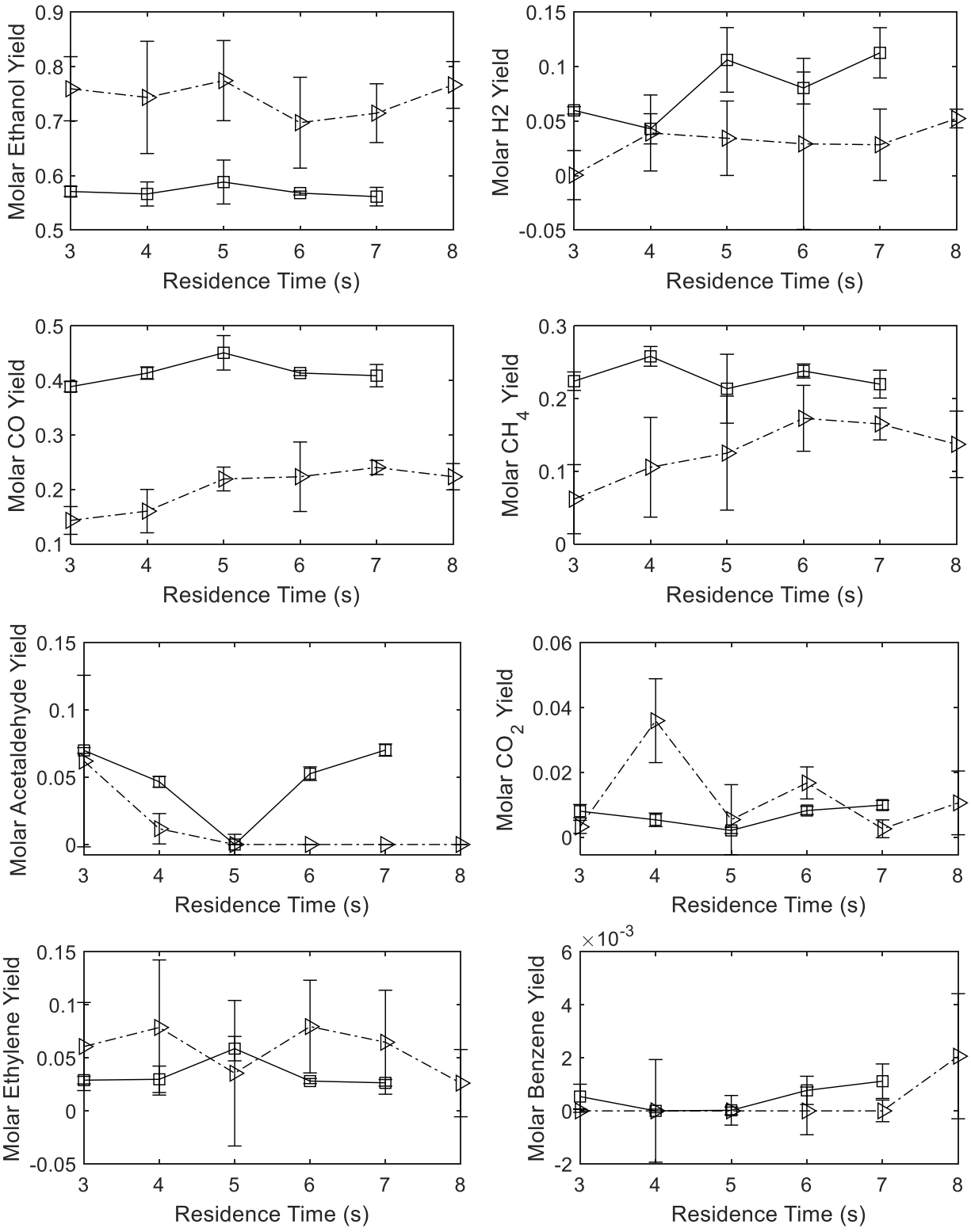

Figure 36. Product yields (normalized to 1 mol ethanol) vs. residence time for SWPO of ethanol at 500 °C. ▷-·- OFR = 5%, □– OFR = 10%

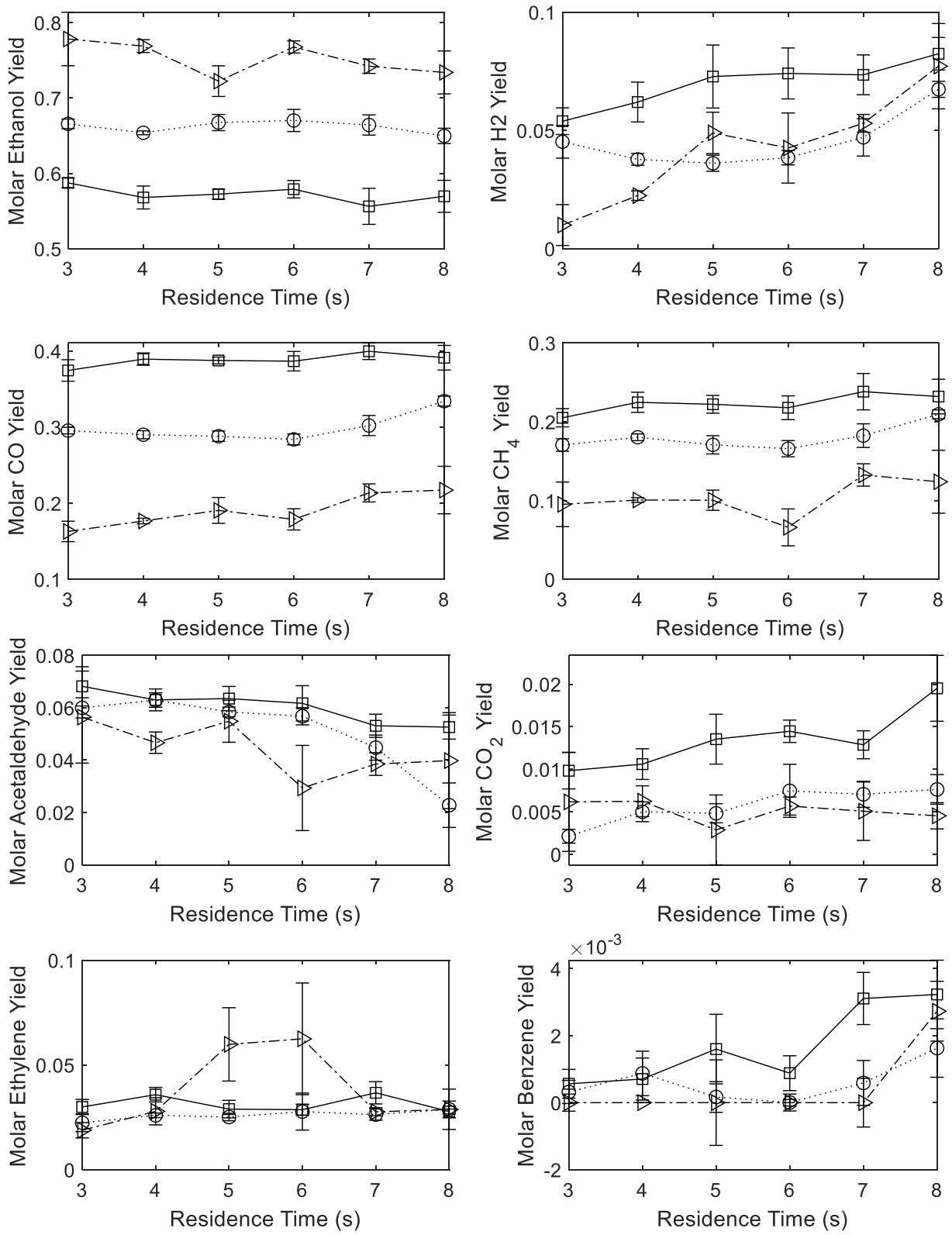

Figure 37. Product yields (normalized to 1 mol ethanol) vs. residence time for SWPO of ethanol at 510 °C. ▷-·- OFR = 5%, ○··· OFR = 7.5%, □– OFR = 10%

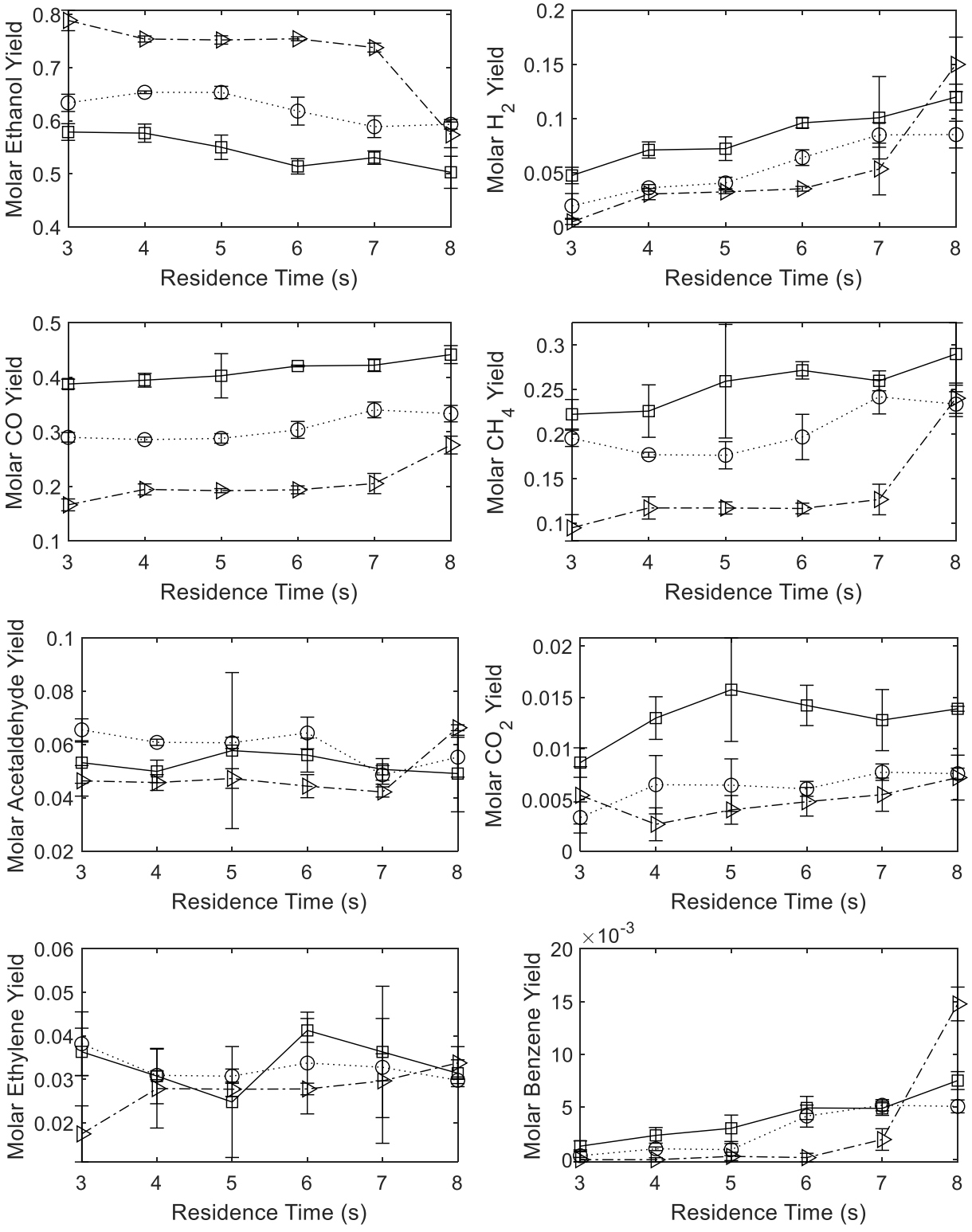

Figure 38. Product yields (normalized to 1 mol ethanol) vs. residence time for SWPO of ethanol at 520 °C. ▷-·- OFR = 5%, ○··· OFR = 7.5%, □– OFR = 10%

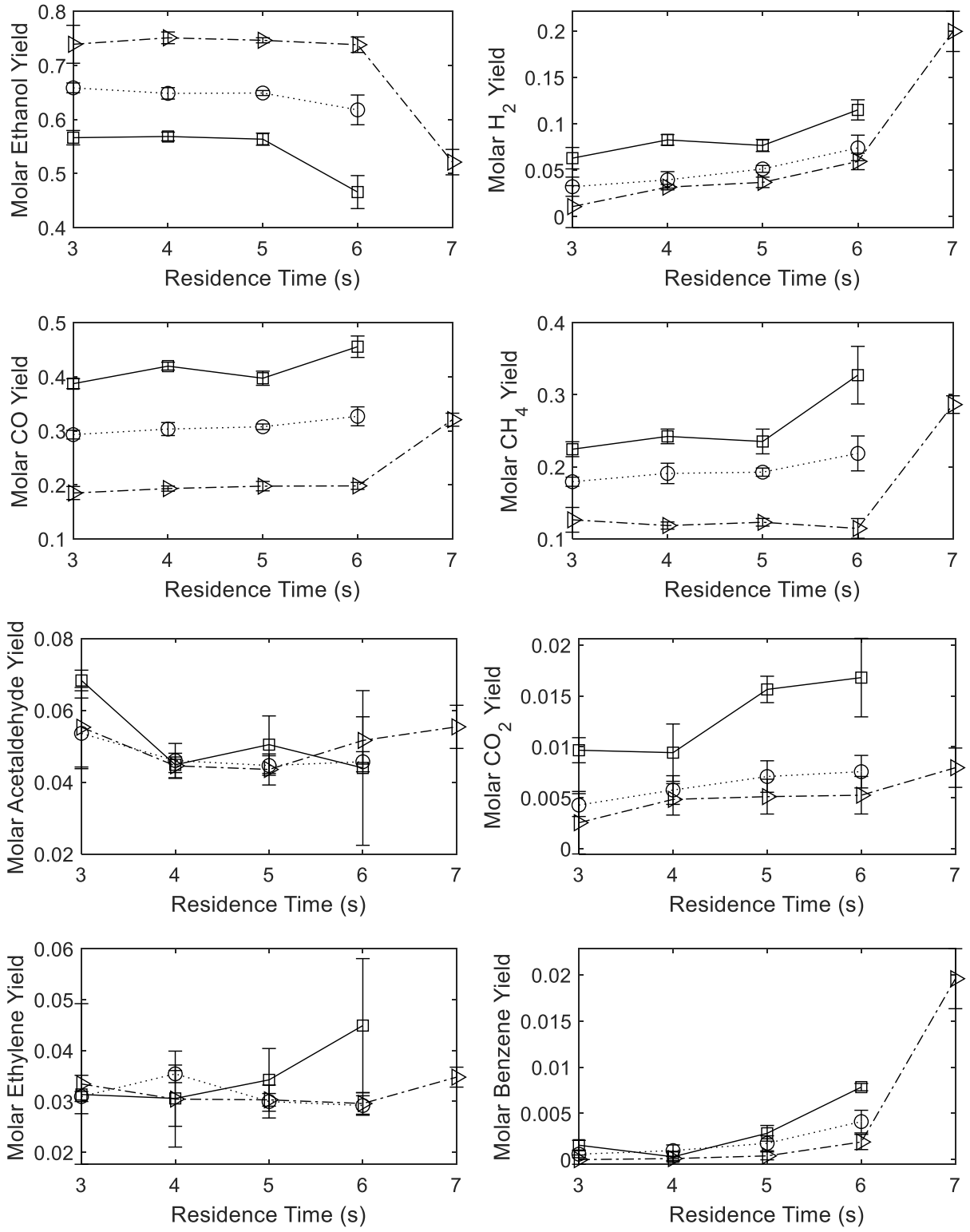

Figure 39. Product yields (normalized to 1 mol ethanol) vs. residence time for SWPO of ethanol at 530 °C. ▷-·- OFR = 5%, ○··· OFR = 7.5%, □– OFR = 10%

10.3. Gasification Efficiency

GE is plotted in Figure 40 against residence time for all temperatures and OFRs. Increased OFR corresponds with an increase in gaseous product yield, while increased temperature and residence time each correspond with minor increases in GE at these conditions. The insignificance of temperature and residence time is expected, as the oxidation steps responsible for most ethanol conversion occur rapidly at these conditions. A maximum GE of 45% is reached after 6 s at 530 °C and an OFR of 10%. Figures 36 through 39 show that gaseous products are primarily CO, CH_4,

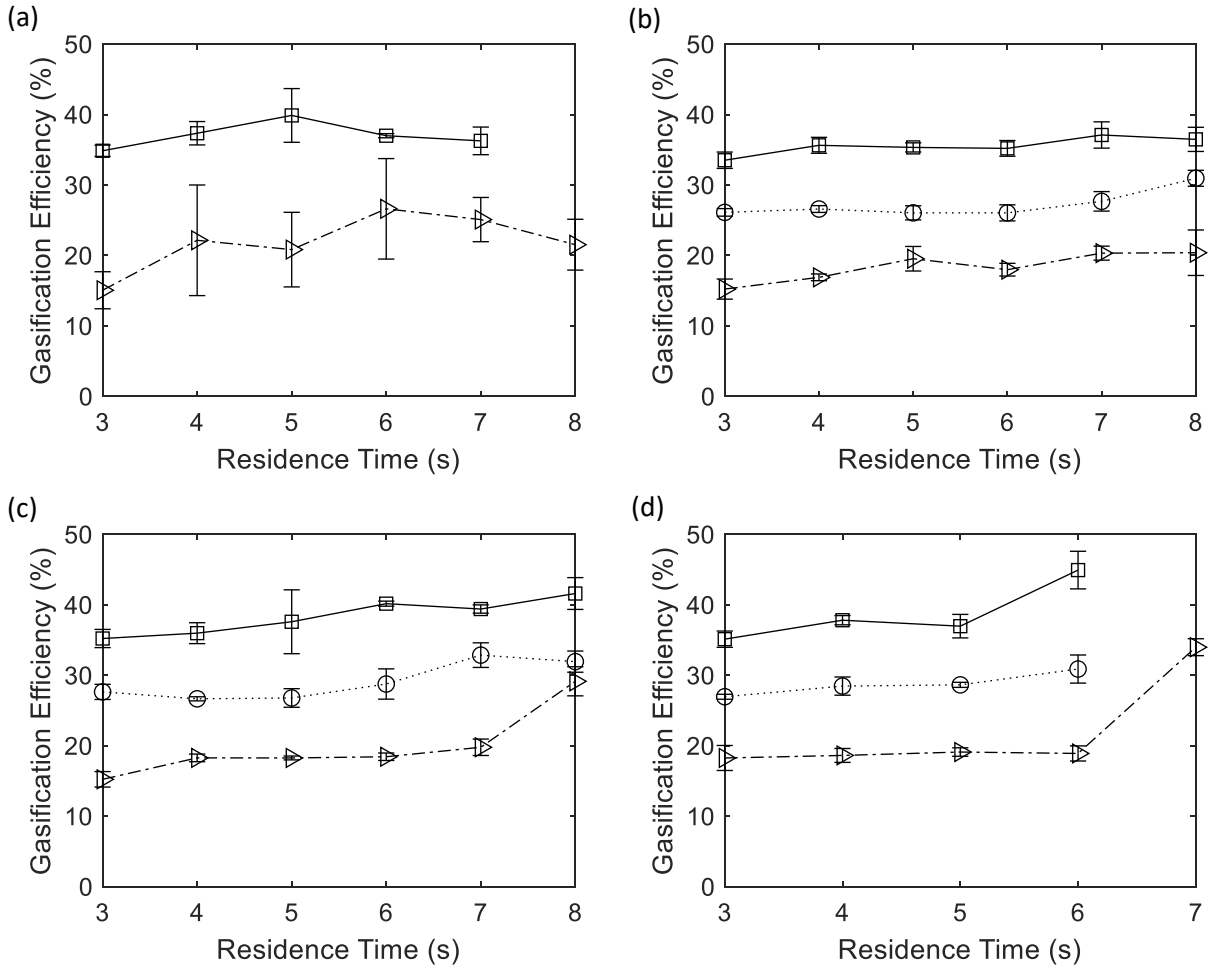

Figure 40. Plots of gasification efficiency vs. residence time for ethanol under SWPO conditions at (a) 500 °C, (b) 510 °C, (c) 520 °C, and (d) 530 °C. ▷-·- OFR = 5%, ○··· OFR = 7.5%, □– OFR = 10%

and H_2. GE never exceeded 6% during previous experiments running SCWG of ethanol with the same reactor at temperatures from 500 to 530 °C and residence times up to 8 s, shown in Figure 22.

10.4. Reaction Mechanisms

It has been well-documented that oxidation of ethanol in the gas-phase initially through hydrogen abstraction to form one of three C_2H_5O isomers:

$$C_2H_5OH + X \rightarrow CH_2CH_2OH\cdot + XH \quad (32)$$

$$C_2H_5OH + X \rightarrow CH_3CHOH\cdot + XH \quad (33)$$

$$C_2H_5OH + X \rightarrow CH_3CH_2O\cdot + XH \quad (34)$$

The temperature-dependent branching ratio between the three isomers is important to the dominant reaction pathways and ultimate product yields [101, 102, 111]. Each isomer subsequently decomposes via third-body reaction:

$$CH_2CH_2OH\cdot + M \rightarrow C_2H_4 + OH\cdot + M \quad (35)$$

$$CH_3CHOH\cdot + M \rightarrow CH_3CHO + H\cdot + M \quad (36)$$

$$CH_3CH_2O\cdot + M \rightarrow CH_3\cdot + CH_2O + M \quad (37)$$

producing key intermediates of acetaldehyde, ethylene, and CH_4. These same mechanisms are active in ethanol oxidation and hydrolysis in SCW, with acetaldehyde production (Equations 33 and 36) known as the preferred route [96, 111, 116].

Under the studied SWPO conditions, the oxidative species are favored to facilitate the initial hydrogen abstraction steps in Equations 32 through 34. The catalytic reactor surface may also initiate hydrogen abstraction. The resulting radicals produced by Equations 35 through 37 cause a propagating chain reaction, as species such as CH_3 and OH are highly reactive for hydrogen abstraction, forming stable products of CH_4 and H_2O [101]. Under SCWG conditions, radical generation subsequently leads to chain-branching behavior, where reaction propagation led to self-catalyzing, accelerating ethanol conversion, as shown in Chapter 8. Interestingly, in these experiments, the chain reactions terminate before complete ethanol conversion, indicating that intermediate radicals react faster via termination mechanisms to stable products than propagation mechanisms to produce more radicals. No formaldehyde is detected in the effluent, indicating that formaldehyde rapidly decomposes to H_2 and CO, or that routes described by Equations 34 and 37 are not favored at these conditions.

10.5. Char Formation

Collection of experimental data was stopped after significant carbon buildup was discovered within the reactor. In ethanol SCWG experiments, no major char formation is observed, indicating that SWPO promotes secondary reaction pathways, likely involving C_2 compounds, that

ultimately lead to char. This seems to run counter to previous observations that SWPO reduces char formation in the processing of complex feedstocks [107].

Coking reactions likely cannot account for all observed carbon buildup during SWPO, as these pathways would have also been accessible during SCWG of methanol, ethanol, and isopropyl alcohol, when no major carbon buildup was observed. SWPO of ethanol must produce a char precursor as an intermediate product. The most likely candidate is ethylene. Hydrogenation of ethylene produces ethane as a stable product, while full oxidation of ethylene produces H_2O and CO_2 as stable products. As an intermediate step, ethylene can undergo hydrogen abstraction to form C_2H_3:

$$C_2H_4 + X \rightarrow C_2H_3\cdot + XH \tag{38}$$

where the abstracting species can be OH, CH_3, or other radicals [101, 102]. Subsequently, C_2H_3 can react via several key pathways, some of which form acetylene:

$$C_2H_3\cdot + O\cdot \rightarrow CH_2O + HCO\cdot \tag{39}$$

$$C_2H_3\cdot + M \rightarrow C_2H_2 + H\cdot + M \tag{40}$$

$$C_2H_3\cdot + H\cdot \rightarrow C_2H_2 + H_2 \tag{41}$$

$$C_2H_3\cdot + H\cdot \rightarrow C_2H_4\cdot \tag{42}$$

In gas-phase combustion experiments, higher C_2H_2 concentrations have been reported in fuel-rich conditions, due to a shift in competition between Equations 39 and Equations 40 through 42 to favor the latter mechanisms at lower oxidant concentrations [101].

An abundance of oxygen (during SCWO) or hydrogen (during SCWG) prevents ethylene from lingering as an intermediate, but SWPO conditions may provide a "sweet spot" for ethylene dehydrogenation to acetylene, which is a critical soot precursor in gas-phase combustion. Pyrolysis of C_2H_2 constitutes the first step toward C_4H_4, previously shown to proceed via molecular reaction at temperatures below 1200 K:

$$C_2H_2 + C_2H_2 \rightarrow C_4H_4 \quad (43)$$

with successive C_2H_2 addition steps to form benzene, and ultimately produce polycyclic aromatic hydrocarbons (PAHs) [114]. These PAHs grow in size building clusters [105], which creates incipient soot particles, which subsequently grow by HACA or condensation mechanisms [117]. Soot formation has been studied in many combustion systems; however, the experiments and modeling of long residence time, low-temperature combustion have been limited [118, 119].

Acetylene is not directly observed in the Raman spectra of the quenched effluent; acetylene has a weak Raman spectrum, with a characteristic peak near 2000 cm^{-1}, which was not visible in experimentally collected spectra, as shown in Figure 35. We assume that acetylene is mostly converted to benzene within the reactor and likely exists in the effluent at concentrations below the detection limit of our Raman setup. Benzene is observed in trace amounts as a reaction product, and the production of char from benzene in supercritical water has been well reported in previous studies [49]. We infer that under the studied SWPO conditions, char formation proceeds via analogous mechanisms as soot formation in gas-phase ethanol combustion. It is important to mention that char yields are qualitatively low - no char is observed in the Raman spectra collected during continuous operation. However, small amounts of solid carbonaceous particles are clearly

visible in the effluent, and char buildup within the reactor was confirmed after all experiments were conducted by cleaning the reactor with acetone.

11. Conclusions

The reaction behavior of four model compounds in supercritical water is determined. Subcritical and supercritical reaction rates and rate parameters for formic acid decomposition are fully determined, assuming first-order reaction behavior [37]. For methanol, ethanol, and isopropyl alcohol, first-order reaction behavior is not observed, and no reaction rates can be proposed [111]. Reaction induction times between 3 and 8 s are observed for all primary alcohols, indicating that free radical reaction mechanisms drive the decomposition of primary alcohols in supercritical water. Catalytic reactor walls are proposed to significantly catalyze these free radical reactions. Adding sub-stoichiometric oxidant is shown to increase gasification efficiency of ethanol in SCW, while surprisingly promoting char formation [120].

In situ Raman spectroscopy allows for product yield data for gaseous and liquid products to be collected rapidly and simultaneously. Post-critical injection of reagents coupled with *in situ* Raman allows for testing short, yet distinct, residence times. Raman spectroscopy shows promise for expediting future experiments, and for future automation of reactor thermal management.

The body of work and the experiments described here form a foundation for bringing SCWG and SWPO towards commercial relevance. A thorough understanding of the gasification behavior of model organic compounds helps elucidate the temperatures and residence times needed to completely gasify real feedstocks into desired products. Although model compounds have been successfully gasified in lab-scale reactors, long-term operation of industrial SCWG reactors with real feedstocks has proven to be technically challenging. The biggest current issues which must be addressed include (i) finding suitable materials to resist corrosion, (ii) mitigating

issues associated with the presence of salts, and (iii) limiting char formation. Future work should be expressly tailored towards solving these challenges.

References

[1] Kruse A, 2008. Supercritical water gasification. *Biofuels. Bioprod. Biorefin. 2*, 415-437.
[2] Kruse A, 2009. Hydrothermal biomass gasification. *J. Supercrit. Fluids 47*, 391-399.
[3] Gong M, Nanda S, Romero MJ, Zhu W, Kozinski JA, 2016. Subcritical and supercritical water gasification of humic acid as a model compound of humic substances in sewage sludge. *J. Supercrit. Fluids 119*, 130-138.
[4] Kamler J, Soria JA, 2012. Supercritical Water Gasification of Municipal Sludge: A Novel Approach to Waste Treatment and Energy Recovery. In *Gasification for Practical Applications*, Yun Y, Ed. InTech: Rijeka, Ch.-06.
[5] Wang C, Zhu W, Gong M, Su Y, Fan Y, 2017. Influence of H2O2 and Ni catalysts on hydrogen production and PAHs inhibition from the supercritical water gasification of dewatered sewage sludge. *J. Supercrit. Fluids 130*, 183-188.
[6] Reddy SN, Nanda S, Dalai AK, Kozinski JA, 2014. Supercritical water gasification of biomass for hydrogen production. *Int. J. Hydrog. Energy 39*, 6912-6926.
[7] Antal Jr MJ, Allen SG, Schulman D, Xu X, Divilio RJ, 2000. Biomass gasification in supercritical water. *Ind. Eng. Chem. Res. 39*, 4040-4053.
[8] Bianchetta S, Li L, Gloyna EF, 1999. Supercritical Water Oxidation of Methylphosphonic Acid. *Ind. Eng. Chem. Res. 38*, 2902-2910.
[9] Savage PE, Gopalan S, Mizan TI, Martino CJ, Brock EE, 1995. Reactions at supercritical conditions: Applications and fundamentals. *AIChE J. 41*, 1723-1778.
[10] Savage PE, 1999. Organic Chemical Reactions in Supercritical Water. *Chem. Rev. 99*, 603-622.
[11] Amin S, Reid RC, Modell M, 1975. Reforming and decomposition of glucose in an aqueous phase, in *Intersociety Conference on Environmental Systems*, San Francisco, ASME Paper 75-ENAS-21.
[12] Pinkard BR, Gorman DJ, Tiwari K, Kramlich JC, Reinhall PG, Novosselov IV, 2018. Review of Gasification of Organic Compounds in Continuous-Flow, Supercritical Water Reactors. *Ind. Eng. Chem. Res. 57*, 3471-3481.
[13] Marrone PA, Hon GT, 2009. Corrosion control methods in supercritical water oxidation and gasification processes. *J. Supercrit. Fluids 51*, 83-103.
[14] Peterson AA, Vogel F, Lachance RP, Fröling M, Antal Jr MJ, Tester JW, 2008. Thermochemical biofuel production in hydrothermal media: a review of sub-and supercritical water technologies. *Energ. Environ. Sci. 1*, 32-65.
[15] Bermejo MD, Cocero MJ, 2006. Supercritical water oxidation: A technical review. *AIChE J. 52*, 3933-3951.
[16] Tang X, Wang S, Qian L, Li Y, Lin Z, Xu D, Zhang Y, 2015. Corrosion behavior of nickel base alloys, stainless steel and titanium alloy in supercritical water containing chloride, phosphate and oxygen. *Chem. Eng. Res. Des. 100*, 530-541.
[17] Hanush RG, Rice SF, Hunter TB, Aiken JD, 1995. *Operation and performance of the Supercritical Fluids Reactor (SFR)* (No. SAND--96-8203). Sandia National Labs., Livermore, CA (United States).
[18] Zhang L, Champagne P, Xu C, 2011. Screening of supported transition metal catalysts for hydrogen production from glucose via catalytic supercritical water gasification. *European Fuel Cell 2009 36*, 9591-9601.

[19] Yu J, Chen Q, Guan Q, Li B, Ning P, Gu J, Lu X, 2016. Characterization of the liquid intermediates from gasification of lignite in supercritical water: Insights into the gasification process for hydrogen production. *Int. J. Hydrog. Energy 41*, 17309-17322.
[20] Pinkard BR, Gorman DJ, Tiwari K, Rasmussen EG, Kramlich JC, Reinhall PG, Novosselov IV, 2019. Supercritical Water Gasification: Practical Design Strategies and Operational Challenges for Lab-Scale, Continuous Flow Reactors. *Heliyon 2*, e01269.
[21] DiLeo GJ, Savage PE, 2006. Catalysis during methanol gasification in supercritical water. *J. Supercrit. Fluids 39*, 228-232.
[22] Caputo G, Rubio P, Scargiali F, Marotta G, Brucato A, 2016. Experimental and fluid dynamic study of continuous supercritical water gasification of glucose. *J. Supercrit. Fluids 107*, 450-461.
[23] Ramayya S, Brittain A, DeAlmeida C, Mok W, Antal Jr MJ, 1987. Acid-catalysed dehydration of alcohols in supercritical water. *Fuel 66*, 1364-1371.
[24] Nanda S, Reddy SN, Hunter HN, Dalai AK, Kozinski JA, 2015. Supercritical water gasification of fructose as a model compound for waste fruits and vegetables. *J. Supercrit. Fluids 104*, 112-121.
[25] Sasaki M, Kabyemela B, Malaluan R, Hirose S, Takeda N, Adschiri T, Arai K, 1998. Cellulose hydrolysis in subcritical and supercritical water. *J. Supercrit. Fluids 13*, 261-268.
[26] Castello D, Kruse A, Fiori L, 2015. Low temperature supercritical water gasification of biomass constituents: Glucose/phenol mixtures. *Biomass Bioenergy 73*, 84-94.
[27] Ondze F, Boutin O, Ruiz JC, Ferrasse JH, Charton F, 2015. Supercritical water gasification of beet residues: From batch to continuous reactor. *Chem. Eng. Sci. 123*, 350-358.
[28] Molino A, Migliori M, Macrì D, Valerio V, Villone A, Nanna F, Iovane P, Marino T, 2016. Glucose gasification in super-critical water conditions for both syngas production and green chemicals with a continuous process. *Renew. Energy 91*, 451-455.
[29] Lemmon EW, Huber ML, McLinden MO, 2013. NIST Standard Reference Database 23: Reference Fluid Thermodynamic and Transport Properties-REFPROP, Version 9.1, National Institute of Standards and Technology.
[30] Wagner W, Pruß A, 2002. The IAPWS Formulation 1995 for the Thermodynamic Properties of Ordinary Water Substance for General and Scientific Use. *J. Phys. Chem. Ref. Data 31*, 387-535.
[31] Shen Z, Yang D, Wang S, Wang W, Li Y, 2017. Experimental and numerical analysis of heat transfer to water at supercritical pressures. *Int. J. Heat Mass Transfer 108*, 1676-1688.
[32] González G, Salvadó J, Montané D, 2004. Reactions of vanillic acid in sub- and supercritical water. *J. Supercrit. Fluids 31*, 57-66.
[33] Aida TM, Sato Y, Watanabe M, Tajima K, Nonaka T, Hattori H, Arai K, 2007. Dehydration of d-glucose in high temperature water at pressures up to 80 MPa. *J. Supercrit. Fluids 40*, 381-388.
[34] Hendry D, Venkitasamy C, Wilkinson N, Jacoby W, 2011. Exploration of the Effect of Process Variables on the Production of High-Value Fuel Gas from Glucose via Supercritical Water Gasification. *Bioresour. Technol. 102*, 3480-3487.
[35] Aida TM, Shiraishi N, Kubo M, Watanabe M, Smith Jr RL, 2010. Reaction kinetics of d-xylose in sub- and supercritical water. *J. Supercrit. Fluids 55*, 208-216.
[36] Yoshida K, Wakai C, Matubayasi N, Nakahara M, 2004. NMR Spectroscopic Evidence for an intermediate of formic acid in the water-gas-shift reaction. *J. Phys. Chem. Letters 108*, 7479-7482.

[37] Pinkard BR, Gorman DJ, Rasmussen EG, Kramlich JC, Reinhall PG, Novosselov IV, 2019. Kinetics of Formic Acid Decomposition in Subcritical and Supercritical Water – A Raman Spectroscopic Study. *Int. J. Hydrog. Energy 44*, 31745-31756.
[38] Rice SF, Hunter TB, Rydén ÅC, Hanush RG, 1996. Raman spectroscopic measurement of oxidation in supercritical water. 1. Conversion of methanol to formaldehyde. *Ind. Eng. Chem. Res. 35*, 2161-2171.
[39] Hunter TB, Rice SF, Hanush RG, 1996. Raman spectroscopic measurement of oxidation in supercritical water. 2. Conversion of isopropyl alcohol to acetone. *Ind. Eng. Chem. Res. 35*, 3984-3990.
[40] Rice SF, Steeper RR, LaJeunesse CA, Hanush RG, Aiken JD, 1997. *Design strategies for high-temperature, high-pressure optical cells*. Sandia National Labs, Livermore, CA. Combustion Research Facility.
[41] Frantz JD, Dubessy J, Mysen B, 1993. An optical cell for Raman spectroscopic studies of supercritical fluids and its application to the study of water to 500 C and 2000 bar. *Chem. Geol. 106*, 9-26.
[42] Spohn PD, Brill TB, 1987. A Raman spectroscopy cell for aqueous solutions to 500° C and 34.5 MPa. *Appl. Spectrosc. 41*, 1152-1156.
[43] Gorbaty YE, Bondarenko GV, 1995. High-pressure high-temperature Raman cell for corrosive liquids. *Rev. Sci. Instrum. 66*, 4347-4349.
[44] Gorbaty YE, Bondarenko GV, Venardou E, Barlow SJ, Garcia-Verdugo E, Poliakoff M, 2004. Experimental spectroscopic high-temperature high-pressure techniques for studying liquid and supercritical fluids. *Vib. Spectrosc. 35*, 97-101.
[45] Gorbaty YE, Bondarenko GV, Venardou E, Garcia-Verdugo E, Sokolova M, Ke J, Poliakoff M, 2003. High-pressure high-temperature Raman spectroscopy of liquid and supercritical fluids. *Appl. Spectrosc. 57*, 1300-1303.
[46] Myrick ML, Kolis J, Parsons E, Chike K, Lovelace M, Scrivens W, Holliday R, Williams M, 1994. In situ fiber-optic Raman spectroscopy of organic chemistry in a supercritical water reactor. *J. Raman Spectrosc. 25*, 59-65.
[47] Huelsman CM, Savage PE, 2013. Reaction Pathways and Kinetic Modeling for Phenol Gasification in Supercritical Water. *J. Supercrit. Fluids 81*, 200-209.
[48] Yong TLK, Matsumura Y, 2013. Kinetic Analysis of Guaiacol Conversion in Sub- and Supercritical Water. *Ind. Eng. Chem. Res. 52*, 9048-9059.
[49] Yong TLK, Matsumura Y, 2014. Kinetics Analysis of Phenol and Benzene Decomposition in Supercritical Water. *J. Supercrit. Fluids 87*, 73-82.
[50] Goodwin AK, Rorrer GL, 2008. Conversion of glucose to hydrogen-rich gas by supercritical water in a microchannel reactor. *Ind. Eng. Chem. Res. 47*, 4106-4114.
[51] Kabyemela BM, Adschiri T, Malaluan RM, Arai K, 1999. Glucose and fructose decomposition in subcritical and supercritical water: detailed reaction pathway, mechanisms, and kinetics. *Ind. Eng. Chem. Res. 38*, 2888-2895.
[52] Aida TM, Tajima K, Watanabe M, Saito Y, Kuroda K, Nonaka T, Hattori H, Smith Jr RL, Arai K, 2007. Reactions of d-fructose in water at temperatures up to 400 C and pressures up to 100 MPa. *J. Supercrit. Fluids 42*, 110-119.
[53] Kabyemela BM, Adschiri T, Malaluan RM, Arai K, 1997. Kinetics of Glucose Epimerization and Decomposition in Subcritical and Supercritical Water. *Ind. Eng. Chem. Res. 36*, 1552-1558.

[54] Promdej C, Matsumura Y, 2011. Temperature Effect on Hydrothermal Decomposition of Glucose in Sub- and Supercritical Water. *Ind. Eng. Chem. Res. 50*, 8492-8497.
[55] Yu D, Aihara M, Antal Jr MJ, 1993. Hydrogen Production by Steam Reforming Glucose in Supercritical Water. *Energy Fuels 7*, 574-577.
[56] Susanti RF, Dianningrum LW, Yum T, Kim Y, Lee BG, Kim J, 2012. High-yield Hydrogen Production from Glucose by Supercritical Water Gasification Without Added Catalyst. *Int. J. Hydrog. Energy 37*, 11677-11690.
[57] Nanda S, Reddy SN, Hunter HN, Butler IS, Kozinski JA, 2015. Supercritical Water Gasification of Lactose as a Model Compound for Valorization of Dairy Industry Effluents. *Ind. Eng. Chem. Res. 54*, 9296-9306.
[58] Hack W, Masten DA, Buelow SJ, 2005. Methanol and ethanol decomposition in supercritical water. *Zeitschrift für Physikalische Chemie 219*, 367-378.
[59] Van Bennekom JG, Venderbosch RH, Assink D, Heeres HJ, 2011. Reforming of methanol and glycerol in supercritical water. *J. Supercrit. Fluids 58*, 99-113.
[60] Guo S, Guo L, Cao C, Yin J, Lu Y, Zhang X, 2012. Hydrogen Production from Glycerol by Supercritical Water Gasification in a Continuous-flow Tubular Reactor. *Int. J. Hydrog. Energy 37*, 5559-5568.
[61] Asinger F, Asinger F, 1986. *Methanol - Chemie und Energierohstoff*; S.B. Heidelberg.
[62] Boukis N, Diem V, Habicht W, Dinjus E, 2003. Methanol Reforming in Supercritical Water. *Ind. Eng. Chem. Res. 42*, 728-735.
[63] Boukis N, Diem V, Galla U, Dinjus E, 2007. Methanol Reforming in Supercritical Water for Hydrogen Production. *Combust. Sci. Technol. 178*, 467-485.
[64] May A, Salvadó J, Torras C, Montané D, 2010. Catalytic gasification of glycerol in supercritical water. *Chem. Eng. J. 160*, 751-759.
[65] Bühler W, Dinjus E, Ederer HJ, Kruse A, Mas C, 2002. Ionic reactions and pyrolysis of glycerol as competing reaction pathways in near-and supercritical water. *J. Supercrit. Fluids 22*, 37.
[66] Antal Jr MJ, Mok WSL, Roy JC, Anderson DGM, 1985. Pyrolytic sources of hydrocarbons from biomass. *J. Anal. Appl. Pyrolysis 8*, 291-303.
[67] Klingler D, Berg J, Vogel H, 2007. Hydrothermal reactions of alanine and glycine in sub- and supercritical water. *J. Supercrit. Fluids 43*, 112-119.
[68] Kang K, Quitain AT, Daimon H, Noda R, Goto N, Hu H, Fujie K, 2001. Optimization of Amino Acid Production from Waste Fish Entrails by Hydrolysis in Sub- and Supercritical Water. *Can. J. Chem. Eng. 79*, 65-70.
[69] Islam MN, Kaneko T, Kobayashi K, 2003. Reaction of Amino Acids in Supercritical Water-Flow Reactor Simulating Submarine Hydrothermal Systems. *Bull. Chem. Soc. Jpn. 76*, 1171-1178.
[70] Sato N, Daimon H, Fujie K, 2002. Decomposition of Glycine in High Temperature and High Pressure Water. *Kagaku Kogaku Ronbunshu 28*, 113-117.
[71] Sato N, Quitain AT, Kang K, Daimon H, Fujie K, 2004. Reaction Kinetics of Amino Acid Decomposition in High-Temperature and High-Pressure Water. *Ind. Eng. Chem. Res. 43*, 3217-3222.
[72] Samanmulya T, Inoue S, Inoue T, Kawai Y, Kubota H, Munetsuna H, Noguchi T, Matsumura Y, 2014. Gasification Characteristics of Alanine in Supercritical Water. *J. Jpn. Petrol. Inst. 57*, 225-229.

[73] Samanmulya T, Inoue S, Inoue T, Kawai Y, Kubota H, Munetsuna H, Noguchi T, Matsumura Y, 2014. Gasification Characteristics of Amino Acids in Supercritical Water. *J. Jpn. Inst. Energy 93*, 936-943.
[74] Samanmulya T, Matsumura Y, 2013. Effect of Activated Carbon Catalytic on Supercritical Water Gasification of Glycine as a Model Compound of Protein. *J. Jpn. Inst. Energy 92*, 894-899.
[75] Weiss-Hortala E, Kruse A, Ceccarelli C, Barna R, 2010. Influence of phenol on glucose degradation during supercritical water gasification. *J. Supercrit. Fluids 53*, 42-47.
[76] Hao XH, Guo LJ, Mao X, Zhang XM, Chen XJ, 2003. Hydrogen production from glucose used as a model compound of biomass gasified in supercritical water. *Int. J. Hydrog. Energy 28*, 55-64.
[77] Yu J, Savage PE, 1998. Decomposition of formic acid under hydrothermal conditions. *Ind. Eng. Chem. Res. 37*, 2-10.
[78] Zhang Y, Zhang J, Zhao L, Sheng C, 2009. Decomposition of formic acid in supercritical water. *Energy Fuels 24*, 95-99.
[79] Tiwari K, Pinkard BR, Gorman DJ, Davis J, Kramlich JC, Reinhall PG, Novosselov IV, 2018. Computational Modeling of Mixing and Gasification in Continuous Flow Supercritical Water Reactor. In *Proceedings of 12th International Symposium on Supercritical Fluids*.
[80] Gan F, Ruan G, Mo J, 2006. Baseline correction by improved iterative polynomial fitting with automatic threshold, *Chemom. Intell. Lab. Syst. 82*, 59-65.
[81] Ruckstuhl AF, Jacobson MP, Field RW, Dodd JA, 2001. Baseline subtraction using robust local regression estimation, *J. Quant. Spectrosc. Radiat. Transf. 68*, 179-193.
[82] Liland KH, Almøy T, Mevik BH, 2010. Optimal choice of baseline correction for multivariate calibration of spectra, *Appl. Spectrosc. 64*, 1007-1016.
[83] Pinkard BR, Gorman DJ, Rasmussen EG, Maheshwari V, Kramlich JC, Reinhall PG, Novosselov IV, 2020. Raman Spectroscopic Data from Formic Acid Decomposition in Subcritical and Supercritical Water. *Data Brief 29*, 105312.
[84] Kriesten E, Alsmeyer F, Bardow A, Marquardt W, Fully automated indirect hard modeling of mixture spectra, *Chemom. Intell. Lab. Syst. 91*, 181-193.
[85] Alsmeyer F, Koß HJ, Marquardt W, Indirect spectral hard modeling for the analysis of reactive and interacting mixtures, *Appl. Spectrosc. 58*, 975-985.
[86] Beumers P, Brands T, Koss HJ, Bardow A, 2016. Model-free calibration of Raman measurements of reactive systems: application to monoethanolamine/water/CO2, *Fluid Phase Equilib. 424*, 52-57.
[87] Magnotti G, KC U, Varghese PL, Barlow RS, 2015. Raman spectra of methane, ethylene, ethane, dimethyl ether, formaldehyde, and propane for combustion application. *J. Quant. Spectrosc. Radiat. Transf. 163*, 80-101.
[88] Griffiths JE, Clerc M, Rentzepis PM, 1974. Intermolecular energy transfer in liquid benzene: Raman spectra, linewidth measurements, picosecond spectroscopy, and vibrational relaxation times. *J. Chem. Phys. 60*, 3824-3830.
[89] Bjerre AB, Soerensen E, 1992. Thermal decomposition of dilute aqueous formic acid solutions. *Ind. Eng. Chem. Res. 31*, 1574-1577.
[90] Rice SF, Steeper RR, Aiken JD, 1998. Water density effects on homogeneous water-gas shift reaction kinetics. *J. Phys. Chem. A 102*, 2673-2678.

[91] Melius CF, Bergan NE, Shepherd JE, 1991. Effects of water on combustion kinetics at high pressure. In *Symposium (International) on Combustion 23*, 217-223.
[92] Picou J, Stever M, Bouquet J, Wenzel J, Lee S, 2014. Kinetics of the non-catalytic water-gas shift reaction in supercritical water. *Energ. Source. Part A 36*, 2666-2672.
[93] Araki K, Fujiwara H, Sugimoto K, Oshima Y, Koda S, 2004. Kinetics of water-gas shift reaction in supercritical water. *J. Chem. Eng. Japan 37*, 443-448.
[94] Wei J, Iglesia E, 2004. Isotopic and kinetic assessment of the mechanism of reactions of CH4 with CO2 or H2O to form synthesis gas and carbon on nickel catalysts. *J. Catal. 224*, 370-383.
[95] Chakinala AG, Kumar S, Kruse A, Kersten SR, van Swaaij WP, Brilman DW, 2013. Supercritical water gasification of organic acids and alcohols: the effect of chain length. *J. Supercrit. Fluids 74*, 8-21.
[96] Schanzenbacher J, Taylor JD, Tester JW, 2002. Ethanol oxidation and hydrolysis rates in supercritical water. *J. Supercrit. Fluids 22*, 139-147.
[97] Arita T, Nakahara K, Nagami K, Kajimoto O, 2003. Hydrogen generation from ethanol in supercritical water without catalyst. *Tetrahedron Lett. 44*, 1083-1086.
[98] Antal MJ, Carlsson M, Xu X, 1998. Mechanism and kinetics of the acid-catalyzed dehydration of 1- and 2-propanol in hot compressed liquid water. *Ind. Eng. Chem. Res. 37*, 3820-3829.
[99] Rice SF, Croiset E, 2001. Oxidation of simple alcohols in supercritical water III. Formation of intermediates from ethanol. *Ind. Eng. Chem. Res. 40*, 86-93.
[100] Held TJ, Dryer FL, 1998. A comprehensive mechanism for methanol oxidation. *Int. J. Chem. Kin. 30*, 805-830.
[101] Norton TS, Dryer FL, 1992. An experimental and modeling study of ethanol oxidation kinetics in an atmospheric pressure flow reactor. *Int. J. Chem. Kin. 24*, 319-344.
[102] Marinov NM, 1999. A detailed chemical kinetic model for high temperature ethanol oxidation. *Int. J. Chem. Kin. 31*, 183-220.
[103] Li J, Kazakov A, Dryer FL, 2001. Ethanol pyrolysis experiments in a variable pressure flow reactor. *Int. J. Chem. Kin. 33*, 859-867.
[104] Huelsman CM, Savage PE, 2012. Intermediates and kinetics for phenol gasification in supercritical water. *Phys. Chem. Chem. Phys. 14*, 2900-2910.
[105] Frenklach M, 2002. Reaction mechanism of soot formation in flames. *Phys. Chem. Chem. Phys. 4*, 2028-2037.
[106] Matsumura Y, Goto S, Takase Y, Inoue S, Inoue T, Kawai Y, Noguchi T, Tanigawa H, 2018. Suppression of radical char production in supercritical water gasification by addition of organic acid radical scavenger. *Energy Fuels 32*, 9568-9571.
[107] Hong GT, Spritzer MH, 2002. Supercritical Water Partial Oxidation. *Proceedings of the 2002 U.S. DOE Hydrogen Program Review*. NREL/CP-610-32405.
[108] Alshammari YM, Hellgardt K, 2015. Partial oxidation of n-hexadecane through decomposition of hydrogen peroxide in supercritical water. *Chem. Eng. Res. Des. 93*, 565-575.
[109] Sato T, Adschiri T, Arai K, Rempel GL, Ng FTT, 2003. Upgrading of asphalt with and without partial oxidation in supercritical water. *Fuel 82*, 1231-1239.

[110] Kruse A, Gawlik A, 2003. Biomass conversion in water at 330-410 °C and 30-50 MPa. Identification of Key Compounds for Indicating Different Chemical Reaction Pathways. *Ind. Eng. Chem. Res. 42*, 267-279.
[111] Pinkard BR, Kramlich JC, Novosselov IV, 2020. Gasification Pathways and Reaction Mechanisms of Primary Alcohols in Supercritical Water. *ACS Sustain. Chem. Eng. 8* 4598-4605.
[112] Croiset E, Rice SF, Hanush RG, 1997. Hydrogen Peroxide Decomposition in Supercritical Water. *AIChE J. 43*, 2343-2352.
[113] Holgate HR, Tester JW, 1994. Oxidation of Hydrogen and Carbon Monoxide in Sub- and Supercritical Water: Reaction Kinetics, Pathways, and Water-Density Effects. 1. Experimental Results. *J. Phys. Chem. 98*, 800-809.
[114] Saggese C, Sanchez NE, Frassoldati A, Cuoci A, Faravelli T, Alzueta MU, Ranzi E, 2014. Kinetic Modeling Study of Polycyclic Aromatic Hydrocarbons and Soot Formation in Acetylene Pyrolysis. *Energy Fuels 28*, 1489-1501.
[115] Therdthianwong S, Srisiriwat N, Therdthianwong A, Croiset E, 2011. Hydrogen production from bioethanol reforming in supercritical water. *J. Supercrit. Fluids 57*, 58-65.
[116] Helling RK, Tester JW, 1988. Oxidation of Simple Compounds and Mixtures in Supercritical Water: Carbon Monoxide, Ammonia, and Ethanol. *Environ. Sci. Technol. 22*, 1319-1324.
[117] Wang H, 2011. Formation of nascent soot and other condensed-phase materials in flames. *P. Combust. Inst. 33*, 41-67.
[118] Davis J, Tiwari K, Novosselov IV, 2019. Soot morphology and nanostructure in complex flame flow patterns via secondary particle surface growth. *Fuel 245*, 447-457.
[119] Davis J, Molnar E, Novosselov IV, 2020. Nanostructure transition of young soot aggregates to mature soot aggregates in diluted diffusion flames. *Carbon 159*, 255-265.
[120] Pinkard BR, Purohit AL, Moore SJ, Kramlich JC, Reinhall PG, Novosselov IV, 2020. Partial Oxidation of Ethanol in Supercritical Water. *Ind. Eng. Chem. Res.* (In Press) https://doi.org/10.1021/acs.iecr.0c00945.